

**ACCELERATED DYNAMIC CARDIAC MRI
USING MOTION-GUIDED COMPRESSED
SENSING WITH REGIONAL SPARSITY**

A Dissertation

Presented to

The Faculty of the School of Engineering and Applied Science

University of Virginia

In Partial Fulfillment

Of the Requirements for the Degree

Doctor of Philosophy in Biomedical Engineering

By

Xiao Chen

May, 2015

© Copyright by

Xiao Chen

All rights reserved

May, 2015

APPROVAL SHEET

The dissertation
is submitted in partial fulfillment of the requirements
for the degree of
Doctor of Philosophy



AUTHOR

The dissertation has been read and approved by the examining committee:

Frederick H. Epstein

Advisor

Craig H. Meyer

Michael Salerno

John P. Mugler, III

Scott T. Acton

Accepted for the School of Engineering and Applied Science:



Dean, School of Engineering and Applied Science

May
2015

Abstract

Dynamic cardiac Magnetic Resonance Imaging (CMR) demands fast imaging techniques to obtain high spatial-resolution, large spatial-coverage and high temporal-resolution images for accurate prognosis and diagnosis. Compressed sensing (CS), a fast imaging technique of growing importance, is making a major impact on MRI. Using CS, high-quality images can be recovered from data sampled well below the Nyquist rate. Because of the high temporal and spatial redundancy inherent to dynamic images, these data are well-suited for acceleration by CS. However, the complex dynamics which include both object motions and image contrast variations encountered in dynamic CMR pose challenging tasks for CS techniques. The complexity, if not handled correctly, leads to largely degraded reconstruction quality.

This dissertation presents a novel CS method to accelerate dynamic CMR imaging, especially those with complex dynamics, with a motion-compensated CS method that exploits regional spatiotemporal sparsity: Block Low-rank Sparsity with Motion-guidance (BLOSM). In one iteration of the BLOSM calculation, blocks of image pixels are motion-tracked through time and low-rank sparsity is exploited within the tracked blocks. The de-noised blocks are merged back into complete images and compensated for data fidelity.

The BLOSM method was first developed and validated using retrospectively accelerated first-pass cardiac perfusion images with prominent respiratory motion and computer simulated motion phantoms. Systematic experiments were conducted to compare BLOSM to several other

competing CS methods. The BLOSM showed great quality improvement for the images presenting complex dynamics.

Two CMR applications of great clinical importance, both of which present distinct and extremely challenging tasks for CS, were prospectively accelerated using BLOSM.

First-pass cardiac perfusion imaging was accelerated on patients with suspected heart disease. With prospective rate 4 acceleration, multi-slice high spatial resolution perfusion images were acquired. A Poisson-disc-distributed sampling pattern was implemented. BLOSM was extended to incorporate parallel imaging. The image quality offered by BLOSM showed significant improvement over the other CS methods when respiratory motion occurred.

2D cine DENSE imaging was accelerated using BLOSM. The scan time was shortened from two separate breathholds of total 28 heartbeats to one single breathhold of 8 heartbeats. Variable-density spiral trajectory with golden angle rotation was designed for accelerated data sampling. Both retrospective and prospective studies were conducted in healthy volunteers and BLOSM provided high image quality and the cardiac function assessed from BLOSM reconstructed images matched well with the fully-sampled reference data.

Acknowledgements

I would like to express my deepest appreciation to my advisor Dr. Frederick H. Epstein for his unlimited support and encouragement in both avenues of academic and personal growth. Without his expert advice and contributions, this dissertation would not have been possible. I have learned and benefited a lot from his expertise in the MRI field, his scientific thoughts, his great work passion and his inspiring optimism. I am grateful to my committee chair Dr. Craig H. Meyer for his specific insights into the field, his knowledge of spiral imaging and his instructions on graduate study. I would express my sincere appreciation for Dr. Michael Salerno for his strong support on the perfusion imaging and the clinical studies. I learned a lot from our discussions and his passion always impressed me. I would thank Dr. Scott T. Acton for providing me unlimited help on the knowledge of image processing. I would also sincerely thank Dr. John P. Mugler for his knowledgeable insight into sequence designing and programming.

I would like to thank Dr. Christopher M. Kramer for his support and instructions on the clinical studies. I also want to appreciate Dr. Klaus D. Hagspiel, Dr. Patrick T. Norton and Dr. Peter Shaw for their supports on the clinical perfusion studies. I would like to thank Dr. Xiaodong Zhong for the early work and continuous help on the DENSE project. I learned a lot from his strict research spirit. I enjoyed the usual technical discussions with my colleagues Yang Yang, Bhairav B. Mehta, Nivedita K. Naresh, Dr. Xue Feng, Dr. Patrick F. Antkowiak, Dr. Kun Qing and Dr. Li Zhao, and I would also like to express my sincere appreciation for their help on this dissertation work. All of them have made my graduate student experience most enjoyable and unforgettable.

Finally, and most importantly, I would like to thank my parents, Qi Chen and Beirong Zheng, and my wonderful wife, Huijie Li, for their firm support through my Ph.D. study and through my life. I am extremely grateful for all they have done for me and owe all that I have achieved to them.

Table of Contents

Abstract	I
Acknowledgements	III
Table of Contents	V
List of Tables	X
List of Figures	XI
List of Symbols	XXIV
List of Abbreviations	XXVIII
Chapter 1 Introduction.....	1
1.1 Cardiac Magnetic Resonance Imaging	1
1.2 MRI data	1
1.3 MRI acceleration.....	3
1.4 Compressed sensing.....	4
1.5 Sparsity in dynamic CMR images	5
1.5.1 Object motion, no change in image contrast.....	6
1.5.2 Smoothly-changing image contrast, no object motion.....	7
1.5.3 Object motion and changes in image contrast.....	7
1.6 CS for complex dynamics	7

1.6.1 Data-driven sparsity transform.....	8
1.6.2 Motion-guided CS.....	9
1.6.3. Regional sparsity.....	11
1.7 K-T sampling pattern.....	12
1.8 Cardiac first-pass perfusion	13
1.9 Cine Displacement ENcoding with Stimulated Echoes (DENSE)	14
1.10 Retrospective acceleration study and prospective acceleration study.....	15
1.11 Dissertation Aims.....	16
1.12 Dissertation Overview.....	17
Chapter 2 BLOSM: Block LOw-rank Sparsity with Motion-guidance.....	19
2.1 Introduction.....	20
2.2 Methods.....	22
2.2.1 BLOSM Overview	22
2.2.2 Block motion tracking.....	25
2.2.3 Regional sparsity.....	27
2.2.4 Coarse-to-fine strategy.....	28
2.2.5 Avoidance of gaps.....	29
2.2.6 Optimization method.....	30
2.2.7 Evaluation of BLOSM	31
2.2.8 Computer-simulated phantoms	33
2.2.9 First-pass cardiac perfusion imaging	34

2.2.10 Evaluation of initial block size, initial block positions, the coarse-to-fine strategy, and the use of motion compensation.....	35
2.2.11 Computation time.....	36
2.3 RESULTS	37
2.3.1 Comparison of BLOSM and other CS reconstruction methods using computer simulations...	37
2.3.2 Comparison of BLOSM and other CS reconstruction methods for accelerated first-pass cardiac perfusion imaging of human subjects	40
2.3.3 Evaluation of initial block size, initial block positions, the coarse-to-fine strategy, and the use of motion compensation.....	44
2.3.4 Computation time.....	47
2.4 DISCUSSION.....	48
Chapter 3 Prospectively Accelerated CMR First-pass Perfusion Imaging in Patients with Suspected Heart Disease	58
3.1 Introduction.....	59
3.2 Methods.....	61
3.2.1 Accelerated first-pass perfusion sequence	61
3.2.2 Prospective-accelerated patient data collection	62
3.2.3 Retrospective-accelerated patient data simulation	63
3.2.4 Data reconstruction	64
3.2.5 Reconstruction assessment.....	66
3.3 Results.....	67
3.4 Discussion.....	71

Chapter 4	Accelerated 2D Cine DENSE using BLOSM.....	76
4.1	Introduction.....	77
4.2	METHODS	79
4.2.1	Data acquisition.....	79
4.2.2	Data reconstruction	80
4.2.3	Evaluation using computer-simulated phantom.....	83
4.2.4	Evaluation using in vivo data.....	85
4.2.5	Comparison of reconstruction methods	86
4.2.6	Functional analysis.....	88
4.3	RESULTS	88
4.3.1	Computer-simulated phantom.....	88
4.3.2	Evaluation of in vivo studies.....	94
4.4	DISCUSSION.....	99
4.4.1	Comparison of different image reconstruction methods	100
4.4.2	Independent encoding vs. joint encoding.....	102
4.4.3	Clinical implications	102
4.4.4	Accelerated 3D cine DENSE	103
Chapter 5	Conclusions and Future Work	106
5.1	Conclusions.....	106
5.2	Future work.....	108
	Free-preparation CMR	108

Higher order data correlations.....	109
Basis functions	110
2D first-pass CMR	110
2D cine DENSE	111
3D imaging.....	111
Optimization parameter selection	112
Computation time.....	112
Appendix Publications, Patents, Awards and Conference Abstracts	113
A.1 Journal Papers	113
A.2 Patents	114
A.3 Awards	114
A.4 Oral Presentations	115
A.5 Other Conference Abstracts	117
References	121

List of Tables

- Table 3.1 Summary of image quality and motion degree scores. The average score from the two scorers are listed. The scores were then averaged over different image studies and standard deviation was calculated.
- Table 3.2 Summary of all image quality scores from the two scorers on the prospectively rate-4 accelerated data. Count and frequency of each score level are shown.
- Table 4.1 Parameters of the variable density spiral trajectories for fully-sampled and accelerated acquisitions. The reference sampling density of 1 corresponds to the Nyquist rate.
- Table 4.2 Bland-Altman and linear regression results from phantoms studies for different reconstruction algorithms and acceleration rates.
- Table 4.3 Bland-Altman and linear regression results from volunteers studies for different reconstruction algorithms and acceleration rates.

List of Figures

- Figure 1.1 Fourier transform relationship between k-space data (A-C) and image space image (a-c) in MRI. Fully-sampled k-space (A) reconstructed by Fourier transform (F.T.) present no image artifacts (a). Undersampled k-space data in an interleaved pattern (B) leads to aliasing artifacts (b). Undersampled k-space data in a pseudo-random pattern (C) leads to blurring artifacts (c).
- Figure 1.2 Three types of dynamics in dynamic CMR images. 1st row is balanced SSFP images. 2nd row is modified Look-Locker images. 3rd row is first-pass perfusion images. Example images at different time points are shown.
- Figure 1.3 Illustration of data-driven basis function analysis of dynamic images. The dynamic images can be decomposed to a multiplication of three matrices referred as singular value decomposition, where the first matrix contains basis spatial patterns, the last matrix contains basis temporal patterns and the center matrix contains the singular values representing the weightings of the patterns. Big singular value (#1) means big contribution of the corresponding patterns (#1 in the spatial pattern and in the temporal pattern) in the dynamic images. Small singular value mostly present noises in the dynamic images.
- Figure 1.4 Motion guidance is required to compute the correct image temporal difference. Im_{t-1} , Im_t and Im_{t+1} are three consecutive dynamic images in time. When motion occurs between Im_{t-1} , Im_t and Im_{t+1} (from dashed frame to solid frame), the temporal difference from motion-corrected images (solid arrow) is correctly computed, while the temporal difference

calculated from non-motion-corrected images (dashed arrow) is incorrect due to mis-registration.

Figure 1.5 Example k-t sampling patterns and sampling frequencies of interleaved (A) random with dual density (B) and random with variable density (C). Each point on the sampling pattern represents one phase-encoding k_y line in the k-space at time t . White points mean the data is sampled and the three patterns shown here have the same number sampling points.

Figure 1.6 Example cine DENSE images from different cardiac phases. Magnitude images are shown on the top row and phase images with displacement encoded in the vertical direction are shown on the bottom row. Cardiac contraction motion along with signal intensity changes can be observed on the images.

Figure 2.1 General description of Block Low-rank Sparsity with Motion-guidance (BLOSM). A set of undersampled dynamic images are divided into blocks (labeled 1 to 5 as an example). Motion trajectories for each block are obtained from the current image estimation and used to track each block through time. The motion-tracked blocks are stacked together to form a cluster for each group of blocks. Each cluster then undergoes a singular value shrinkage step and the resulting blocks are merged into a new estimated image. The iterations continue for a fixed number of iterations or until a stopping criteria is met.

Figure 2.2 BLOSM tracks blocks of pixels through time and exploits regional low-rank sparsity. An example block of pixels (red square) is tracked through all the frames. These temporally related blocks with similar spatial contents are gathered together to form a 3D ($N_b \times N_b \times N_t$) cluster. The cluster is

rearranged into a 2D matrix ($N_s \times N_t$, $N_s = N_b \times N_b$), which has high spatiotemporal correlations. Singular value decomposition is applied to the matrix, and only a few of the singular values have significantly higher values than the others, thus the data present low-rank sparsity.

Figure 2.3

Illustration of BLOSM block tracking. $m(t_1)$ and $m(t_2)$ are two consecutive images. An object (gray circle) is displayed on both images which underwent a translational shift (rightward and upward) from frame to frame. A red point is labeled on the circle to represent part of the object. A block $B(u_1)$ centered at the red point is initiated on $m(t_1)$. The red point is tracked from $m(t_1)$ to $m(t_2)$ using the ANTS toolbox, as shown by the arrow. Note that the tracked point on $m(t_2)$ is not at the center of the pixel. Instead of using spatial interpolation, the pixel containing the red dot (the shaded pixel) is selected as the new center pixel for the block. Then the neighboring pixels are included to form a tracked block on $m(t_2)$ as $B(u_2)$ where $u_2 = \{u_1 + \Delta u_1\}$.

Figure 2.4

In BLOSM, overlapping blocks are used to avoid gaps. The circles in the figure represent block centers. The solid red centers represent initial blocks that cover the whole image, and the unfilled circles represent additional blocks. The initial blocks are demarcated by solid lines, and the additional blocks, which overlap the initial blocks, are demarcated by dashed lines.

Figure 2.5

Simulated phantoms in a time series. Images at selected time points are shown. Phantom 1 (P1) undergoes rigid translational shifts along the phase-encoding direction. P2 has an abrupt change in size as well as appearance/disappearance of features to mimic through plane motion combined with translational shifts in the readout direction. P3 undergoes

rigid translational shifts along the readout direction. P4 undergoes a gradual change in size which can be interpreted as either cardiac contraction or through-plane motion. P5 rotates counterclockwise through time to mimic object rotation motion. All the phantoms also have quadratically changing signal intensity over time.

Figure 2.6

Reconstruction of retrospectively rate-4 undersampled images from computer-simulated phantoms that undergo translational shifts, rotation, deformation/TPM and variable signal intensity over time. Example reconstructed images at one time frame are shown in the top row. Corresponding x-t profiles for each phantom (P1-P5) are shown on the bottom panel, where the profile locations are indicated by dashed lines on the fully-sampled image. The first column shows fully-sampled data reconstructed by FFT and serves as a reference. The other columns display undersampled data reconstructed using conventional FFT and the CS methods: BLOSM, k-t FOCUSS with ME/MC, k-t SLR, BLOSM without motion guidance (BLOSM w/o MG) and k-t SLR with global motion guidance (k-t SLR w/ gMG). BLOSM provided the most accurate recovery of the fully sampled images. For k-t FOCUSS with ME/MC, k-t SLR and BLOSM w/o MG, residual artifacts and moderate motion blurring can be observed, especially on P4.

Figure 2.7

Comparison of BLOSM with other CS algorithms using retrospectively rate-4 undersampled first-pass contrast-enhanced MRI of the heart. Example frames are presented in different rows representing early, mid and late phases of contrast passage. Undersampled data are reconstructed by conventional FFT, BLOSM, k-t FOCUSS with ME/MC, k-t SLR, BLOSM without motion guidance (w/o MG) and k-t SLR with global motion guidance (w/ gMG). Respiratory motion occurred to a large degree during the middle phase (second row) and to a lesser degree at the late phase (third

row). BLOSM provided the best image quality for all the phases and very closely matched the fully-sampled images. k-t FOCUSS with ME/MC, k-t SLR and BLOSM w/o MG performed fairly well for phases where there was no or little motion. For the mid phase, severe artifacts can be seen for k-t FOCUSS with ME/MC, k-t SLR and BLOSM w/o MG. k-t SLR w/ gMG resulted in blurred images for all phases. x-t profiles showing similar results are shown on the bottom row, with important dynamic features highlighted by red arrows.

Figure 2.8

Quantitative analysis of the performance of various reconstruction methods applied to rate-4 accelerated first-pass contrast-enhanced MRI of the heart. Average relative root mean square error (rRMSE) and structural similarity (SSIM), averaged over time, of the CS-reconstructed images were compared to fully-sampled reference images. BLOSM achieved the lowest error (rRMSE) and highest similarity (SSIM) of all the CS methods. (* $P < 0.01$ v.s. undersampled, k-t FOCUSS with ME/MC, k-t SLR and k-t SLR w/ gMG; & $P < 0.05$ v.s. BLOSM w/o MG; ** $P < 0.01$ v.s. undersampled, k-t SLR, and k-t SLR w/ gMG; \$ $P < 0.05$ v.s. k-t FOCUSS with ME/MC).

Figure 2.9

Convergence of BLOSM for different initial block sizes. BLOSM using different initial block sizes was used to reconstruct a first-pass perfusion dataset. These rRMSE vs. iteration curves demonstrate that the convergence of BLOSM is essentially independent of the initial block size (not all tested initial block sizes are shown, but all had similar behavior).

Figure 2.10

Convergence of BLOSM under various conditions. Panels (A and B) show for both computer simulated phantoms and in vivo perfusion imaging that the coarse-to-fine strategy provides lower rRMSE compared to not using

this strategy. Similarly, panels (C and D) show that for both computer simulated phantoms and in vivo perfusion imaging the use of motion guidance reduces rRMSE compared to not using motion guidance.

Figure 2.11

Image reconstruction using BLOSM is not highly dependent on the initial block positions. Images were reconstructed using BLOSM with original initial block positions (A) and with shifted initial block positions (D). The difference between a fully-sampled 2DFT-reconstructed image (Reference image) and (A) is shown in (B), and the difference between the reference image and (D) is shown in (E). Histograms from multiphase difference images using the original initial block positions and the shifted initial block positions are shown in (C) and (F), respectively. Using either the original initial block positions or the shifted initial block positions results in the same difference distribution (Gaussian distribution verified using the Jarque-Beta test) compared to the reference images. μ is the mean and σ^2 is the variance.

Figure 2.12

Relative root mean square (rRMSE) values from 30 dataset (26 human perfusion and 4 computer simulation) using BLOSM and BLOSM with average motion (BLOSM w/ avg. motion). Similar rRMSE were found among the two implementations while for some dataset BLOSM which uses the central pixel to represent the block motion had better rRMSE behavior.

Figure 2.13

Tracking of two example pixels through time using integer-displacement and non-integer-displacement methods. No accumulation of error is observed.

Figure 2.14

Example images and singular values before and after regularization using different threshold levels (λ values). Images showed visible blocking

artifacts, i.e. discontinuities at block edges at a high threshold level ($\lambda = 15000$). Singular values from two regions, one over the left ventricle blood pool and the other over the background (squares on the original image), were calculated and compared. With the setting of norm $p = 0.9$, region 2 received more regularization than region 1. When λ increased to 15000 (bottom row), large singular values which contained most of the image energy and contrast information were influenced and gave rise to the blocking artifacts.

Figure 3.1

Example variable-density k_y - t sampling pattern following Poisson-disc distribution and corresponding sampling frequency at different k_y positions. The center of the k -space is fully sampled at all time points. The radius of the Poisson-disc increases from the center k_y towards the edge of the k space, resulting in decreased sampling density. Prospective rate 4 and 6 patterns are generated on the scanner. Retrospective rate 6 and rate 8 patterns are down-sampled from the prospective rate 4 pattern by randomly removing k_y lines. Note that the sampling frequencies of prospective rate 6 and simulated retrospective rate 6 are very similar.

Figure 3.2

BLOSM-SENSE exploits matrix low-rank sparsity within motion-tracked regions from SENSE-combined images. After the multi-channel data are combined with SENSE, regions (blocks) are initialized on the first image. Each block is motion tracked to the succeeding images through time using motion trajectories from image registration. The blocks are gathered into a 3D cluster and further rearranged into a 2D matrix with high spatial-temporal correlations. The sparsity is exploited using singular value decomposition.

Figure 3.3 Example reconstruction images using BLOSM (A-L) and k-t SLR (a-l) at various acceleration rates. Images from prospectively accelerated rate-4 scan (A-C,a-c) and corresponding retrospectively sub-sampled rate-6 (D-F, d-f) and rate-8 (G-I, g-i) were shown in the top panel. Images from prospectively accelerated rate-6 scan (J-L, j-l) were shown in the bottom. Images at early, mid and late time points were shown in different columns. The top panel images present strong respiratory motions. BLOSM reconstructions showed the best image quality with respect to noise removal and motion preservation. The BLOSM quality preserved with increased sub-sampling rates. k-t SLR suffered from blurring for all accelerations. In the Pro R6 study, BLOSM presented consistent high image quality. K-t SLR presented similar quality as BLOSM, since the images presented few motions in this study.

Figure 3.4 Example vertical (y-t) and horizontal (x-t) spatial-temporal profiles across the heart from BLOSM (A-H) and k-t SLR (a-h). The profiles were obtained using the same example data used in Figure 3.3. For prospective rate-4 (Pro R4, A, B, a, b), retrospective rate-6 (Retro R6, C, D, c, d) and retrospective rate-8 data (Retro R8, E, F, e, f), strong respiratory motions can be observed in both directions. The BLOSM reconstruction provided clear motion depiction while the k-t SLR presented severe motion blurring at all acceleration rates. Limited motion can be observed from the prospective rate-6 (Pro R6, G, H, g, h) data, and BLOSM and k-t SLR performed similarly in this case, although some subtle motion blurring can still be observed on the k-t SLR reconstruction.

Figure 3.5 Example BLOSM reconstruction results from one patient with amyloidosis. Multi-slice images from one time point are shown (A-C), along with the x-t profile (D) and a corresponding LGE image (I). A subendocardial perfusion defect is clearly depicted by BLOSM, even in the presence of respiratory motion during the scan, as illustrated in the x-t profile. The subendocardial perfusion defect location matched closely with enhancement on the LGE image.

Figure 3.6 Example images at one time point reconstructed using different threshold level. The threshold level increases from left to right, representing stronger regularization. Data at different acceleration rates reconstructed by BLOSM and k-t SLR are shown in different rows. BLOSM presented good noise removal performance at all levels of thresholding. Subtle increase of motion blurring can be observed as the threshold level increases in BLOSM. In contrast, images reconstructed by k-t SLR presented high level of residual artifacts at low threshold level. The artifacts were removed at the cost of increased motion blurring in k-t SLR.

Figure 3.7 Example standard deviation of signals from a background region over a wide range of threshold levels. Signals were obtained from the same images reconstructed by BLOSM and k-t SLR shown in Figure 7. High threshold values are needed in k-t SLR to match the same noise level in BLOSM. At low threshold level where k-t SLR presented moderate motion blurring, the noise level is much higher than BLOSM.

Figure 4.1 BLOSM-SENSE reconstruction of 2D cine DENSE. The reconstruction includes: calculation of sensitivity maps (stage 1) and BLOSM-SENSE reconstruction (stage 2). The undersampled phase-cycled raw k-space data

are first subtracted to remove T1-relaxation echoes. The subtracted undersampled stimulated echoes undergo a linear combination to extract the background phase reference stimulated echo. The phase reference data are transformed into images, averaged over time and eigen-analysis is applied to obtain coil sensitivity maps. At the second stage, the undersampled stimulated echoes subtracted from the undersampled raw-k-space data are input for the BLOSM-SENSE CS-PI algorithm. BLOSM-SENSE uses the calculated sensitivity maps to exploit matrix low-rank sparsity within motion-tracked regions from SENSE-combined images. The final outputs of the iterative BLOSM-SENSE reconstruction are magnitude images and phase images with orthogonal 2D displacement encoding.

Figure 4.2

Example reconstructions of retrospectively rate-4 undersampled images from a computer simulated cardiac-contraction phantom. Magnitude (A-E) and phase (J-N) images with displacement encoding applied in the x direction at end-systole are shown. Fully-sampled data reconstructed with NUFFT (A,J) and accelerated data reconstructed using BLOSM-SENSE with joint encoding (B,K), BLOSM-SENSE with independent encoding (C,L), k-t SPARSE-SENSE (D,M) and zero-filled NUFFT (under-sampled) (E,N) are shown in different columns. Difference images (F-I,O-R) computed by subtracting reconstructed images from fully-sampled images are also shown (difference amplified by 5 and 50 times for magnitude and phase images, respectively, for display purposes). BLOSM-SENSE with joint encoding presented the smallest error and best agreement with the fully-sampled data.

Figure 4.3 Root mean square error (RMSE) analysis of the performance of various reconstruction methods applied to a computer-simulated cardiac-contraction phantom at different undersampling rates. RMSE of the complex-valued images is shown in (A). Regional RMSE over the myocardium of the phase images was calculated and shown in (B). At the lower acceleration rate of 2, all CS-based algorithms performed similarly and showed lower complex RMSE compared to the zero-filled NUFFT reconstruction (Under-sampled). At higher acceleration rates of 4 and 8, BLOSM-SENSE with joint encoding showed advantages over the other methods using both complex and phase data.

Figure 4.4 Linear regression (A-C) and Bland-Altman analysis (D-E) of Ecc calculated from BLOSM-SENSE with joint encoding compared to fully-sampled reconstructions for computer-simulated phantoms. Results from retrospectively rate-2, rate-4 and rate-8 are shown. Excellent agreement was achieved at all acceleration rates. Note that the y-axis range on the Bland-Altman graphs are much smaller than the Ecc range.

Figure 4.5 Example reconstructions of retrospectively rate-4 (A-L) and prospectively rate-4 (M-V) undersampled images from a healthy volunteer. Magnitude and phase images with displacement encoding applied in the x direction at end-systole are shown. Fully-sampled data reconstructed with NUFFT (A,G) and accelerated data reconstructed using BLOSM-SENSE with joint encoding (B,H,M,R), BLOSM-SENSE with independent encoding (C,I,N,S), k-t SPARSE-SENSE (D,J,O,T), SENSE (E,K,P,U) and zero-filled NUFFT-SOS-combined (under-sampled) (F,L,Q,V) methods are

shown. All CS-PI combined methods achieved better image quality than SENSE.

Figure 4.6 Quantitative analysis of the performance of various reconstruction methods applied to in vivo imaging of volunteers. Root mean square error (RMSE) and signal-to-noise ratio (SNR) are shown, with error bars indicating one standard deviation. (A) RMSE of the complex-valued images; (B) Regional RMSE over the myocardium of the phase images; (C) SNR values. At a low acceleration rate of 2, all methods offered similar RMSE, although CS-PI presented higher SNR. At a higher acceleration rate of 4, CS-PI showed improvement over SENSE. Specifically, BLOSM-SENSE with joint encoding showed significantly lower RMSE compared to the other methods at rate-4 acceleration for complex and phase data (* $P < 0.05$, ANOVA). For rate-2 acceleration, the lower RMSE of BLOSM-SENSE with joint encoding was statistically significant compared to the undersampled data reconstructed using SOS (# $P < 0.05$, ANOVA). BLOSM-SENSE with joint encoding showed significantly higher SNR compared to all other reconstruction methods (* $P < 0.05$, ANOVA).

Figure 4.7 Linear regression (A-D) and Bland-Altman analysis (E-H) of Ecc using BLOSM-SENSE with joint encoding compared to fully-sampled reconstructions for in vivo imaging of volunteers. Results from retrospectively rate-2 (A,E) and rate-4 (B,F) and prospectively rate-2 (C,G) and rate-4 (D,H) are shown. Good agreement was achieved at all acceleration rates. Agreement was better for retrospectively undersampled data compared to prospectively accelerated data, likely due to differences in breathholding between different acquisitions.

Figure 4.8 Example BLOSM-accelerated 3D cine DENSE images. Three short-axis (SA) views at base, mid and apex locations, along with one long-axis (LA) views are shown in different rows. The magnitude images (A-D) show clear delineation of the myocardium. All the phase images with displacement encodings in x (E-H), y (I-L) and z (M-P) show clear phase information that can be utilized for strain analysis.

Figure 4.9 Example 3D voxel-wise strain maps of the LV at end systole. Radial (E_{rr}), circumferential (E_{cc}) and longitudinal strain (E_{ll}) maps show values in the range of normal subjects.

List of Symbols

$\mathbf{B}(\mathbf{u}_1)$	Square block of pixels centered at \mathbf{u}_1
c_1	Variable to stabilize average term in SSIM calculation
c_2	Variable to stabilize variance term in SSIM calculation
\mathbf{d}	Measured k-space data
$\text{diag}()$	Take the diagonal of a matrix
$\mathcal{D}_{\lambda,p}$	Singular value soft thresholding operator, with thresholding level of λ and norm order of p
ϵ	Error level
E_{cc}	Circumferential strain
E_{cc_ref}	Reference circumferential strain
\mathcal{F}_u	Undersampled fast Fourier transform operator, with undersampling of u
\mathbf{G}_c	Common gap mask
\mathbf{G}_n	Gap mask on the n_{th} frame
i	Iteration number
Im_t	Image at time of t
\mathbf{k}_e	Displacement encoding frequency
k_x	k-space spatial frequency, corresponding to x
k_y	k-space spatial frequency, corresponding to y
$k\text{-}t$	k-space and time
$k_y\text{-}t$	k_y and time
ℓ_0	ℓ_0 norm

ℓ_1	ℓ_1 norm
\mathbf{m}	Dynamic images
\mathbf{m}^i	Dynamic image from the i_{th} iteration
\mathbf{m}^i	Auxiliary dynamic image from the i_{th} iteration
$\mathbf{m}(t_1)$	Image at time t_1
\mathbf{m}_c	Coil-combined dynamic images
$\max(\)$	Take the maximum number
N	Number of entities
N_{acc}	Acceleration rate
N_b	Number of entities in a block
N_{enc}	Number of displacement-encoding directions
N_{leaves}	Number of spiral interleaves
N_{phcyc}	Number of phase-cycling factor
N_s	Number of entities in a cluster
N_{segment}	Number of spiral interleaves acquired per heartbeat
N_t	Number of image frames in time
N_x	Dimension of 2D matrix, along x
N_y	Dimension of 2D matrix, along y
p	Order of nuclear norm
\mathbf{R}	Displacement map
R^2	Coefficient of determination
$\mathcal{R}(\mathbf{u}_1)$	Displacement of block centered at \mathbf{u}_1
\mathbf{S}	Coil sensitivities
\mathbf{S}_{bg}	Regional signal from the background

$\text{signum}()$	Sign function
\mathbf{S}_{obj}	Regional signal from the imaged object
$\overline{\mathbf{S}_{\text{obj}}}$	Averaged regional signal from the imaged object
$\text{soft}()$	Soft thresholding operator
\mathcal{S}_w	Weighted averaging operator
t	Time
$T1$	Spin-lattice time constant
u	Undersampling mask
\mathbf{U}	Left matrix from singular value decomposition
\mathbf{V}^*	Hermitian conjugate of Right matrix from singular value decomposition
x	Spatial coordinate in the x axis
\mathbf{x}	A 2D image
y	Spatial coordinate in the y axis
\mathbf{y}	A 2D image
$x\text{-}f$	Spatial-temporal-frequency
$x\text{-}t$	Spatiotemporal profile with vertical spatial direction
$y\text{-}t$	Spatiotemporal profile with horizontal spatial direction
\mathbf{Z}	Spatiotemporal 2D Casaroti matrix
γ	Number be soft-thresholded
δ	Step size
λ	Thresholding level
Σ	Center matrix containing singular values from singular value decomposition
\mathcal{E}	Cluster of blocks
\mathcal{E}	Group of clusters

μ	Mean value
$\mu_{\mathbf{x}}$	Mean value of image \mathbf{x}
θ	Phase of the complex value
Φ	Sparsity transform
$\Phi_{\mathcal{R}}$	Sparsity transform with motion-guidance
φ	Background phase
σ^2	Variance
$\sigma_{\mathbf{x}}$	Variance of image \mathbf{x}
$\sigma_{\mathbf{xy}}$	Covariance of images \mathbf{x} and \mathbf{y}
$\Delta \mathbf{t}$	Change in time
$\Delta \mathbf{u}$	Change in block
$\Delta \mathbf{x}$	Change in position along x-axis
$\Delta \mathbf{y}$	Change in position along y-axis
$\nabla \mathbf{t}$	Gradient along time direction
$\{ \}$	Take the integer
$\{ \}_{2\pi}$	Take the modulus of 2π
$\ \cdot \ _2$	Norm 2
$\ \cdot \ _{\ell_0}$	Norm ℓ_0
$\ \cdot \ _{p^*}$	Joint Schatten p -norm

List of Abbreviations

1D	One-Dimensional
1.5 T	1.5 Tesla
2D	Two-Dimensional
2DFT	2D Fourier Transform
3D	Three-Dimensional
3T	3 Tesla
Acc. rate	Acceleration Rate
AIF	Arterial Input Function
ANTS	Advanced Normalization Tools
ANOVA	ANalysis Of VAriance
avg.	Average
BIR4	B1-Independent Refocusing 4 pulse
BLOSM	Block LOw-rank Sparsity with Motion-guidance
BLOSM-SENSE	BLOSM with SENSE
BLOSM-SENSE-ind	BLOSM-SENSE with independent encoding sparsity
BLOSM-SENSE-joint	BLOSM-SENSE with joint encoding sparsity
CMR	Cardiac Magnetic Resonance imaging
CPU	Central Processing Unit
CS	Compressed Sensing
CTF	Coarse-To-Fine
DENSE	Displacement ENcoding with Stimulated Echoes
ECG	ElectroCardioGraphy

F.T.	Fourier Transform
FFT	Fast Fourier Transform
FLASH	Fast Low Angle SHot
FOV	Field Of View
GB	GigaByte
gMG	global Motion Guidance
GPU	Graphic Processing Unit
ISMRM	International Society of Magnetic Resonance in Medicine
IST	Iterative Soft Thresholding
kg	kilogram
k-t PCA	k-t Principal Component Analysis
k-t FOCUS	k-t FOCal Underdetermined System Solver
k-t SLR	k-t Sparsity and Low-Rank
LGE	Late Gadolinium Enhancement
LOST	LOW-dimensional-structure Self-learning and Thresholding
LV	Left Ventricle
MASTeR	Motion-Adaptive Spatio-Temporal Regularization (MASTeR)
ME/MC	Motion Estimation / Motion Compensation
MG	Motion Guidance
MGS	Motion Guided Segmentation
mm	millimeter
mmol	millimolar
MRI	Magnetic Resonance Imaging
ms	millisecond
MSE	Mean Square Error

MOLLI	MOdified Look-Locker Imaging
NP-hard	Non-deterministic Polynomial-time hard
NUFFT	Non-Uniform Fast Fourier Transform
P1	Phantom One
PI	Parallel Imaging
PCA	Principal Component Analysis
Pro.	Prospective
Pro R4	Prospective Rate 4
Pro R6	Prospective Rate 6
RAM	Random-Access Memory
Ref.	Reference
Retro.	Retrospective
Retro R6	Retrospective Rate 6
Retro R8	Retrospective Rate 8
RF	Radio Frequency
RMSE	Root Mean Square Error
rRMSE	relative Root Mean Square Error
ROI	Region Of Interest
SENSE	SENSitivity Encoding
SNR	Signal-to-Noise Ratio
SoS	Sum-of-Square
SPIRiT	Iterative Self-consistent Parallel Imaging Reconstruction
SSFP	Steady State Free Precession
SSIM	Structural SIMilarity
Stddev.	Standard deviation

SV	Singular Value
SVD	Singular Value Decomposition
s.t.	such that
TE	Echo Time
TF	Tissue Function
TI	Inversion Time
TR	Repetition Time
w/	with
w/o	without

Chapter 1

Introduction

1.1 Cardiac Magnetic Resonance Imaging

Magnetic resonance imaging (MRI), as a relatively new member of the medical imaging modality family, has developed over the past three decades into a powerful tool and is now playing important roles in many medical applications. MRI provides excellent soft tissue contrast with no ionizing radiation exposure, which makes it well suited for cardiac imaging. Tremendous efforts have been made and have proven that cardiac MRI (CMR) can provide accurate assessment of cardiac morphology, function, perfusion and myocardial viability (1-3), the comprehensive capability of which cannot be competed by any other single imaging modality (1). Dynamic imaging, where a time series of images are acquired, is commonly used in CMR to capture the changing phenomena in the cardiovascular system. However, the data acquisition speed of MRI is relatively slow. Fast imaging techniques are demanded in CMR to match the data acquisition speed with the physiological changing speed.

1.2 MRI data

The raw data collected by MRI, rather than the image itself, is the spatial frequency information. A Fourier transform relationship exists between the image space and the MRI data

space, usually referred to as k-space (Figure 1.1). If the k-space data is collected following the Nyquist-Shannon sampling rule, the acquisition is referred to as a “fully-sampled” acquisition. In the fully-sampled case, specified by the desired spatial resolution and the size of the field of view (FOV), a certain amount of data are distributed in the k-space with a certain density. If higher spatial resolution or bigger FOV is desired without compromising the other imaging protocols, more k-space data must be collected, which leads to increased scan time. In CMR, a short data acquisition window is usually used to restrain cardiorespiratory motion or other physiological changes in each image. On the other hand, a large amount of k-space data is needed for accurate prognosis and diagnosis, where high spatial-resolution images to delineate thin structures or small abnormality regions, and high spatial-coverage images to cover the whole heart are desired. To address this dilemma, acceleration of data acquisition is commonly performed for CMR dynamic imaging.

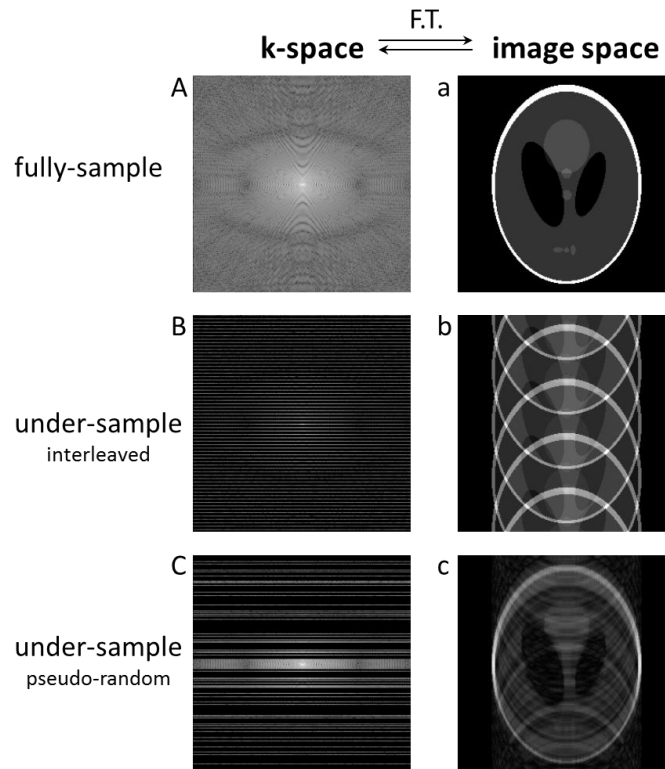


Figure 1.1 Fourier transform relationship between k-space data (A-C) and image space image (a-c) in MRI. Fully-sampled k-space (A) reconstructed by Fourier transform (F.T.) present no image artifacts (a). Undersampled k-space data in an interleaved pattern (B) leads to aliasing artifacts (b). Undersampled k-space data in a pseudo-random pattern (C) leads to blurring artifacts (c).

1.3 MRI acceleration

Data acquisition acceleration can be achieved by collecting a reduced amount of data relative to the fully-sampled data, referred to as “undersampling”. An acceleration rate N_{acc} acquisition means that only $1/N_{acc}$ of the fully-sampled data is acquired and the data acquisition time is shortened to $1/N_{acc}$ of the fully-sampled time. However, the undersampling violates the Nyquist-Shannon sampling theorem and the images reconstructed by Fourier transform alone will be contaminated by artifacts such as aliasing or blurring, as illustrated in Figure 1.1.

To obtain artifact-free or artifact-reduced images from undersampled MRI data, various fast imaging techniques have been proposed. Some of them exploit data correlations in the spatial-frequency structure, such as partial Fourier (4). Some of the methods exploit data correlations along temporal direction for dynamic imaging, such as UNFOLD (5) and keyhole (6). With the development of phased-array RF coil acquisition, parallel imaging techniques such as SENSE (7) and GRAPPA (8) that exploit correlations among coils have been widely used in clinical and research MR scans. However, these methods usually gain the acceleration at the cost of degraded image quality (signal-to-noise ratio, temporal-resolution, spatial-resolution etc.) and thus the applicable acceleration rate is limited, ranging from rate 2 to rate 4 for clinical scans.

1.4 Compressed sensing

The compressed sensing theory (9) was introduced to MR imaging around 2007 and has had a big influence to the field since then (10). Using CS, a high acceleration rate can be achieved with little or no cost of image quality, unlike the other conventional fast imaging techniques. The CS theory is based on the fact that most natural images, including medical images, present redundant information which can be utilized to decrease the amount of measurements without sacrificing the reconstruction quality. The data redundancy is represented as the concept of “sparsity” in the CS theory, which defines that a sparse data has a small amount of non-zero-value entries. A transform of the data can be used to “sparsify” the data, namely that transforming the data into certain domain, referred as the “sparsity domain”, where it presents sparsity. The transform is referred as the “sparsity transform”.

A successful CS reconstruction requires that the sampling (data measurement) is random, the images present sparsity, and a non-linear process is taken to reconstruct the images (10). The image reconstruction can be formulated into an optimization problem

$$\begin{aligned} & \text{minimize}_m \|\Phi \mathbf{m}\|_{\ell_0} && [1.1] \\ & \text{s. t. } \|\mathcal{F}_u \mathbf{m} - \mathbf{d}\|_2 < \epsilon \end{aligned}$$

where Φ is the sparsity transform, $\|\cdot\|_{\ell_0}$ is the ℓ_0 norm which counts the number of zeros, \mathbf{d} is the undersampled data acquired in the k-space, \mathbf{m} is the estimated image/images and \mathcal{F}_u is the undersampled Fourier transform where the subscript u represents the sampling pattern or the sampling mask, which has 1 at the k-space location where the data is sampled and 0 at the location where there is no sampling. The ℓ_0 norm minimization promotes the sparsity and the constraint bounds the solution to the existing measurement \mathbf{d} . The final reconstructed images will be the solution of the optimization problem.

In reality, the ℓ_0 norm is an NP-hard problem and is usually approximated by ℓ_1 norm or other types of norms. Conditions exist that the solution from those approximated norms can be similar or the same as the ℓ_0 norm problem (11).

1.5 Sparsity in dynamic CMR images

The possibility of a successful CS reconstruction relies on the sparsity level of the data (9). With a given data, the sparsity level is decided by how well the sparsity transform can sparsify the data. The higher sparsity level can translate into either higher acceleration rate (fewer measurements) or better image quality.

Dynamic CMR is inherently suitable for CS acceleration because both spatial and temporal sparsity can be exploited. However, different CMR applications present a wide range of dynamic behaviors in the images. The CS sparsifying transform should be chosen wisely to handle different types of dynamics.

The dynamics in CMR may be broadly divided into three groups, with each group having its own suitable data sparsity domain and corresponding CS algorithm.

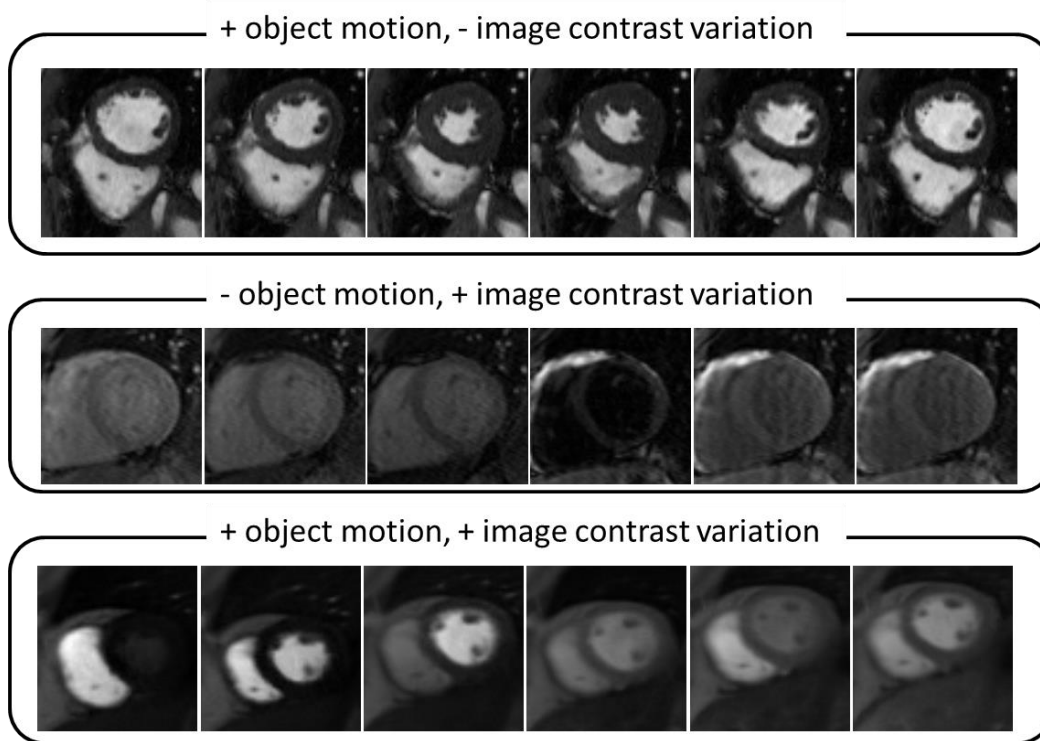


Figure 1.2 Three types of dynamics in dynamic CMR images. 1st row is balanced SSFP images. 2nd row is modified Look-Locker images. 3rd row is first-pass perfusion images. Example images at different time points are shown.

1.5.1 Object motion, no change in image contrast

Example images include cine balanced SSFP images of the heart (Figure 1.2, 1st row).

With periodic or close to periodic motions, these images present sparsity in the spatial-temporal-

frequency domain (x-f domain) (12). CS algorithms such as kt-SPARSE utilize x-f sparsity and have achieved acceleration rates up to 4 (12).

1.5.2 Smoothly-changing image contrast, no object motion

Example images include modified Look-Locker (MOLLI) images (Figure 1.2, 2nd row), which are routinely used for T1 mapping in the heart. With no motion, the signal at each pixel is smoothly changing and thus the consecutive two images in time have little difference. CS algorithms using 1st and 2nd order temporal differences as the sparsity transform can effectively sparsify this type of dynamics. Rate 4 acceleration has been achieved on these images (13,14).

1.5.3 Object motion and changes in image contrast

This category represents the most complex dynamics. Examples include first-pass perfusion images with respiratory motion (Figure 1.2, 3rd row) and cine Displacement ENcoding with Stimulated Echoes (DENSE) imaging. The motion invalidates the temporal sparsity constraint, as pixels in the image may have sharp discontinuities in signal intensity, causing CS reconstruction algorithms such as the temporal difference to fail. The complex dynamics also broaden the temporal frequency spectrum and decrease the x-f domain sparsity, causing CS reconstruction algorithms such as the x-f transform to fail (15,16).

1.6 CS for complex dynamics

To apply CS to CMR dynamic imaging with complex dynamics, several methods have been proposed, the majority of which can be categorized into three basic strategies.

1.6.1 Data-driven sparsity transform

The first strategy is to use a robust sparsifying transform that can sparsify signals regardless of the signal changing sources, either due to motion or due to image contrast changes. One solution is to use data-driven basis-function transform, instead of a fixed basis-function such as the Fourier transform. Underlying spatial and/or temporal patterns (basis functions) in the data are estimated from some training data or the data itself, and the acquired data are decomposed into a linear weighted summation of these basis functions. The weighting of these basis functions (or scores) are sparse, given that only a few underlying patterns exist in the images and are successfully estimated, as illustrated in Figure 1.3. Example methods include partially separable functions (PSF) (17), k-t principal component analysis (k-t PCA) (18), and k-t sparsity and low-rank (k-t SLR) (19). While these methods showed promising improvement over the fixed basis function transforms, images with large and rapid motions lead to decreased accuracy of pattern estimations and further lead to decreased reconstruction quality.

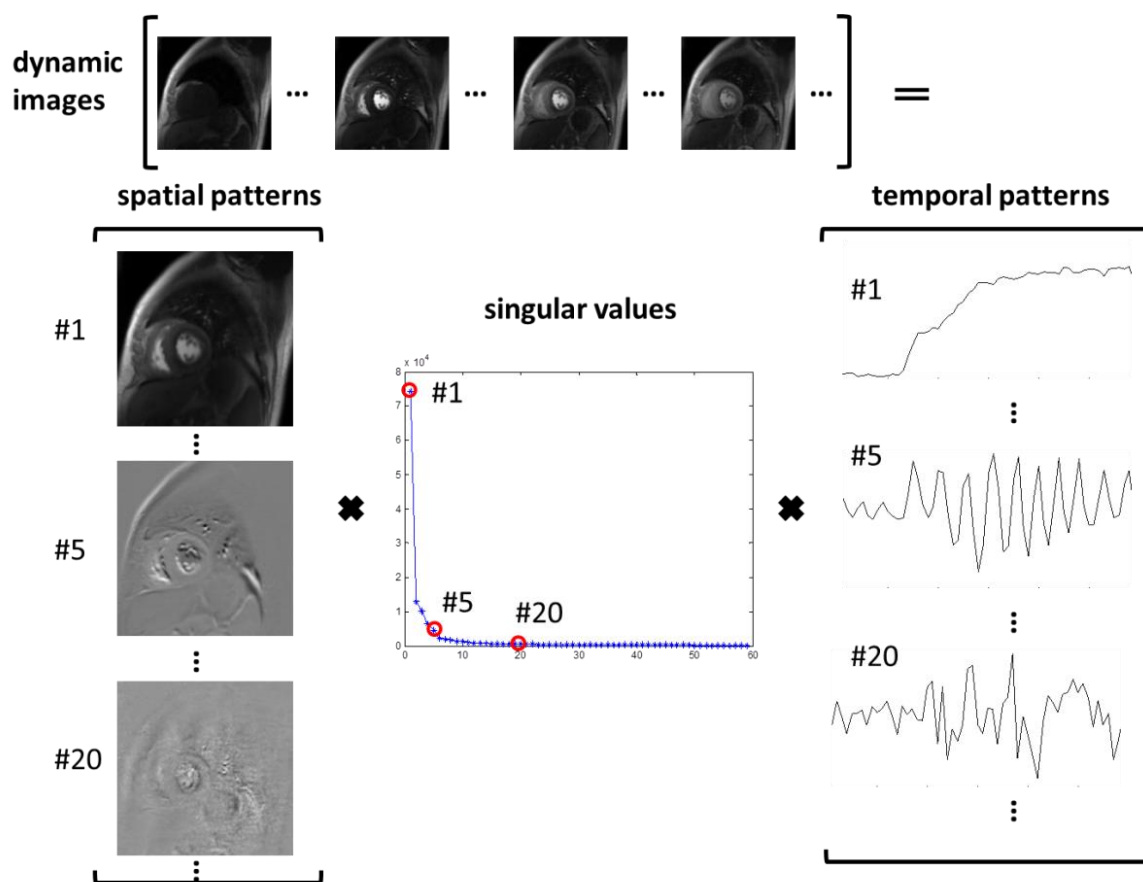


Figure 1.3 Illustration of data-driven basis function analysis of dynamic images. The dynamic images can be decomposed to a multiplication of three matrices referred as singular value decomposition, where the first matrix contains basis spatial patterns, the last matrix contains basis temporal patterns and the center matrix contains the singular values representing the weightings of the patterns. Big singular value (#1) means big contribution of the corresponding patterns (#1 in the spatial pattern and in the temporal pattern) in the dynamic images. Small singular value mostly represent noise in the dynamic images.

1.6.2 Motion-guided CS

The second strategy is to utilize the concept of motion-compensation/-guidance. The motion-compensated CS simplifies the dynamics in the images by generating motion-corrected or registered images. The dynamics-simplified images now present contrast changes with little

or no motion, and eases the job of the sparsifying transform, as illustrated in Figure 1.4. The motion-compensation has been successfully combined with sparsity transform such as temporal difference (20-22) and x-f transform (16,23). One drawback of these motion-compensated CS methods is that the quality of the reconstruction relies heavily on the accuracy of the motion estimation. This might be a challenging task for CS reconstruction since the motions need to be estimated from artifact contaminated images in the early CS iterative calculation due to undersampling. Another drawback is that the implementation of these methods usually requires spatial interpolation, which tends to generate additional blurring artifacts in the final reconstructed images.

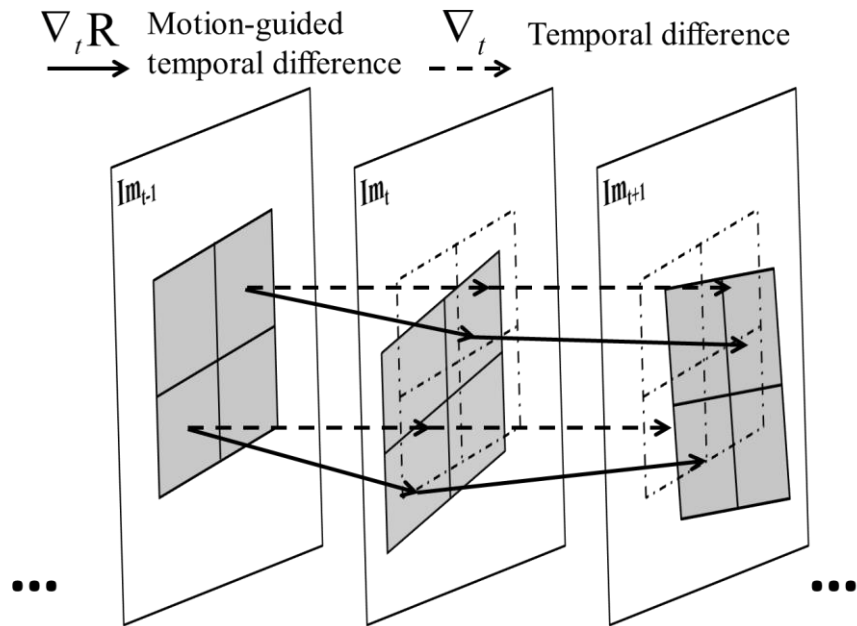


Figure 1.4 Motion guidance is required to compute the correct image temporal difference. Im_{t-1} , Im_t and Im_{t+1} are three consecutive dynamic images in time. When motion occurs between Im_{t-1} , Im_t and Im_{t+1} (from dashed frame to solid frame), the temporal difference from motion-corrected images (solid arrow) is correctly computed, while the temporal difference calculated from non-motion-corrected images (dashed arrow) is incorrect due to mis-registration.

1.6.3. Regional sparsity

Another strategy is to divide the dynamic images into sub-regions, where sparsity transform is separately applied to each region. It is hypothesized that simplified dynamics can be achieved within a small scope of the image. Methods includes LOST (24), compartment-based k-t PCA (25) and localized spatio-temporal constraints (26). These methods present promising quality improvement; however, large motion remains a problem. These studies were proposed during a similar period of the work presented in this dissertation.

1.7 K-T sampling pattern

According to the CS theory, the sampling or the data measurement should be random to generate incoherent artifacts due to undersampling (10). This can be realized by positioning the sampling point randomly in the k-space (Figure 1.5). Since both spatial and temporal redundancies are exploited in dynamic CMR CS applications, randomness should be presented both in k-space and time, and thus a k-t sampling pattern is commonly adopted. In MRI, because of most of the image energy resides at the center low spatial-frequency portions of the k-space, a variable density k-t sampling pattern is usually used for dynamic CMR undersampling, where the high spatial frequencies are randomly sampled at a lower possibility, while the center low spatial frequencies are more densely sampled or even fully-sampled. Example k-t sampling patterns are illustrated in Figure 1.5.

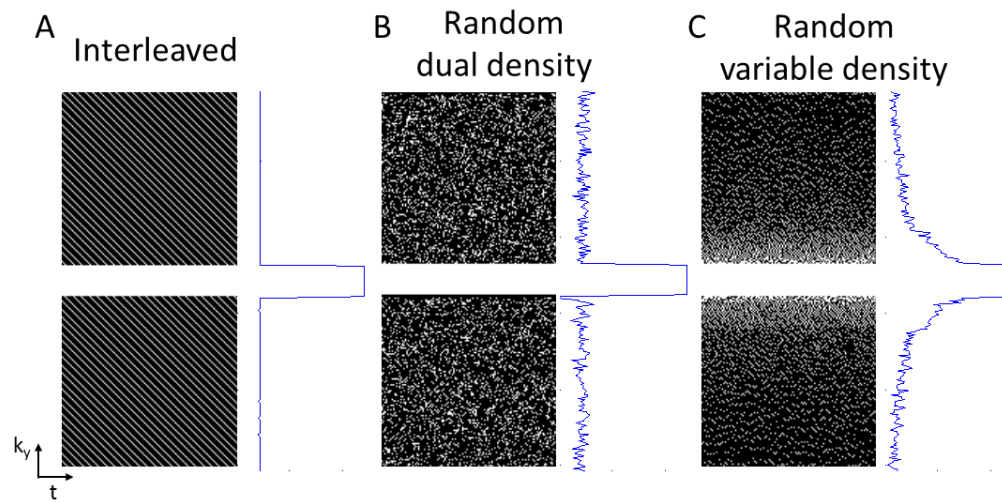


Figure 1.5 Example k-t sampling patterns and sampling frequencies of interleaved (A) random with dual density (B) and random with variable density (C). Each point on the sampling pattern represents one phase-encoding k_y line in the k-space at time t . White points mean the data is sampled and the three patterns shown here have the same number sampling points.

1.8 Cardiac first-pass perfusion

CMR first-pass perfusion imaging assesses regional myocardial blood flow and is becoming an important tool for noninvasive assessment of coronary artery disease (27,28). The imaging process includes electrocardiography (ECG) triggered data acquisition of a time series of images during the first passage of gadolinium through the heart (29). Myocardium perfused by the gadolinium in the blood will show hyperintense signal, while perfusion defect regions will show hypointense signal (30). The imaging occurs during the first few passages of the injected contrast through the heart, which usually only lasts for a few heartbeats. Temporal resolution of one image per heartbeat is required to capture this fast changing phenomenon, providing a short data acquisition window. On the other hand, high spatial resolution images are desired to reveal

subtle perfusion defect regions and to decrease dark rim artifacts (31). High spatial coverage such as multi-slice 2D acquisition or 3D acquisition is preferred to offer whole heart coverage. To freeze respiratory motion, breathholding is required during the entire scan. However, even when patients are instructed to suspend respiration for 15-20 seconds, they are often unable to comply fully with instructions and they breathe during the scan. The problem of imperfect breathholding and associated respiratory motion presents a major challenge to CS-acceleration of first-pass cardiac MRI (15,16,19).

1.9 Cine Displacement ENcoding with Stimulated Echoes (DENSE)

Imaging myocardial strain is of growing importance for the clinical assessment of heart disease (3,32-34). MRI myocardial tagging, a long-established method, has been considered the gold standard as compared to strain imaging using echocardiography (34,35). However, recently within the MRI modality, cine displacement encoding with stimulated echoes (DENSE) (36-38) has emerged as a strain imaging technique that, compared to tagging, has equivalent accuracy and better reproducibility (39), and where strain analysis is less time consuming (35,40,41). While cine DENSE holds these advantages, it also has the disadvantage that data acquisition times are relatively long. Currently, tagged images using two-dimensional (2D) grid tags are typically acquired during a single breathhold (34), whereas common protocols for 2D cine DENSE typically require two separate breathholds, each with 1D displacement encoding (42). Acceleration using data undersampling could substantially shorten the scan time and/or provide

improved temporal resolution for cine DENSE. However, the relatively low signal-to-noise ratio (SNR) inherent to stimulated echoes presents challenges to acceleration techniques such as parallel imaging (PI), which reduce scan time at the expense of SNR (43). Cine DENSE encodes object displacement directly into the phase of the complex-valued images and thus complex-valued image reconstruction is required. The images feature cardiac contraction and relaxation coupled with signal intensity changes due to T1 relaxation of the stimulated echo (Figure 1.6). All these present challenging task for CS acceleration.

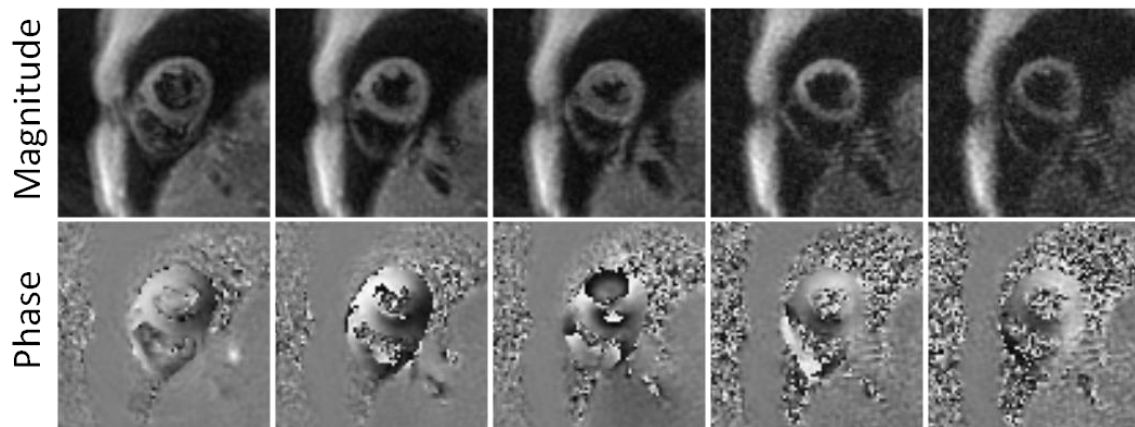


Figure 1.6 Example cine DENSE images from different cardiac phases. Magnitude images are shown on the top row and phase images with displacement encoded in the vertical direction are shown on the bottom row. Cardiac contraction motion along with signal intensity changes can be observed on the images.

1.10 Retrospective acceleration study and prospective acceleration study

To evaluate a CS method, two types of studies are commonly conducted. The first is a retrospective acceleration study, where fully-sampled data is acquired and serves as the reference images. To simulate undersampling, certain amount of data points are removed from the fully-

sampled data to match the desired acceleration rate. The retrospective undersampled data is reconstructed by the image reconstruction methods of interest and quantitative performance assessment can be realized by comparing the reconstructed images to the reference images. The second type is a prospective acceleration study, where decreased amount of data is directly collected using the designed undersampling pattern and thus the data acquisition can benefit from the acceleration. The prospectively accelerated data is reconstructed by the image reconstruction methods as in the retrospective study, while due to the lack of reference images, direct comparison is usually not available. The reconstruction result can be compared to separately-acquired fully-sampled data. Blind image quality assessment, such as quality score, can also be performed.

1.11 Dissertation Aims

In this study, our goal was to develop and evaluate motion-compensated regional-sparsity-based CS-accelerated methods for imaging complex cardiovascular kinetics including both signal variation and cardiorespiratory motion. .

Specific aim #1 was to develop a CS algorithm that can handle complex dynamics. (a) Develop a motion-compensated CS method that exploits regional spatiotemporal sparsity. (b) Validate the CS method using simulated and in vivo data and compare the proposed method to other CS methods.

Specific aim #2 was to accelerate first-pass perfusion imaging in patients with suspected heart disease. (a) Increase reconstruction quality and further accelerate data acquisition by adding parallel imaging to the CS method. (b) Implement accelerated first-pass sequence and

collect patient data. (c) Validate the CS method using the patient data and compare the proposed method to other CS methods.

Specific aim #3 was to accelerate cine DENSE imaging using the CS methods developed in aims #1 and 2. (a) Develop a variable-density spiral cine DENSE sequence with golden angle rotation through time for CS acceleration. (b) Validate the CS method using simulated and in vivo data and compare the method to existing parallel imaging techniques and other CS methods.

1.12 Dissertation Overview

This dissertation is organized as follows.

Chapter 1 provides the background of the dissertation. Specific aims and the structure of this dissertation are introduced.

Chapter 2 presents the CS method developed in this dissertation and its validation study using retrospectively accelerated first-pass cardiac perfusion and computer simulated phantom data. BLOSM was systematically compared to several other CS methods. Key points of BLOSM are verified and discussed. This chapter covers the content of specific aim #1. The main material in this chapter is published in a full paper titled “Motion-compensated compressed sensing for dynamic contrast-enhanced MRI using regional spatiotemporal sparsity and region tracking: Block LOW-rank Sparsity with Motion-guidance (BLOSM)” in *Magnetic Resonance in Medicine* 2014,72(4):1028-38. The paper also entered the semi-final of 2014 ISMRM young investigator I.I.Rabi award in basic science. The material is published as several conference abstracts as well, including oral and poster presentations.

Chapter 3 presents the study of prospectively accelerated first-pass perfusion imaging in patients with suspected heart disease using BLOSM. BLOSM was combined with parallel imaging to handle multi-coil data. High-quality reconstruction was achieved in 12 heart-disease patients using BLOSM at different acceleration rates, even when substantial respiratory motion occurred. This chapter covers the content of specific aim #2. Some material in this chapter is accepted as an oral presentation at 2015 annual meeting of Society of Cardiac Magnetic Resonance, titled “Prospectively accelerated first-pass myocardial perfusion imaging in patients using motion-compensated compressed sensing exploiting regional low-rank sparsity”. A full paper manuscript on this work is under preparation.

Chapter 4 presents the study of accelerated 2D cine DENSE imaging using BLOSM. Single breathhold 2D myocardium strain mapping in 8 heartbeats was realized in 10 volunteers using BLOSM. Both retrospective and prospective studies were conducted. Image quality and cardiac function assessments showed BLOSM provided high image quality and accurate function assessment from highly accelerated cine DENSE scan. The content of this chapter covers specific aim #3. The material has been published in several conference abstracts, including “Accelerated Cine DENSE using Variable Density Spirals and Compressed Sensing with Parallel Imaging” in Proceedings of ISMRM 2014. A full paper is in preparation.

Chapter 5 summarizes the work of this dissertation and discusses the future work.

Appendix lists all the journal paper publications, patents and conference abstracts of the author during this Ph.D. study.

Chapter 2

BLOSM: Block LOW-rank Sparsity with Motion-guidance

Dynamic contrast-enhanced MRI of the heart is well-suited for acceleration with compressed sensing (44) due to its spatiotemporal sparsity; however, respiratory motion can degrade sparsity and lead to image artifacts (15,16,19,21,23,45-47). A novel compressed sensing method, Block LOW-rank Sparsity with Motion-guidance (BLOSM), was developed to accelerate first-pass cardiac MRI, even in the presence of respiratory motion. This method divides the images into regions, tracks the regions through time, and applies matrix low-rank sparsity to the tracked regions. BLOSM was evaluated using computer simulations and first-pass cardiac datasets from human subjects. Using retrospectively rate-4 accelerated data, BLOSM was compared to other CS methods such as k-t SLR that employs matrix low-rank sparsity applied to the whole image dataset, with and without motion tracking, and to k-t FOCUSS with motion estimation and compensation that employs spatial and temporal-frequency sparsity. BLOSM was qualitatively shown to reduce artifacts due to respiratory motions compared to other methods. Quantitatively, using root mean squared error and the structural similarity index, BLOSM was superior to other methods. BLOSM, which exploits regional low rank structure and uses region tracking for motion compensation, provides improved image quality for CS-accelerated first-pass cardiac MRI.

2.1 Introduction

Compressed sensing (32), an acceleration technique of growing importance, is making a major impact on MRI (10). Using CS, high-quality images can be recovered from data sampled well below the Nyquist rate provided that the sampling pattern is incoherent, the images are sparse in a transform domain, and a sparsity-promoting iterative reconstruction is used (10). Because of the high temporal and spatial redundancy inherent to dynamic contrast-enhanced MRI, these data can be represented sparsely in a transform domain and are well-suited for acceleration by CS (44). However, patient motion due to respiratory or other factors reduces the spatiotemporal redundancy of the data and, if not corrected, leads to image artifacts (15,16,19-21,23,45-47). The problem of imperfect breathholding and associated respiratory motion presents a major challenge to CS-acceleration of first-pass cardiac MRI, where, even when patients are instructed to suspend respiration for 15-20 seconds, they are often unable to comply fully with instructions and they breathe during the scan.

A number of CS methods have been developed to accelerate dynamic MRI. Early studies such as k-t SPARSE showed that sparsity in the spatial and temporal-frequency (x-f) domain could be exploited to accelerate cine MRI using CS (12,44). The k-t FOCal Underdetermined System Solver (k-t FOCUSS) method made improvements to x-f domain approaches by separating the data into predicted and residual signals, where the predicted signal served as a baseline signal and sparsity was exploited for the residual signal (16). While x-f domain methods combined with parallel imaging have been successfully used for dynamic contrast-enhanced MRI (15), the non-periodic nature of dynamic contrast-enhanced MRI leads to a broader band of temporal frequencies than cine MRI, thus these applications present less x-f sparsity than cine

MRI. For these cases, data-driven spatiotemporal basis functions such as those used in Partially Separable Functions (17) and the k-t Sparsity and Low-Rank (k-t SLR) method (19) may have advantages. For example, the k-t SLR method, which is applied in the image-time domain and exploits matrix rank sparsity by decomposing the signal using singular value decomposition (SVD), has provided quite good image quality for accelerated contrast-enhanced cardiac perfusion imaging (19). However, even while advanced sparsifying transforms such as SVD provide improved image quality, these approaches are still subject to artifacts when respiratory motion or other patient movement occurs.

One approach to handle complex dynamics such as breathing is to extract motion information from the acquired data and apply motion compensation during CS reconstruction. Some studies (23,48) base their work on Batchelor's motion matrix method (49) to correct for respiratory motion in free-breathing or real-time cine imaging. While this approach carefully separates cardiac and respiratory motion, the data binning step limits its extension to wider applications such as dynamic perfusion imaging and relaxation imaging. Another approach is to compensate the image dataset for motion and then apply a CS sparsity transform to the motion-compensated data, such as in k-t FOCUSS with motion estimation and compensation (16) and the recent method of Motion-Adaptive Spatio-Temporal Regularization (MASTeR) (22), as well as other methods (20,21). To date, these methods have employed the temporal difference or x-f methods as the sparsifying transform, and the results clearly demonstrate the advantages afforded by motion compensation.

We sought to develop and evaluate a CS method for first-pass contrast-enhanced cardiac perfusion MRI that combines the advantages of data-driven spatiotemporal basis functions and regional motion tracking. Specifically, we propose a method that divides images into regions,

tracks the regions over time, and applies SVD to the tracked regions. Using this approach, our method can both account for regional non-periodic variations in motion and can exploit regional spatiotemporal sparsity. In our present implementation, the regions are square blocks and we exploit matrix low rank sparsity, thus we have coined the term Block LOw-rank Sparsity with Motion-guidance (BLOSM) to describe this method.

2.2 Methods

2.2.1 BLOSM Overview

The proposed BLOSM method is based on the concept of motion-guided compressed sensing using a regional approach to motion tracking and spatiotemporal sparsity. In BLOSM (as shown in Figure 2.1), blocks of image pixels are defined on one image and tracked through time using motion maps extracted from the image data itself (not using separately acquired training data). The tracked blocks are then grouped into clusters which contain structurally-similar and temporally-related content. The clusters undergo SVD, image estimates are re-computed, and the algorithm iterates as shown. Because the clusters contain motion-tracked blocks, we expect them to exhibit decreased dynamic complexity and, correspondingly, increased matrix low-rank sparsity (50).

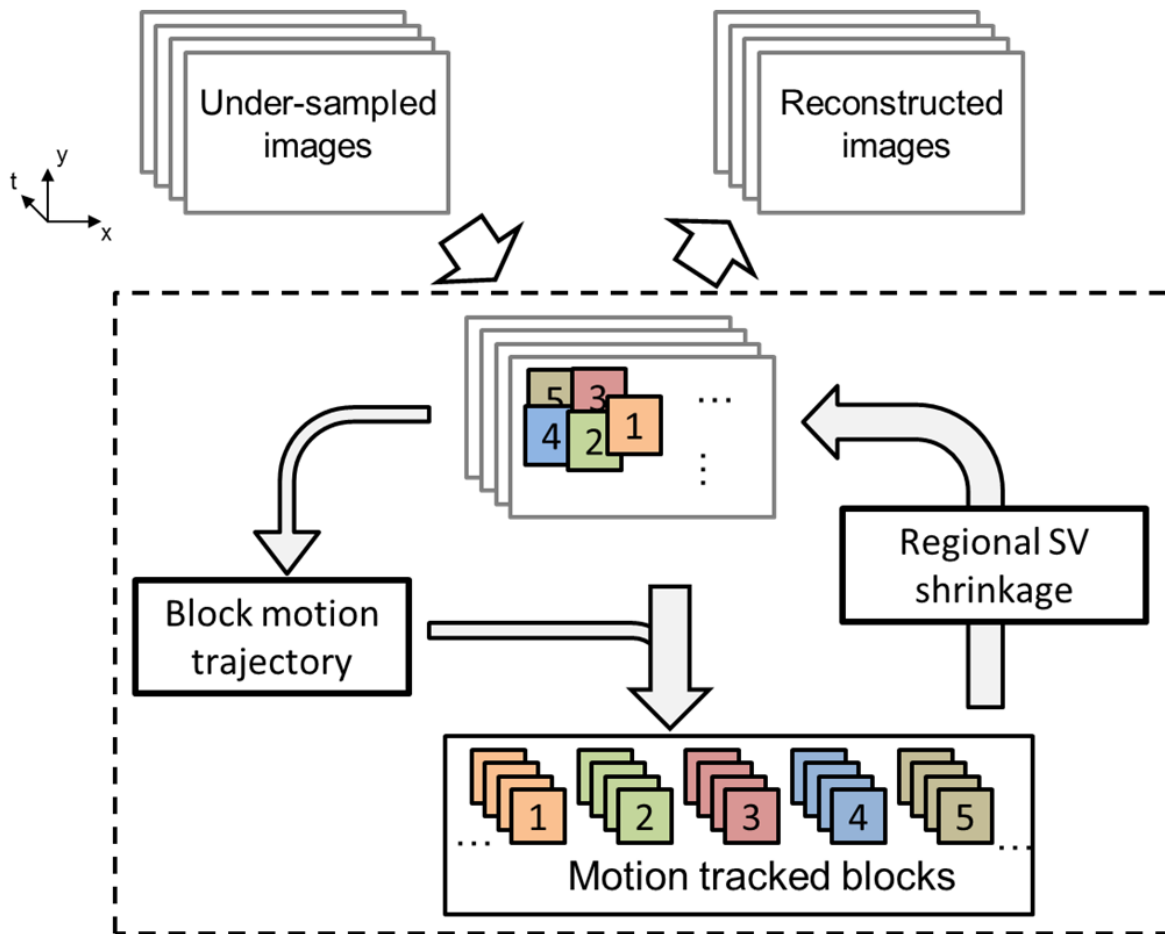


Figure 2.1 General description of Block Low-rank Sparsity with Motion-guidance (BLOSM). A set of undersampled dynamic images are divided into blocks (labeled 1 to 5 as an example). Motion trajectories for each block are obtained from the current image estimation and used to track each block through time. The motion-tracked blocks are stacked together to form a cluster for each group of blocks. Each cluster then undergoes a singular value shrinkage step and the resulting blocks are merged into a new estimated image. The iterations continue for a fixed number of iterations or until a stopping criteria is met.

Specifically, referring to Figure 2.2, a block (red box) is initiated on the first image and is tracked to the succeeding images. Next, as also illustrated, the tracked blocks are gathered into a 3D cluster and rearranged into a 2D matrix, where each block becomes one column and blocks corresponding to separate time points are placed into separate columns. The 2D matrix is then

subject to SVD to exploit low-rank sparsity. The 2D matrix is expected to have greater spatiotemporal sparsity compared to the whole image or to untracked blocks because the blocks have a smaller scope with decreased spatiotemporal variations, and motion tracking leads to less motion contamination.

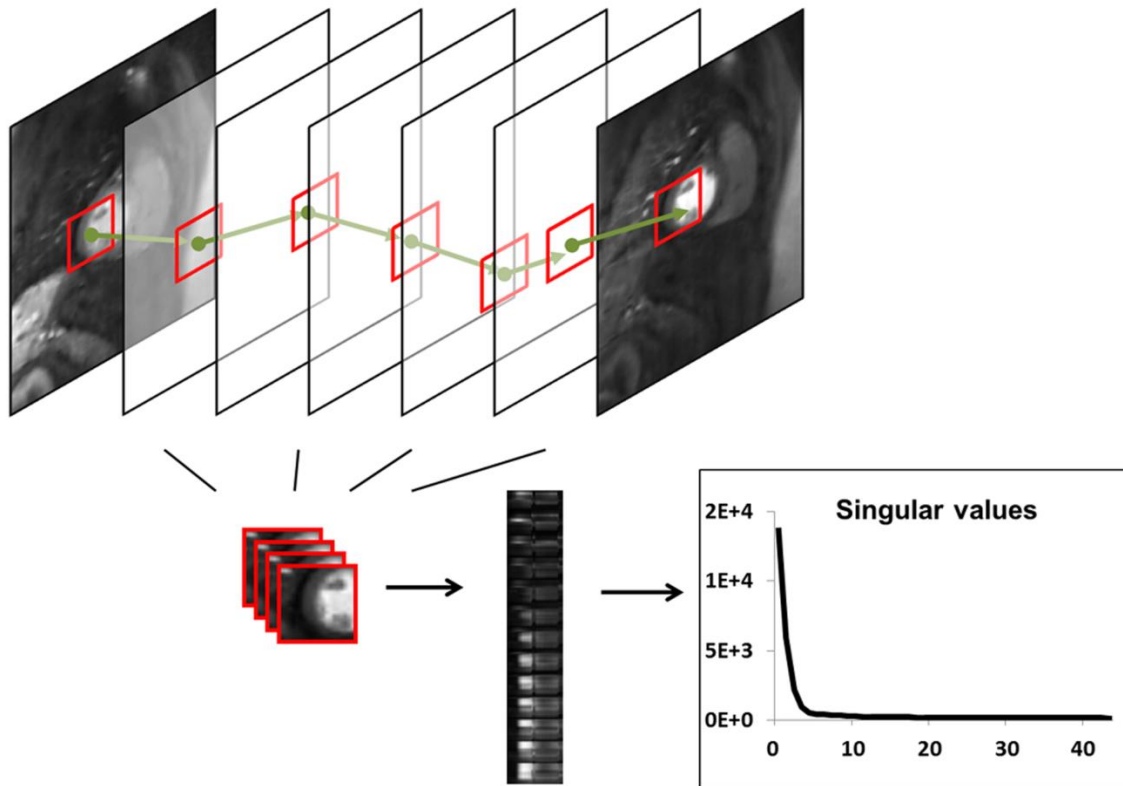


Figure 2.2 BLOSM tracks blocks of pixels through time and exploits regional low-rank sparsity. An example block of pixels (red square) is tracked through all the frames. These temporally related blocks with similar spatial contents are gathered together to form a 3D ($N_b \times N_b \times N_t$) cluster. The cluster is rearranged into a 2D matrix ($N_s \times N_t$, $N_s = N_b \times N_b$), which has high spatiotemporal correlations. Singular value decomposition is applied to the matrix, and only a few of the singular values have significantly higher values than the others, thus the data present low-rank sparsity.

The CS reconstruction problem of BLOSM can be framed as the following constrained optimization problem:

$$\text{minimize}_{\mathbf{m}, \mathcal{R}} \|\Phi_{\mathcal{R}} \mathbf{m}\|_{p^*} \quad [2.1]$$

$$s. t. \|\mathcal{F}_u \mathbf{m} - \mathbf{d}\|_2 < \epsilon$$

where \mathbf{m} represents the estimated dynamic images, \mathbf{d} is the acquired undersampled k-space data, and \mathcal{F}_u is the undersampled Fourier transform which only takes values at the k-space positions where the \mathbf{d} are acquired. $\Phi_{\mathcal{R}}$ represents the operator for block tracking and creation of rearranged clusters, after \mathbf{m} is divided into blocks which are tracked using displacement maps \mathcal{R} . $\|\cdot\|_{p^*}$ is a joint Schatten p -norm that exploits the regional low rank property.

2.2.2 Block motion tracking

There are several techniques that may be used to extract motion information from images (51-55), where displacements of moving objects relative to a reference image can be obtained. In this study, displacement maps were computed using the Advanced Normalization Tools (ANTs) registration toolbox (56,57) which includes a set of state-of-the-art image registration methods. The inputs to ANTS are the complex images. From these inputs, the registration toolbox takes the magnitude of the complex images and outputs pixel-by-pixel displacement maps. For block tracking, the displacement $\Delta \mathbf{u}$ of each pixel was obtained as $\Delta \mathbf{u} = \mathcal{R}(\mathbf{u}) \equiv (\Delta x, \Delta y, \Delta t)$ where $\mathbf{u} = (x, y, t)$ is the pixel space-time position and the displacement operator \mathcal{R} is obtained using ANTS.

In BLOSM, blocks were initiated on the first image and motion tracking was applied to each block. For example, consider one block $\mathbf{B}(\mathbf{u}_1) \in \mathbb{C}^{N_b \times N_b}$, where $\mathbf{u}_1 = (x_1, y_1, t_1)$ indicates that the block center was at position (x_1, y_1) at time frame t_1 . The displacement $\Delta \mathbf{u}_1$ of the block center pixel was obtained from the displacement map as $\mathcal{R}(\mathbf{u}_1)$ and the tracked pixel location

would then be $\mathbf{u}_1 + \mathcal{R}(\mathbf{u}_1)$. Note that the displacement operator \mathcal{R} is calculated globally using the whole image and that $\mathcal{R}(\mathbf{u}_1)$ and $\mathbf{u}_1 + \mathcal{R}(\mathbf{u}_1)$ may be non-integer numbers. Instead of performing a spatial interpolation to get the tracked pixel location as in conventional image registration, the tracked center from \mathbf{u}_1 was taken as $\mathbf{u}_2 = \{\mathbf{u}_1 + \mathcal{R}(\mathbf{u}_1)\}$, where “{ }” takes the integer. A new block $\mathbf{B}(\mathbf{u}_2)$ was defined to include all neighboring pixels around \mathbf{u}_2 with the same block size, as illustrated in Figure 2.3 $\mathbf{B}(\mathbf{u}_2)$ was then motion tracked to succeeding frames with the block center at $\mathbf{u}_n = \{\mathbf{u}_{n-1} + \mathcal{R}(\mathbf{u}_{n-1})\}$ on the n^{th} frame. The tracked blocks were collected as a cluster $\mathcal{E} = [\mathbf{B}(\mathbf{u}_1), \mathbf{B}(\mathbf{u}_2), \dots, \mathbf{B}(\mathbf{u}_{N_t})]$ with dimension of $N_b \times N_b \times N_t$. $\Phi_{\mathcal{R}} \mathbf{m}$ yields a set of clusters $\mathcal{E} = [\mathcal{E}_1, \mathcal{E}_2, \dots]$ and was obtained by performing the block motion tracking procedure for each block defined on the first frame and tracked through all subsequent frames. This approach avoids spatial interpolation, which often leads to image blurring (58).

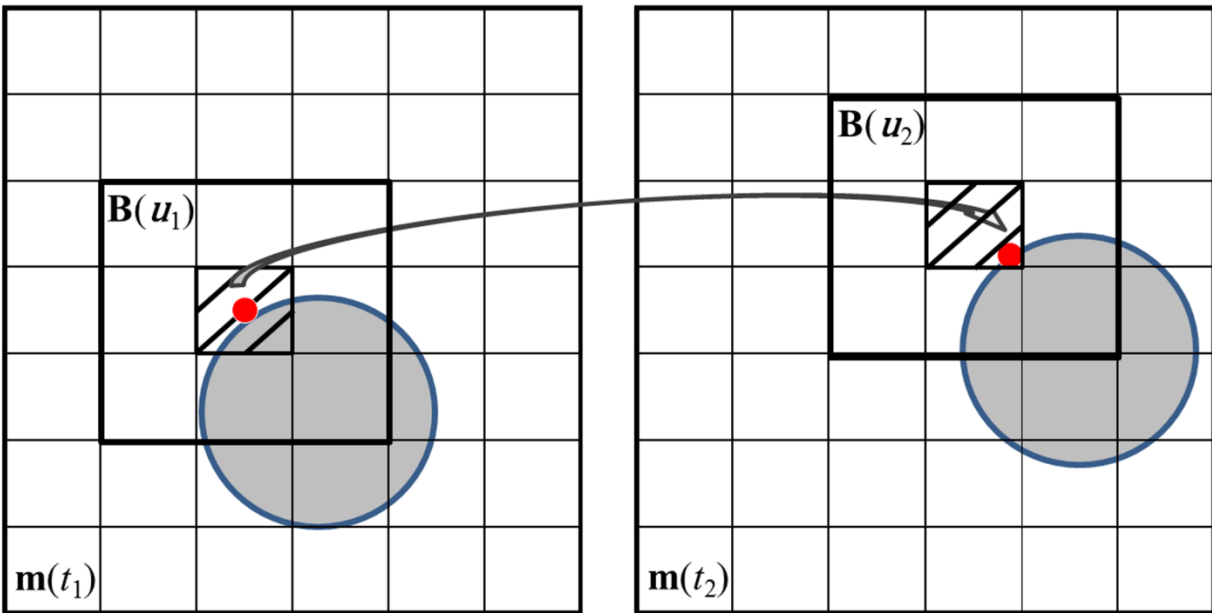


Figure 2.3 Illustration of BLOSM block tracking. $m(t_1)$ and $m(t_2)$ are two consecutive images. An object (gray circle) is displayed on both images which underwent a translational shift (rightward and upward) from frame to frame. A red point is labeled on the circle to represent part of the object. A block $B(u_1)$ centered at the red point is initiated on $m(t_1)$. The red point is tracked from $m(t_1)$ to $m(t_2)$ using the ANTS toolbox, as shown by the arrow. Note that the tracked point on $m(t_2)$ is not at the center of the pixel. Instead of using spatial interpolation, the pixel containing the red dot (the shaded pixel) is selected as the new center pixel for the block. Then the neighboring pixels are included to form a tracked block on $m(t_2)$ as $B(u_2)$ where $u_2 = \{u_1 + \Delta u_1\}$.

2.2.3 Regional sparsity

Matrix rank sparsity has been used previously for dynamic CS reconstruction (19,59-61), with one example being the k-t SLR method. In these studies matrix rank sparsity was applied to the entire image dataset. In addition, recent studies such as Low-dimensional-structure Self-learning and thresholding (LOST) (24,62) and compartment-based k-t Principal Component Analysis (25) showed that separating an image dataset into different regions could increase

spatiotemporal sparsity and improve reconstruction quality. Along these lines, we explored the use of matrix rank sparsity applied regionally by using SVD on tracked regions of dynamic datasets. Specifically, SVD was applied separately on each cluster $\mathcal{E} \in \mathbb{C}^{N_b \times N_b \times N_t}$. Each \mathcal{E} was rearranged into a matrix $\mathbf{Z} \in \mathbb{C}^{N_s \times N_t}$ ($N_s = N_b \times N_b$) where each block becomes one column. Then, \mathbf{Z} was decomposed as $\mathbf{Z} = \mathbf{U}\mathbf{\Sigma}\mathbf{V}^*$ by SVD. The diagonal of $\mathbf{\Sigma} \in \mathbb{C}^{N_s \times N_t}$ consists of singular values γ which, if the block is truly low rank, will have fewer significant values than the rank of \mathbf{Z} .

2.2.4 Coarse-to-fine strategy

We used a variable-density sampling pattern with full sampling of the central phase-encode lines and random undersampling of the outer phase-encode lines. The total number of collected k_y lines was the fully sampled number divided by the acceleration rate, and 50% of the total acquired lines were sampled around the center of k-space. Using this approach, the initial image estimate has very low spatial resolution, and, as the algorithm iterates, the spatial resolution increases. We developed a coarse-to-fine strategy to take advantage of this behavior, where smaller blocks and finer motion tracking (i.e., registration methods) were used as the algorithm iterated and image resolution improved. Specifically, an initial reconstruction was performed where no motion estimation was used for the first 50 iterations. Through the subsequent iterations, smaller block sizes and a finer registration method were used for motion estimation. Given the dimensions of the images as $N_x \times N_y \times N_t$, the initial block size was set as 1/5 of the shorter spatial dimension. After 50 iterations, a mutual-information-based rigid registration method embedded within ANTS was performed to obtain global translational shifts. After subsequent sets of 50 iterations, the block size was decreased 1.5 times until the final block

size reached 5×5 pixels. Motion information was updated every 50 iterations. After 150 iterations, the rigid registration was replaced with a cross-correlation-based non-rigid registration method using ANTS.

2.2.5 Avoidance of gaps

To ensure that gaps are not left between tracked blocks, we used highly overlapping blocks and a gap detection and filling method. After defining the initial blocks, a second set of blocks, shifted by half the block size, was also defined and used (Figure 2.4). In addition, during execution of BLOSM, images are automatically inspected for gaps and additional blocks are generated to cover gaps if they appear. Specifically, on the n^{th} frame after block motion tracking, a mask of uncovered areas or “gaps” is calculated as \mathbf{G}_n . A “common” gap mask \mathbf{G}_c is generated by taking the union set (along the temporal direction) of all the gap masks: $\mathbf{G}_c = \mathbf{G}_1 \cup \mathbf{G}_2 \cup \dots \mathbf{G}_{N_t}$. \mathbf{G}_c is then used for each frame to get the pixels belonging to the gaps. Spatially discontinuous gaps are separated using connected component analysis (63) and are treated as different gap blocks at different spatial locations. Gap blocks at the same spatial location on different frames are gathered together into a 3D block cluster, which is further transformed into a 2D matrix and subjected to SVD, in the same manner as the other block clusters. No motion tracking is performed for the gap blocks in order to avoid potential additional gaps that might occur if the gap blocks were tracked.

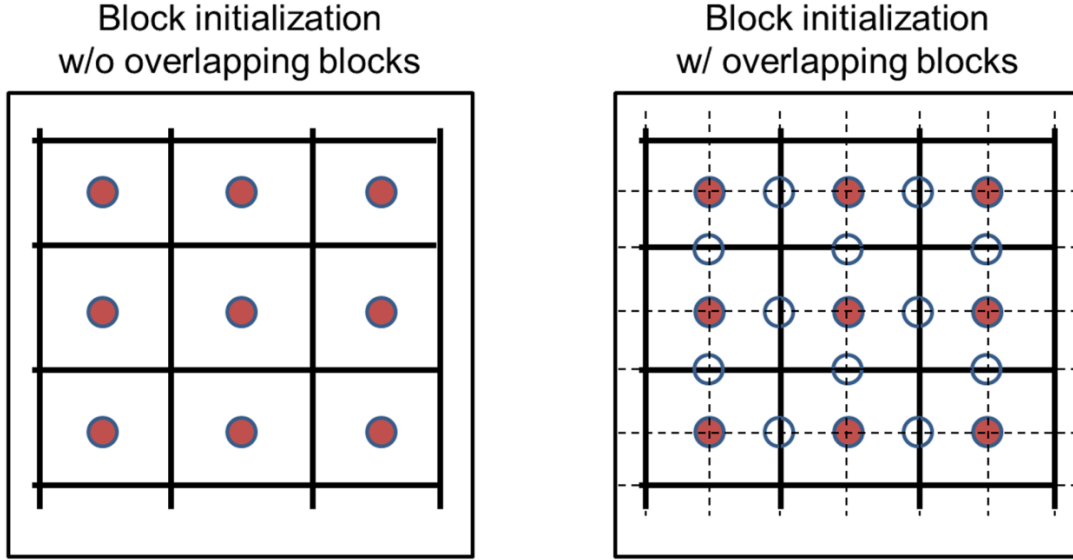


Figure 2.4 In BLOSM, overlapping blocks are used to avoid gaps. The circles in the figure represent block centers. The solid red centers represent initial blocks that cover the whole image, and the unfilled circles represent additional blocks. The initial blocks are demarcated by solid lines, and the additional blocks, which overlap the initial blocks, are demarcated by dashed lines.

2.2.6 Optimization method

A solution to the constrained optimization problem of Equation 2.1 can be obtained by solving the following unconstrained Lagrangian problem using a diminishing λ through the iterations (64)

$$\mathbf{m}^* = \arg \min_{\mathbf{m}, \mathcal{R}} \|\mathcal{F}_u \mathbf{m} - \mathbf{d}\|_2 + \lambda \|\Phi_{\mathcal{R}} \mathbf{m}\|_{p^*} \quad [2.2]$$

An iterative soft-thresholding (IST) algorithm (65) was adopted to solve Equation 2.2.

Specifically, for the i_{th} iteration, the following steps were taken:

1. $\mathbf{m}^i = \mathcal{S}_w(\mathcal{D}_{\lambda, p}(\Phi_{\mathcal{R}} \mathbf{m}^i))$ [2.3]

$$2. \quad \mathbf{m}^i = \mathbf{m}^{i-1} + \delta \mathcal{F}^{-1}(\mathbf{d} - \mathcal{F} \mathbf{m}^i) \quad [2.4]$$

where $\mathcal{D}_{\lambda,p}$ is a singular value soft thresholding operator defined as

$$\mathcal{D}_{\lambda,p}(\mathbf{Z}) = \mathcal{D}_{\lambda,p}(\mathbf{U}\Sigma\mathbf{V}^*) = \mathbf{U} \text{soft}(\text{diag}(\Sigma), \lambda p / \text{diag}(\Sigma)^{p-1}) \mathbf{V}^* \quad [2.5]$$

and $\text{soft}()$ is the well-known soft thresholding operation defined as

$$\text{soft}(\gamma, \lambda p / \gamma^{p-1}) = \text{signum}(\gamma) \max(0, \gamma - \lambda p / \gamma^{p-1}) \quad [2.6]$$

$\mathcal{D}_{\lambda,p}$ was applied to every cluster generated by $\Phi \mathbf{x} \mathbf{m}^i$. \mathcal{S}_w is a weighted averaging operator (66) which merges the blocks to form images. The weighting was calculated as the reciprocal of the number of times one pixel was overlapped by different blocks. \mathbf{m}' is an auxiliary variable and δ is a fixed value step size. Currently, the calculation was set to have a fixed number of iterations.

2.2.7 Evaluation of BLOSM

To evaluate the BLOSM method, we used computer simulations and experimental first-pass contrast-enhanced cardiac MRI of human subjects. In both settings, retrospectively rate-4 undersampled images reconstructed using BLOSM were compared to fully-sampled data and to other CS methods. Since BLOSM uses SVD applied to motion-tracked regions, we compared it to conventional k-t SLR (which uses SVD applied to non-motion-compensated whole images), BLOSM without block motion-guidance (BLOSM w/o MG), and k-t SLR with global motion-guidance (k-t SLR w/ gMG). The implementation of BLOSM w/o MG was straightforward. The blocks were treated as static and motion information was not estimated. Overlapping blocks were

still generated. SVD was applied to each cluster of blocks. The implementation of k-t SLR was treated as BLOSM without motion guidance or blocks. k-t SLR w/ gMG exploited sparsity of the registered/motion compensated whole images. Specifically, for one iteration, the images were first compensated for motion by registering them to one reference image, which was the temporal average of the last 10 images. SVD was applied on the registered images. After the singular value shrinkage, the de-noised images were “registered back” for fidelity calculations since the original acquired data contained motion. These algorithms were all solved using IST, and no additional sparsity constraints were used. The weighting factor λ in front of the sparsity term was optimized independently for each of these three methods, as it was for BLOSM. Other parameters such as the norm p and the block size N_b were selected to be the same as those used for BLOSM. BLOSM was also compared to k-t FOCUSS with motion estimation and compensation (k-t FOCUSS with ME/MC), since this is a motion-compensated CS method. The program code of k-t FOCUSS with ME/MC was obtained online (67). The five CS methods: BLOSM, k-t FOCUSS with ME/MC, k-t SLR, BLOSM w/o MG and k-t SLR w/ gMG were systematically compared.

Image quality for the various reconstruction algorithms was quantified using the root mean square error (RMSE) and the structural similarity (SSIM). RMSE measures the direct difference between the two images and is widely used for the assessment of CS methods (15,16,19,23,45,68,69). In this study, we used the relative RMSE (rRMSE) defined as

$$\text{rRMSE} = \frac{1}{N} \sqrt{\sum \frac{|\mathbf{x}-\mathbf{y}|^2}{|\mathbf{x}|^2}} \quad [2.7]$$

where $N = N_x \times N_y \times N_t$, \mathbf{x} are the fully-sampled images and \mathbf{y} are the reconstructed images. We also used the structural similarity index (SSIM), which is a more comprehensive measurement of

the similarity between two images, and includes measurement of structure, intensity and contrast, representing human perception more closely (70). The equation for SSIM is

$$\text{SSIM}(\mathbf{x}, \mathbf{y}) = \frac{(2\mu_x\mu_y + c_1)(2\sigma_{xy} + c_2)}{(\mu_x^2 + \mu_y^2 + c_1)(\sigma_x^2 + \sigma_y^2 + c_2)} \quad [2.8]$$

where \mathbf{x} and \mathbf{y} are the two images undergoing comparison, μ_x and σ_x are the average and variance of \mathbf{x} , σ_{xy} is the covariance of \mathbf{x} and \mathbf{y} , and c_1 and c_2 are variables that stabilize the division with a weak denominator, chosen as described by Wang et al (70).

2.2.8 Computer-simulated phantoms

Computer simulations of heart-like phantoms with complex motions and signal intensity variations were used to evaluate BLOSM (Figure 2.5). Specifically, we simulated objects undergoing rigid translational shifts along the phase-encoding and readout directions, objects undergoing both abrupt and gradual changes in size (which can be interpreted as either through-plane motion or cardiac contraction), objects undergoing appearance and disappearance (i.e., non-permanent features) and an object undergoing counterclockwise rotation. Motions were combined with temporally quadratically changing signal intensity.

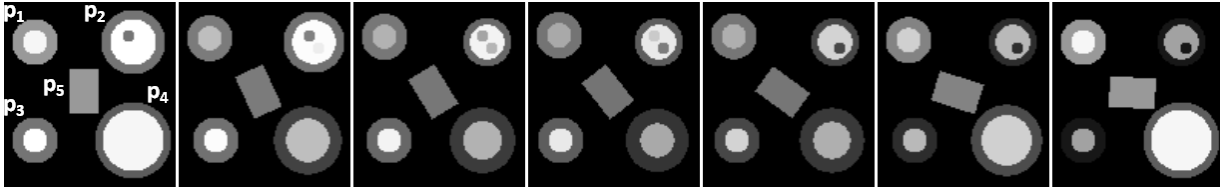


Figure 2.5 Simulated phantoms in a time series. Images at selected time points are shown. Phantom 1 (P1) undergoes rigid translational shifts along the phase-encoding direction. P2 has an abrupt change in size as well as appearance/disappearance of features to mimic through plane motion combined with translational shifts in the readout direction. P3 undergoes rigid translational shifts along the readout direction. P4 undergoes a gradual change in size which can be interpreted as either cardiac contraction or through-plane motion. P5 rotates counterclockwise through time to mimic object rotation motion. All the phantoms also have quadratically changing signal intensity over time.

The images were Fourier transformed to generate k-space data, undersampled at acceleration rate 4 using the variable density k_y -t mask described above, and then reconstructed using various CS algorithms.

2.2.9 First-pass cardiac perfusion imaging

All imaging was performed on a 1.5T MR scanner (Avanto, Siemens, Erlangen, Germany). Eight different subjects with suspected heart disease were studied in accordance with protocols approved by our institutional review board after informed consent was obtained. For each subject a 5-channel phased-array RF coil was used and 1-4 short-axis slices were acquired each heartbeat for 50 repetitions during infusion of 0.075 mmol/kg gadopentetate dimeglumine (Magnevist, Bayer HealthCare, Montvale, NJ). A saturation-recovery Turbo FLASH sequence was used with parameters as follows: nonselective 90° saturation pulse with a saturation recovery time of 100-120 ms, field of view = 240-315 \times 370-410 mm², matrix = 86-152 \times 128-200, slice thickness = 8 mm, flip angle = 8-15 $^\circ$, TR = 1.9-2.2 ms, and TE = 0.9-1.4 ms.

Immediately prior to initiating the perfusion scan, each subject was instructed to suspend respiration during the scan using our standard instructions for breathholding. If the subjects could not hold their breath for the entire scan, they were instructed to breathe lightly for the remainder of the scan. As is typical for first-pass perfusion MRI of the heart, even with proper instructions about breathing, many patients do not comply well with the instructions, and various breathing patterns occur during perfusion imaging. The datasets collected and used in this study all present prominent respiratory motion, even though the patients were instructed not to breathe. From the 8 patients studied, a total of 26 slices were collected, and each slice was treated as a distinct dataset. All data were acquired without prospective undersampling. Among the 26 datasets, 14 of them were fully-sampled sum-of-squares (SoS) combined magnitude-valued images and 12 of them were fully-sampled multi-coil complex-valued k-space data. In this study, we focused our efforts on evaluating BLOSM and other CS methods using only single-coil data. To serve this purpose, we combined the 12 multi-coil complex-valued k-space datasets into 12 single-coil magnitude-valued image data using SoS. The resulting 26 magnitude-valued datasets were transformed into k-space and retrospectively undersampled at acceleration rate 4 using the variable density k_y -t mask described above, and then reconstructed using various CS algorithms.

2.2.10 Evaluation of initial block size, initial block positions, the coarse-to-fine strategy, and the use of motion compensation

Systematic experiments were performed to determine whether the initial block size or block positions have an effect on image quality. For these studies, the same datasets were

reconstructed using different initial block sizes or positions. Specifically block size factors of 2, 3, 4, ..., 10 were chosen, which correspond to initial block sizes of 51, 35, 27, ..., 11 for an image matrix of 102×128 . Due to the usage of the coarse-to-fine (CTF) strategy, where the block size decreases through the iterations and the registration method varied with iteration, the final block size was kept constant (5 for all settings), and the total iteration number was the same for different initial settings. Relative RMSE was calculated to perform a quantitative evaluation comparing the initial block sizes. Reconstruction time was also recorded. To assess whether there is a dependence on the initial block positions, BLOSM reconstructions using the original initial block positions and using shifted initial block positions (shifted by up to one quarter of the initial block size) were compared to reference images, where the reference images were fully-sampled 2DFT-reconstructed images. Experiments were also performed to demonstrate the utility of the CTF strategy. For these studies, both simulated and human datasets were reconstructed using BLOSM with and without the CTF strategy. In BLOSM without the CTF strategy, a constant block size and rigid registration method were used through all the iterations. Studies were also performed to show that motion guidance within BLOSM improves image quality. Both simulated and human datasets were used for these studies, which compared BLOSM with and without motion tracking.

2.2.11 Computation time

Benchmark tests for BLOSM, k-t SLR and k-t FOCUSS with ME/MC were performed. All tests were performed in MATLAB on a desktop computer (3.4GHz Intel(R)i7 CPU with 12GB RAM). A human perfusion dataset with a matrix size of 102×128 and 44 time frames was

used. A fixed number of 200 iterations was used for BLOSM and k-t SLR, and the k-t FOCUSS with ME/MC method used a convergence metric to terminate the algorithm.

2.3 RESULTS

2.3.1 Comparison of BLOSM and other CS reconstruction methods using computer simulations

Figure 2.6 shows the comparison of BLOSM to other reconstruction algorithms for the computer-simulated phantoms. Example rate-4 accelerated CS-reconstructed images at one time point along with the fully-sampled reference and under-sampled FFT reconstructed images are shown on the top row. In Figure 2.6 various motions were presented: rigid translational shifts along the phase-encoding direction (phantom 1, or P1) and readout direction (P3); translational shifts combined with an abrupt change in size and appearance/disappearance of non-permanent features (P2) and gradual change in size (P4), both of which can be interpreted as either through-plane motion or cardiac contraction; and object rotation (P5). Corresponding position-time (x - t) profiles are shown on the bottom row for each of the simulated phantoms. In the presence of object motion, signal intensity variation, and the appearance and disappearance of objects, visual inspection shows that images reconstructed using BLOSM most closely resemble the fully sampled images, as compared to the other CS methods. k-t FOCUSS with ME/MC and conventional k-t SLR had substantial residual artifact as well as some blurring. Some artifacts were more severe on k-t FOCUSS with ME/MC. BLOSM w/o MG removed more artifacts than conventional k-t SLR, which supports the concept of exploiting regional instead of global

spatiotemporal sparsity. However, edge artifacts along the direction of motion can be seen on BLOSM w/o MG, which are attributed to the lack of motion correction. k-t SLR w/ gMG had substantial smoothing effects. Relative RMSE and SSIM analysis showed that BLOSM achieved the minimum error and the maximum similarity ($rRMSE=2.85E-8$, $SSIM=0.89$) compared to k-t FOCUSS with ME/MC ($rRMSE=6.30E-8$, $SSIM=0.66$), k-t SLR ($rRMSE=8.85E-8$, $SSIM=0.49$), BLOSM w/o MG ($rRMSE=6.50E-8$, $SSIM=0.78$) and k-t SLR w/ gMG ($rRMSE=8.28E-8$, $SSIM=0.57$).

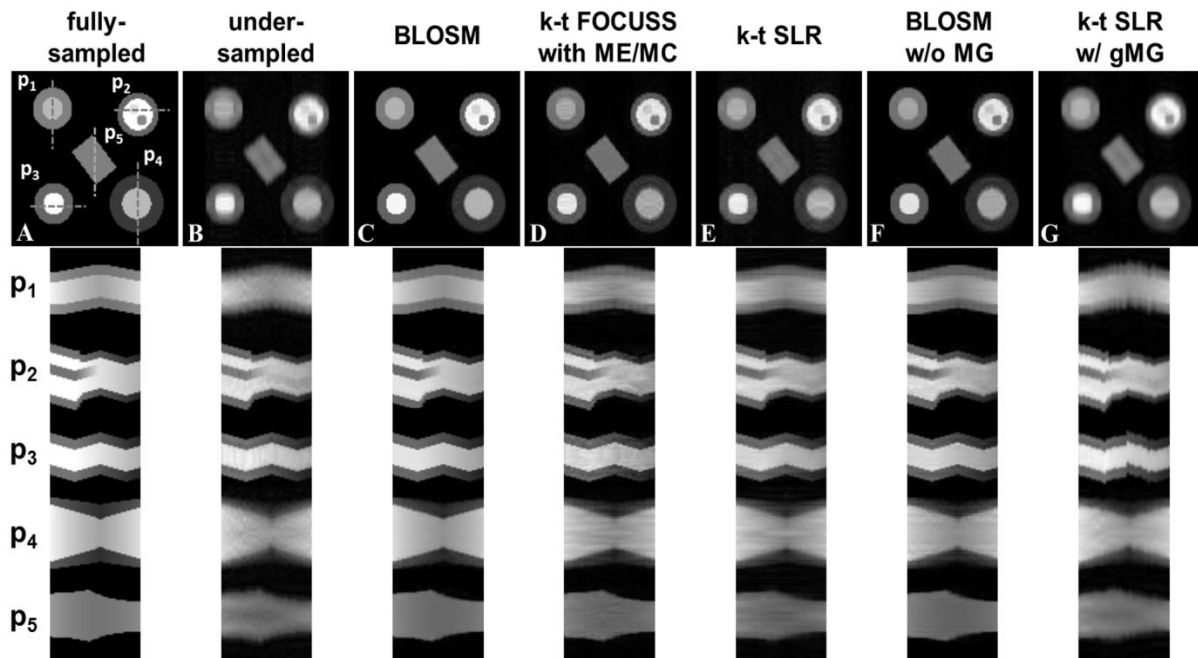


Figure 2.6 Reconstruction of retrospectively rate-4 undersampled images from computer-simulated phantoms that undergo translational shifts, rotation, deformation/TPM and variable signal intensity over time. Example reconstructed images at one time frame are shown in the top row. Corresponding x-t profiles for each phantom (P1-P5) are shown on the bottom panel, where the profile locations are indicated by dashed lines on the fully-sampled image. The first column shows fully-sampled data reconstructed by FFT and serves as a reference. The other columns display undersampled data reconstructed using conventional FFT and the CS methods: BLOSM, k-t FOCUSS with ME/MC, k-t SLR, BLOSM without motion guidance (BLOSM w/o MG) and k-t SLR with global motion guidance (k-t SLR w/ gMG). BLOSM provided the most accurate recovery of the fully sampled images. For k-t FOCUSS with ME/MC, k-t SLR and BLOSM w/o MG, residual artifacts and moderate motion blurring can be observed, especially on P4.

2.3.2 Comparison of BLOSM and other CS reconstruction methods for accelerated first-pass cardiac perfusion imaging of human subjects

Figure 2.7 shows representative results from first-pass contrast-enhanced perfusion images of the heart using different CS reconstruction methods. Images acquired at early, middle, and late phases of contrast enhancement are shown in different rows. Due to patient respiration, the heart shifted downward (~ 16 mm) in the middle row. Images from fully-sampled k-space data as well as rate-4 retrospectively-accelerated images reconstructed using conventional FFT, BLOSM and other CS methods are shown in separate columns. Visual inspection shows that BLOSM-reconstructed images resemble the fully-sampled data at all phases better than the other CS methods. Reconstruction methods without motion guidance, namely k-t SLR and BLOSM w/o MG (columns 3 and 4), show the inability to recover artifact-free images when motion occurs (row 2). k-t FOCUSS with ME/MC (row 2) had blurring and lower SNR as compared to BLOSM. k-t SLR w/ gMG had excessive blurring, similar to that seen in the simulated phantom, which propagated through many phases including phases with little or no motion.

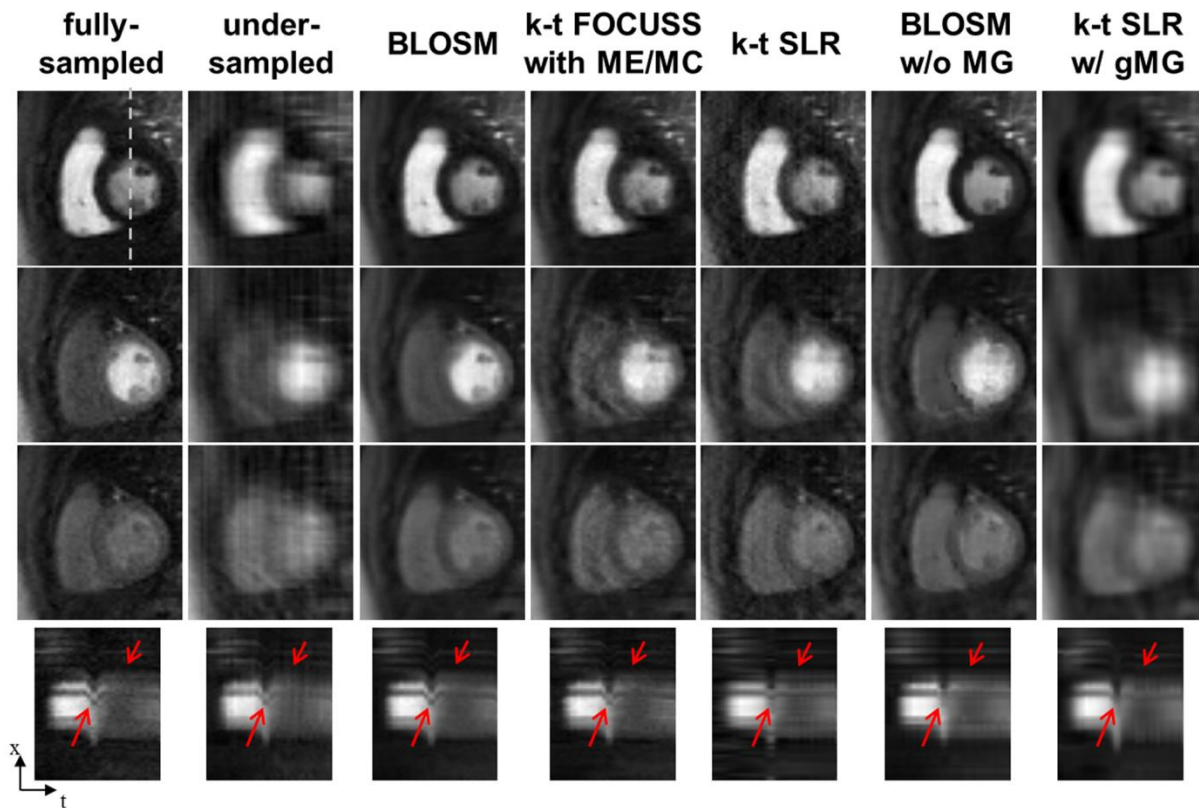


Figure 2.7 Comparison of BLOSM with other CS algorithms using retrospectively rate-4 undersampled first-pass contrast-enhanced MRI of the heart. Example frames are presented in different rows representing early, mid and late phases of contrast passage. Undersampled data are reconstructed by conventional FFT, BLOSM, k-t FOCUSS with ME/MC, k-t SLR, BLOSM without motion guidance (w/o MG) and k-t SLR with global motion guidance (w/ gMG). Respiratory motion occurred to a large degree during the middle phase (second row) and to a lesser degree at the late phase (third row). BLOSM provided the best image quality for all the phases and very closely matched the fully-sampled images. k-t FOCUSS with ME/MC, k-t SLR and BLOSM w/o MG performed fairly well for phases where there was no or little motion. For the mid phase, severe artifacts can be seen for k-t FOCUSS with ME/MC, k-t SLR and BLOSM w/o MG. k-t SLR w/ gMG resulted in blurred images for all phases. x-t profiles showing similar results are shown on the bottom row, with important dynamic features highlighted by red arrows.

Motion recovery can also be appreciated by observation of the x-t profiles. As highlighted by the red arrows, noise and artifacts were mostly removed without over-smoothing using BLOSM, while all the other methods showed various artifacts and did not recover x-t profiles when motion occurred as accurately as BLOSM.

The reconstructed images were analyzed quantitatively using rRMSE and SSIM. Values for 26 slices are shown in Figure 2.8. BLOSM demonstrated the best reconstruction quality with the minimum rRMSE and the maximum value of SSIM ($p < 0.05$ vs. all other methods, ANOVA).

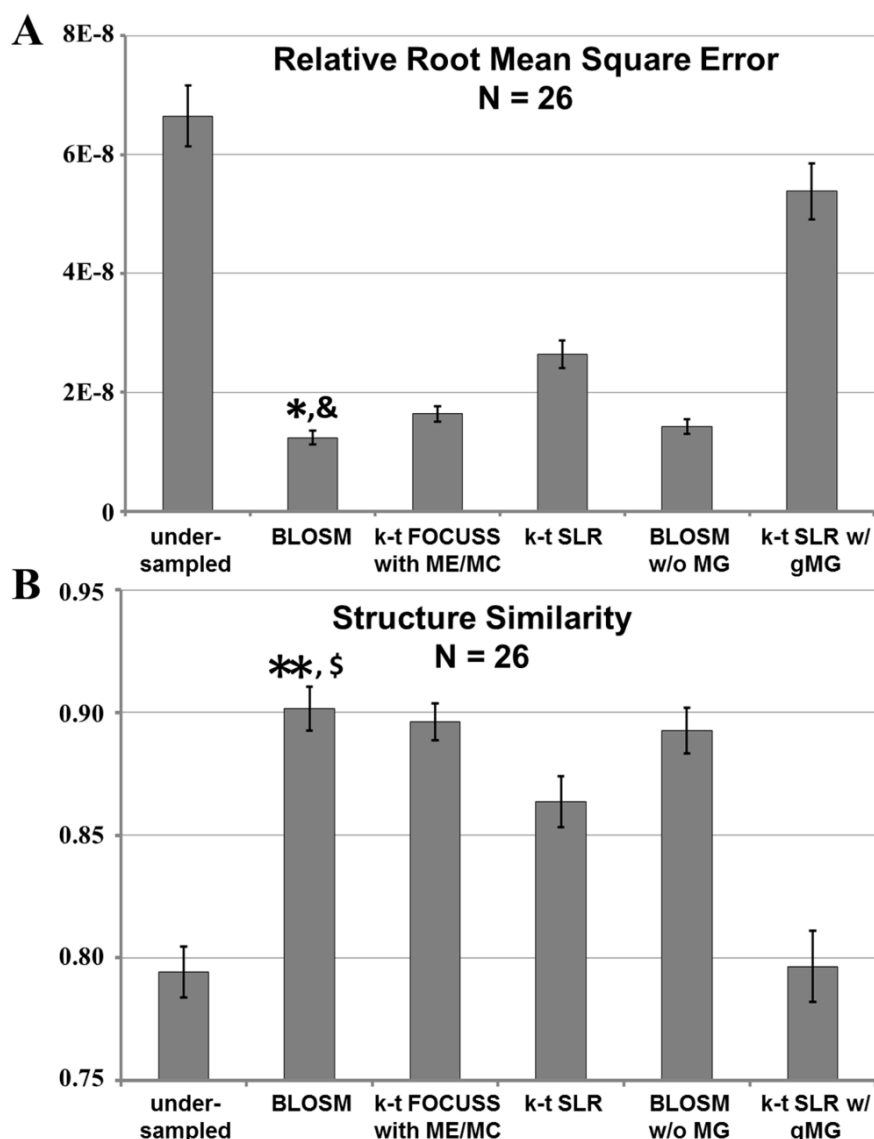


Figure 2.8 Quantitative analysis of the performance of various reconstruction methods applied to rate-4 accelerated first-pass contrast-enhanced MRI of the heart. Average relative root mean square error (rRMSE) and structural similarity (SSIM), averaged over time, of the CS-reconstructed images were compared to fully-sampled reference images. BLOSM achieved the lowest error (rRMSE) and highest similarity (SSIM) of all the CS methods. (* $P < 0.01$ v.s. undersampled, k-t FOCUSS with ME/MC, k-t SLR and k-t SLR w/ gMG; & $P < 0.05$ v.s. BLOSM w/o MG; ** $P < 0.01$ v.s. undersampled, k-t SLR, and k-t SLR w/ gMG; \$ $P < 0.05$ v.s. k-t FOCUSS with ME/MC).

2.3.3 Evaluation of initial block size, initial block positions, the coarse-to-fine strategy, and the use of motion compensation

Figure 2.9 plots rRMSE as a function of the BLOSM iteration number for different initial block sizes, and shows that BLOSM converges to a single rRMSE value independent of the initial block size. Thus, no single initial block size is optimal for BLOSM.

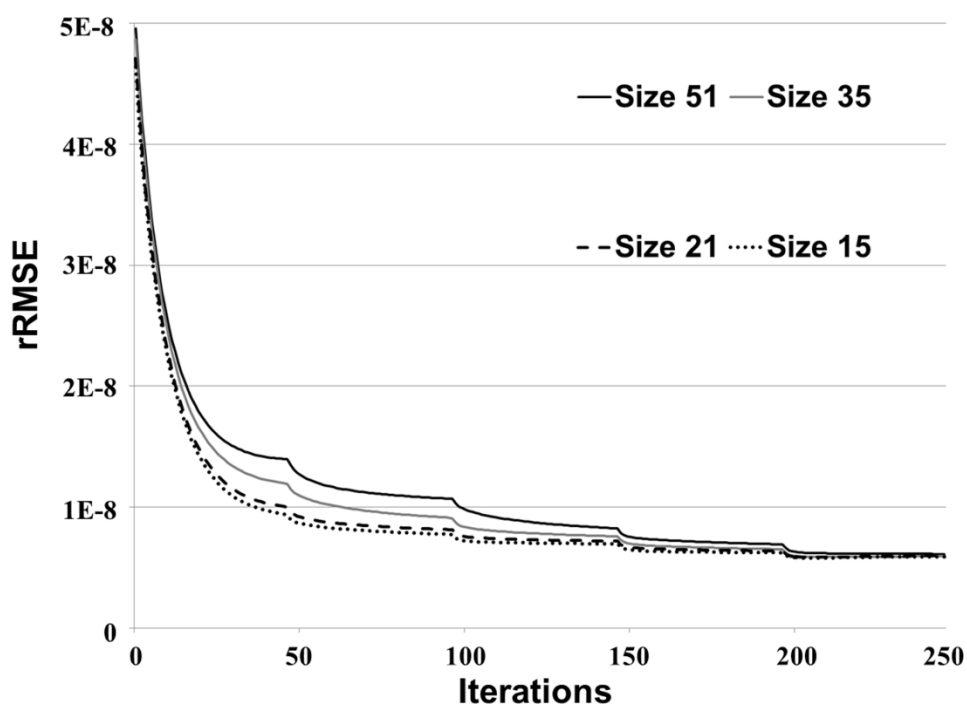


Figure 2.9 Convergence of BLOSM for different initial block sizes. BLOSM using different initial block sizes was used to reconstruct a first-pass perfusion dataset. These rRMSE vs. iteration curves demonstrate that the convergence of BLOSM is essentially independent of the initial block size (not all tested initial block sizes are shown, but all had similar behavior).

Using similar plots, Figure 2.10A-B demonstrate the benefits of the coarse-to-fine strategy, as use of the coarse-to-fine strategy reduces rRMSE in both phantom and human data. Lastly, Figure 2.10C-D show the benefits of motion guidance, as BLOSM with motion tracking leads to reduced rRMSE as compared to BLOSM w/o MG. A number of abrupt transitions in rRMSE as a function of iteration are observed in Figure 2.9, and correspond to coarse-to-fine adjustments of block size, registration method, and iterative soft thresholding values as BLOSM iterates.

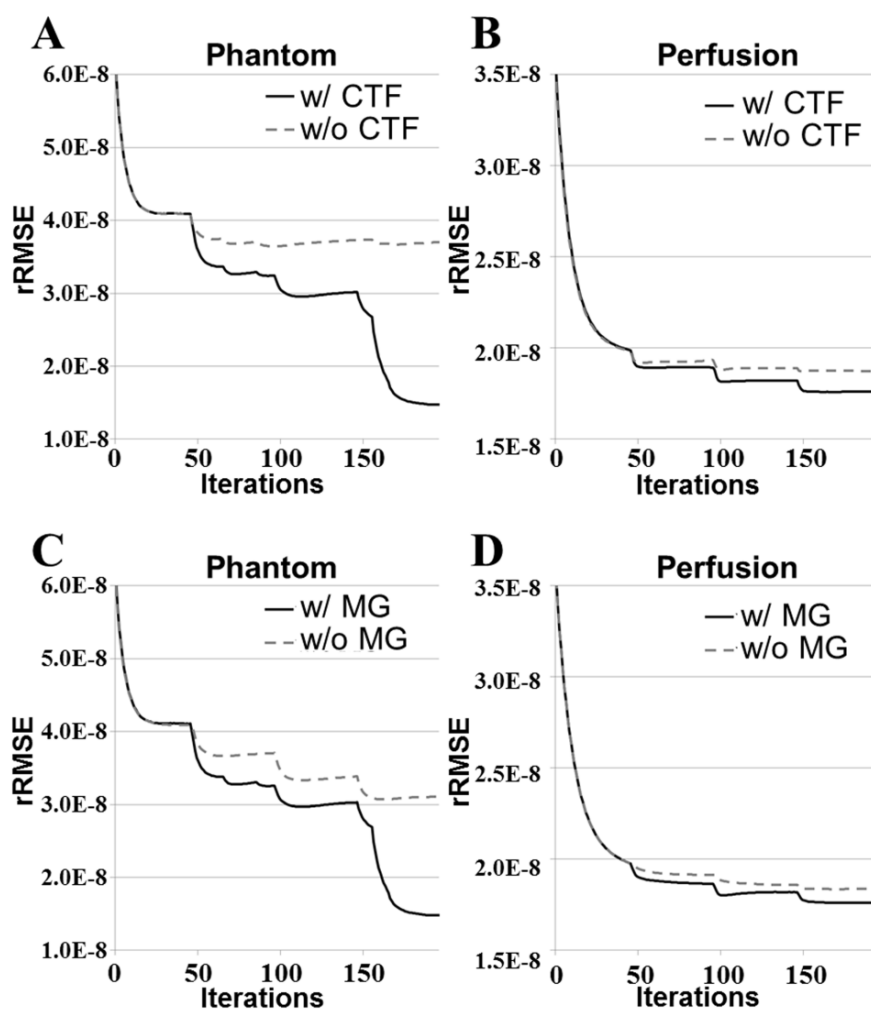


Figure 2.10 Convergence of BLOSM under various conditions. Panels (A and B) show for both computer simulated phantoms and in vivo perfusion imaging that the coarse-to-fine strategy provides lower rRMSE compared to not using this strategy. Similarly, panels (C and D) show that for both computer simulated phantoms and in vivo perfusion imaging the use of motion guidance reduces rRMSE compared to not using motion guidance.

To quantify potential differences related to initial block positions, BLOSM using the original block positions and BLOSM using the shifted block positions were both compared to a reference image (a fully-sampled 2DFT-reconstructed image). As shown in Figure 2.11, we found a nearly identical difference distribution compared to the reference image for BLOSM using the original block positions and BLOSM using the shifted block positions.

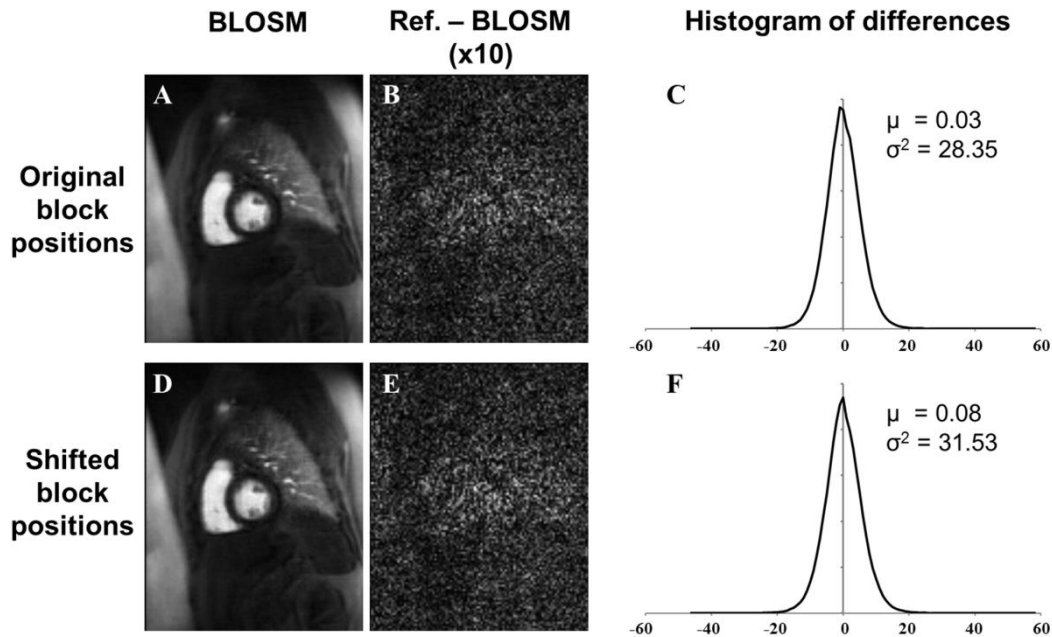


Figure 2.11 Image reconstruction using BLOSM is not highly dependent on the initial block positions. Images were reconstructed using BLOSM with original initial block positions (A) and with shifted initial block positions (D). The difference between a fully-sampled 2DFT-reconstructed image (Reference image) and (A) is shown in (B), and the difference between the reference image and (D) is shown in (E). Histograms from multiphase difference images using the original initial block positions and the shifted initial block positions are shown in (C) and (F), respectively. Using either the original initial block positions or the shifted initial block positions results in the same difference distribution (Gaussian distribution verified using the Jarque-Beta test) compared to the reference images. μ is the mean and σ^2 is the variance.

2.3.4 Computation time

Benchmark tests showed the total computation times for BLOSM, k-t SLR and k-t FOCUSS with ME/MC for a given dataset were 986, 32, and 142 seconds, respectively. For BLOSM, 647 seconds were spent on motion estimation, 93 seconds on computing sparsifying transforms (SVD) and 210 seconds on block handling. Due to the coarse-to-fine strategy, BLOSM iterations were divided into 4 stages, where stage 1 had 60 blocks of size 21×21 pixels,

stage 2 had 90 blocks of size 17×17 , stage 3 had 154 blocks of size 13×13 and stage 4 had 216 blocks of size 11×11 . The average computation times per iteration were 1.1 ± 0.04 , 1.5 ± 0.04 , 1.9 ± 0.05 and 2.3 ± 0.05 seconds for each stage, respectively.

2.4 DISCUSSION

We developed a novel CS reconstruction technique, termed BLOSM, that exploits regional spatiotemporal sparsity and compensates for the effects of respiratory motion by embedding motion tracking within the reconstruction algorithm. Experiments comparing different reconstruction algorithms demonstrated that the regional approach with motion compensation combine to contribute to the superior performance of BLOSM. Visual inspection of images as well as quantitative assessments of image quality (rRMSE and SSIM) demonstrated the advantages of BLOSM.

The two key components of BLOSM, namely the use of both regional sparsity and motion tracking, work together to achieve improved image quality. The finding that BLOSM without motion guidance performed better than global k-t SLR demonstrated that regional sparsity has advantages over global sparsity when using SVD. This finding was also observed in previous work where compartment-based k-t PCA separated perfusion images into different parts (right ventricular blood pool, left ventricle, etc.) and achieved better image quality than conventional k-t PCA (25). In addition, BLOSM with motion guidance performed better than BLOSM without motion guidance, showing the advantage of the motion-guided regional approach.

Adequate motion tracking is central to the performance of BLOSM. We chose to use the ANTS toolbox because it can handle various types of motion and deformation, even with changing signal intensity (56,57). It is worth pointing out that although in BLOSM blocks are tracked, the motion information used for block tracking is obtained by registering whole images, not by using a block matching algorithm, such as in k-t FOCUSS with ME/MC. We used the displacement of the central pixel of the block to represent the whole block motion. The displacements in a region are expected to be smoothly changing, so the center pixel should be representative of the block. To demonstrate this, we also implemented a version of BLOSM which used the average motion of all the pixels within a block to represent the block motion (BLOSM w/ avg. motion), and compared it to BLOSM using the central pixel. We reconstructed 30 datasets which included 26 human perfusion data and 4 simulated data. Results (Figure 2.12) showed that the behaviors from the two methods were quite similar, where BLOSM using the central pixel had better image quality for some datasets.

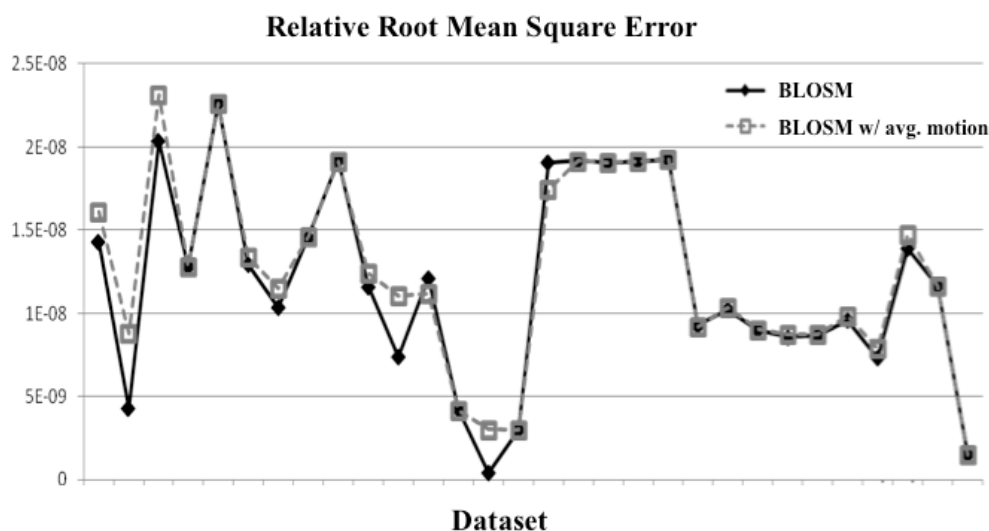


Figure 2.12 Relative root mean square (rRMSE) values from 30 dataset (26 human perfusion and 4 computer simulation) using BLOSM and BLOSM with average motion (BLOSM w/ avg. motion). Similar rRMSE were found among the two implementations while for some dataset BLOSM which uses the central pixel to represent the block motion had better rRMSE behavior.

Our method for tracking blocks in BLOSM avoided the use of spatial interpolation. In contrast, our implementation of k-t SLR with global motion guidance included spatial interpolation steps in the sparsity calculation and in the fidelity calculation, and lead to blurring and smoothing. BLOSM was designed to avoid spatial interpolation, which contributed to its lack of blurring. BLOSM was evaluated using 2D imaging, and may be subject to errors when through-plane motion occurs. Therefore, we used computer simulations to investigate the behavior of BLOSM with through-plane motion and found that, while some minor blurring can occur, BLOSM still performed better than the other CS methods under these conditions. This result held even when objects completely disappeared and appeared over time. In the future we may investigate a frame rejection scheme and/or a 3D acquisition to better deal with through-plane motion. While motion tracking within BLOSM will never be perfect, we combined motion tracking with SVD, which is known to be fairly tolerant to misregistration of serial images

(17,19,71). Also, the use of a block-tracking approach could potentially lead to image regions that are not covered by tracked blocks, i.e., gaps. To avoid such a situation, we use highly overlapping blocks and, if gaps do occur, they are detected and patched with additional blocks. Our results also showed that BLOSM converges to a common RMSE independent of the initial block size, and that there is little effect of using different initial block positions on the resulting reconstructed images.

In order to reduce blurring due to interpolation, we restrict our motion tracking calculations to integer numbers of pixels. However, there could be a possibility that the bias due to taking the integer could accumulate over multiple frames. To check whether there is an accumulation of the bias, we compared the BLOSM tracking method (which takes integer values) to a similar method where tracking is performed without restriction to an integer number of pixels. For the second method (without restriction to an integer number of pixels), the method can be described as $\mathbf{u}_n = \mathbf{u}_{n-1} + \mathcal{R}(\mathbf{u}_{n-1})$, where \mathbf{u}_n is the pixel at position \mathbf{u} on frame n , and the displacement of \mathbf{u} is given by $\Delta\mathbf{u} = \mathcal{R}(\mathbf{u})$. Since in this case \mathbf{u}_n can be non-integer coordinates and $\mathcal{R}(\mathbf{u})$ only provides displacements for \mathbf{u} values located on the Cartesian grid, spatial spline interpolation was performed to compute displacements at non-integer coordinates. Each pixel on the first frame was tracked through time using the two methods, and coordinates of the tracked pixels were recorded. Figure 2.13 shows traces of two example tracked pixels from a human perfusion dataset. While the two methods do not track motion identically, no accumulation of error over time is observed for the BLOSM algorithm. The average accumulations (averaged differences of all tracked positions on the last frame) are -0.18 ± 1.96 pixels in the x direction and 0.11 ± 1.88 pixels in the y direction. Indeed these tracking errors are

smaller than one pixel, which is very small compared to the minimum block size used in BLOSM of 5x5 pixels.

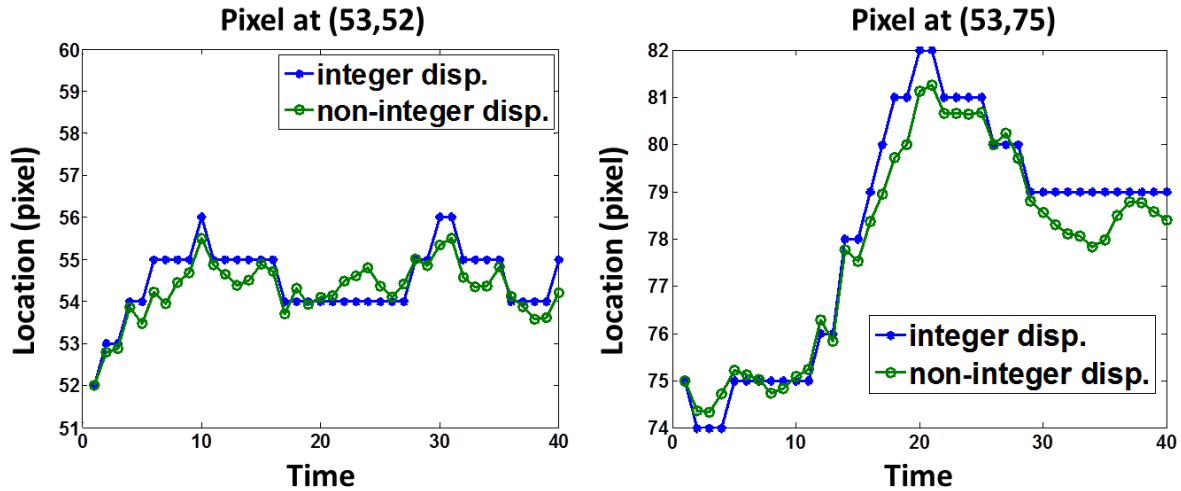


Figure 2.13 Tracking of two example pixels through time using integer-displacement and non-integer-displacement methods. No accumulation of error is observed.

Our data also support the use of the coarse-to-fine strategy for BLOSM. As the BLOSM algorithm iterates, the spatial resolution of the estimated image improves and supports the use of finer motion estimation and use of smaller blocks. When comparing BLOSM with and without the coarse-to-fine strategy, rRMSE is lower when using this strategy. In the current implementation of BLOSM, the block size decreased and the registration method updated once for every fifty iterations, and these settings achieved good results. However, a better approach to consider in the future may be to include an estimate of displacement accuracy into the cost function and to adaptively weight motion-guidance. In that case, when the displacement estimation accuracy is low, less trust will be given to the current estimate and the previous estimate would be used instead. Such a strategy would be similar to the approach used with Kalman filters and may improve tolerance to motion estimation error (72).

Free parameters for the CS problem were empirically varied to find a set that achieved low rRMSE. The Schatten norm, p , threshold value, λ , and block size, N_b , were optimized separately while fixing the other parameters. Parameter optimization was done for phantom and human data, and the optimal values were similar for both types of data, indicating that the algorithm is stable. With Schatten norm $p < 1$, Equation 2.1 becomes a non-convex problem. We found that optimal image quality was achieved with $p=0.9$, and this agrees with other results using the same Schatten norm applied to MR images of the brain (64). The threshold value for each block at singular value γ is calculated as $\lambda p(\gamma)^{p-1}$ and the selection of $p=0.9$ enables a block-specific regularization since different blocks have different values of γ . Singular values which contain most of the energy and contrast will receive low penalties while small singular values which mainly correspond to noise and artifacts will receive higher penalties. When p is fixed, the weighting factor λ in Equation 2.6 controls the threshold and has a high impact on reconstruction quality. For each of the CS methods (BLOSM, BLOSM w/o MG, k-t SLR and k-t SLR w/ gMG) a range of λ (0~2000) was independently tested using a couple of datasets to find the optimal λ that gave the minimum rRMSE. For the IST algorithm and using a diminishing of λ through iterations, we found that the final image quality was stable for a range of λ values (20~200) even with changes in other experimental parameters, such as the norm p . When an aggressive λ value (>500) was chosen, over-regularization was observed as block-like artifacts. To demonstrate this, we have tested the influence of λ on block artifacts by running the BLOSM reconstruction using λ values of 0, 50, 500 and 15000. As shown in Figure 2.14, the block artifacts become visible when λ is 15000. The singular values from a region-of-interest (ROI) block over the left ventricle and a background block with the same size at the top left corner were calculated. Singular values before and after the thresholding were both plotted in Figure 2.14. It is shown that the block

artifacts happen when λ is set too high which leads to tremendous decreases in the first few significant singular values. Other recent methods exploiting regional sparsity (24,25,66) also have different regularization of different regions. A moderate filtering or denoising step is taken in these studies to ease the block artifacts. Our use of overlapping blocks is similar to these strategies. In our study, all images were scaled to have a maximum value of 250 and no block artifacts were observed for a wide range of λ (0~500) with our experimental settings. Most of the datasets tested showed optimal behavior at $\lambda=50$. Thus a λ value of 50 was chosen to reconstruct all the datasets.

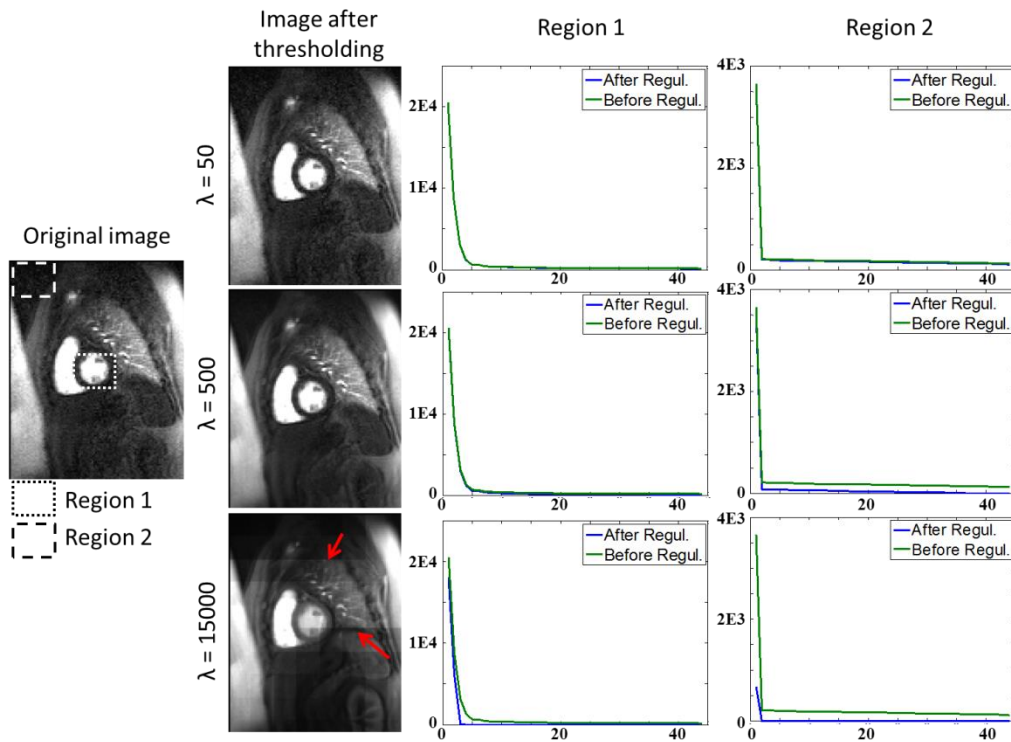


Figure 2.14 Example images and singular values before and after regularization using different threshold levels (λ values). Images showed visible blocking artifacts, i.e. discontinuities at block edges at a high threshold level ($\lambda = 15000$). Singular values from two regions, one over the left ventricle blood pool and the other over the background (squares on the original image), were calculated and compared. With the setting of norm $p = 0.9$, region 2 received more regularization than region 1. When λ increased to 15000 (bottom row), large singular values which contained most of the image energy and contrast information were influenced and gave rise to the blocking artifacts.

BLOSM is a motion-adaptive regional-sparsity-based CS method. Other methods such as k-t FOCUSS (16) and, recently, MASTeR (22) also incorporate motion compensation into a CS reconstruction. In k-t FOCUSS with motion estimation and compensation, although motions are estimated on a regional basis, x-f sparsity is exploited. In MASTeR, motion estimation varies regionally and temporal-difference sparsity is used. In contrast, BLOSM uses regional motion estimation and exploits regional matrix low-rank structure. Also, these three methods differ in

the details of the motion estimation algorithms, which likely affects resulting image quality. Previously, most CS methods for dynamic imaging have exploited sparsity using either whole images (such as k-t SLR) or single pixels (such as temporal difference or x-f sparsity). BLOSM, which exploits regional sparsity, is in between these two extremes, and provides the advantages of greater flexibility (compared to whole images) and use of more information (compared to single pixels). The k-t SLR method used in this study for comparison was modified to use the IST optimization algorithm and excluded the spatiotemporal total variation reported by Lingala et al (19). The modified k-t SLR method was used in order to make a fair comparison with BLOSM. Like k-t SLR, BLOSM could be extended to include extra sparsity constraints and could be solved by alternating direction algorithms (73). In this manuscript, we focused our efforts on evaluating BLOSM and other CS methods using only single-coil data. In the future we plan to combine BLOSM with parallel imaging such as SENSE (7) and Self-consistent Parallel Imaging (SPIRiT) (74) by exploiting joint sparsity (15,75-77) to achieve higher acceleration rates and better reconstruction quality. BLOSM is also compatible with non-Cartesian k-space trajectories. A limitation of our study was that, when comparing various reconstruction methods, we used magnitude-only datasets, thus phase effects were not accounted for. The magnitude-only data inherently promotes the k-space symmetry which was not exploited in this study. Clinical study with complex-valued data is needed to further evaluate the BLOSM method. The current study, in addition to RMSE, used SSIM which closely represents human perception for quality assessment. Spatial resolution quantification such as the signal profile transition width can be adopted in the future for more comprehensive quality assessment. With the usage of regional low-rank sparsity, it is difficult to estimate an up-bound of the possible acceleration rate of BLOSM. Higher acceleration rates will be evaluated in the future studies.

The present study focused on using BLOSM to reconstruct high-quality accelerated contrast-enhanced first-pass cardiac perfusion images, even in the presence of respiration due to imperfect breathholding. However, using the concepts of regional motion tracking and regional sparsity, BLOSM may also be applicable to other dynamic MRI such as cardiac cine imaging, T1 mapping, multi-TI arterial spin labeling, and other methods. Acceleration of these applications with BLOSM may be the subject of future studies. The computation time of BLOSM could also be improved in the future. The time consumed by the motion estimation (65% of total time) and block handling (21% of total time) can be decreased through better parallelization of the code and implementation using a graphics processing unit.

In summary, BLOSM makes use of data-driven spatiotemporal basis functions applied to regions and achieves motion compensation by embedding regional motion tracking into the iterative CS image reconstruction algorithm. With this combination, BLOSM attains the benefits of data-driven spatiotemporal basis functions while reducing artifacts from non-periodic motion such as breathing.

Chapter 3

Prospectively Accelerated CMR First-pass Perfusion Imaging in Patients with Suspected Heart Disease

First-pass perfusion CMR utilizes accelerated imaging to achieve high spatial resolution and coverage within a small acquisition window. Several compressed sensing (32) methods have been proposed to accelerate first-pass perfusion imaging (15,19,25,26,45). However, patient motion due to imperfect breathholding and other factors leads to degraded quality of CS-reconstructed images. We recently demonstrated a CS method (Block Low-rank Sparsity with Motion guidance, BLOSM) that exploits regional low-rank sparsity and compensates for the effects of motion, and the advantages of BLOSM were demonstrated using retrospectively-undersampled first-pass data (78). In the present study, prospectively-accelerated first-pass data were collected from patients undergoing clinically ordered CMR studies. BLOSM was combined with parallel imaging to reconstruct the data. High-quality reconstruction was achieved in heart-disease patients using BLOSM, even when substantial respiratory motion occurred. These findings support the use of regional low-rank sparsity with motion compensation for myocardial perfusion MRI.

3.1 Introduction

Cardiac first-pass perfusion imaging assesses myocardium blood flow by measuring the signal intensity changes caused by an injected contrast agent during its first passage through the heart, which usually only lasts for a few heartbeats. Fast imaging techniques are utilized to accelerate first-pass perfusion CMR to achieve high spatial resolution and coverage within this small acquisition window. Compressed sensing is a rapidly emerging and highly promising acceleration method (10). First-pass perfusion imaging is potentially well suited for CS acceleration since both spatial and temporal sparsity can be exploited. However, respiratory motion due to imperfect breathholding combined with the signal intensity change due to contrast passages, present complex dynamics, and if not handled properly, leads to degraded CS reconstruction quality

Over the years, several CS methods have been developed to accelerate first-pass perfusion imaging. Techniques, such as k-t Broad Linear Acquisition Speed-up Technique (k-t BLAST) and k-t sensitivity encoding (k-t SENSE) (79) used data covariance information obtained from the training data to re-distribute the aliased signals in the spatial and temporal-frequency (x - f) domain. These techniques act as the first iteration of the CS method k-t FOCUSS (16). The k-t BLAST and k-t SENSE techniques have been evaluated in several studies and high spatial-resolution images were achieved (80). However, respiratory motion resulted in severe image quality degradation (81).

k-t SPARSE-SENSE used sinusoidal basis functions to sparsify the images along the temporal direction and was combined with parallel imaging (15). The method was validated in two healthy volunteers and one patient on a 3T MRI scanner. k-t SLR used data-driven basis

functions to exploit low-rank sparsity in the images (19), where the basis functions were estimated from the data itself instead of using pre-fixed basis functions. The method showed promising improvement of image quality over the k-t SPARSE-SENSE method by using retrospectively accelerated radial trajectory data in a phantom and one human data (15). However, these two methods still showed degraded image qualities when respiratory motion presented.

Recently, a CS method exploiting localized spatio-temporal constraints was proposed for accelerated CMR perfusion imaging (26). To address the respiratory motion issue, the method used data driven basis functions to exploit regional sparsity, but no motion-compensation was performed. The method was validated in healthy volunteers and patients and showed good image quality for 3D and 2D imaging.

Our group has previously developed a CS method (Block LOW-rank Sparsity with Motion guidance, BLOSM) that used data driven basis functions to exploit regional low-rank sparsity and compensates for the effects of motion (78). Using 26 retrospectively-undersampled first-pass data and one computer simulated motion phantom, superior image quality even in the presence of significant motion was achieved by BLOSM, comparing to k-t SLR, a modified BLOSM without motion guidance and other CS methods (78). The use of both regional sparsity and motion tracking in BLOSM was demonstrated to work together to achieve improved image quality. However, the retrospective study used synthesized data derived from magnitude images. Clinical studies using prospectively accelerated acquisition are needed to further evaluate the performance of BLOSM.

In the present study, we evaluated BLOSM using prospectively-accelerated first-pass data collected from patients undergoing clinically ordered CMR studies, which demonstrated

true acceleration. Complex-valued and multi-coil data were collected and used for reconstruction. To handle multi-coil data and take advantage of the correlations among different coils, BLOSM was extended to incorporate with parallel imaging. Image quality was assessed using a score system and compared to a reference CS method k-t SLR, which exploits global low-rank sparsity without motion compensation.

3.2 Methods

3.2.1 Accelerated first-pass perfusion sequence

A saturation-recovery Cartesian TurboFLASH first-pass perfusion sequence was modified to realize CS acceleration. A variable-density k_y - t undersampling pattern was implemented, where the center phase-encode lines were fully sampled at all time points and the sampling density decreased towards the edges of k -space. To avoid “clusters” of the sampling points, the sampling positions are decided following a Poisson-disc distribution. In this way, each sampling point occupies a “forbidden disc” that no other points can reside in. The radius of the disc is designed as anisotropic, namely that the disc is an ellipse. The k_y radius varies at different k_y positions, where the center has the smallest distance and increases towards the edges. The t radius was kept the same for all time points. The resulting sampling pattern has variable sampling density along k_y and uniform density along the t direction. To avoid possible missing of the center lines, 35% of the total acquired lines were fully sampled around the center of k -space. To maintain the same acceleration rate for each image, the number of k_y lines were automatically adjusted to be the same at all time points. k_y lines at random places, except the center, are

removed or added to meet the desired acquired line number. From our observations, only a few lines for each frame need this adjustment, so the Poisson-disc distribution is still well maintained (Figure 3.1).

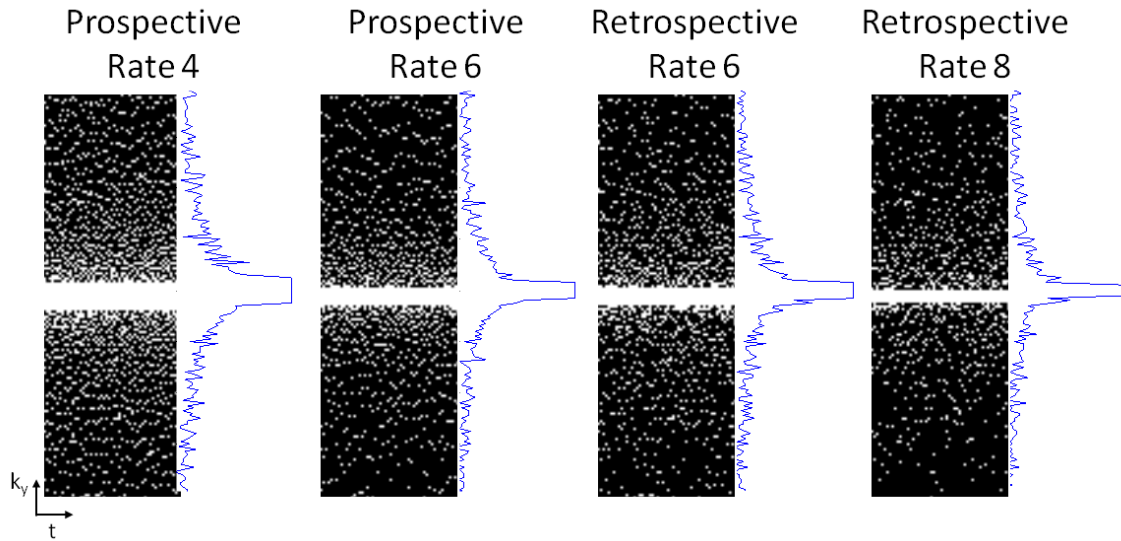


Figure 3.1 Example variable-density k_y - t sampling pattern following Poisson-disc distribution and corresponding sampling frequency at different k_y positions. The center of the k -space is fully sampled at all time points. The radius of the Poisson-disc increases from the center k_y towards the edge of the k space, resulting in decreased sampling density. Prospective rate 4 and 6 patterns are generated on the scanner. Retrospective rate 6 and rate 8 patterns are down-sampled from the prospective rate 4 pattern by randomly removing k_y lines. Note that the sampling frequencies of prospective rate 6 and simulated retrospective rate 6 are very similar.

3.2.2 Prospective-accelerated patient data collection

Accelerated multi-slice 2D first-pass gadolinium-enhanced data were collected from 12 patients undergoing clinically ordered CMR studies on a 1.5T Avanto scanner (Siemens Healthcare, Erlangen, Germany). Standard body phased-array RF coil was used under triple mode, resulting in 18-channel data. The imaging protocols were approved by our institutional

review board and informed consent was obtained before the study. For each patient, 3 short-axis tissue-function (TF) slices with saturation recovery time of 100 ms were acquired per heartbeat for 50-70 heartbeats during infusion of 0.075 mmol/kg gadopentetate dimeglumine (Magnevist, Bayer HealthCare, Montvale, NJ) followed by saline flush. The patients were instructed to hold their breath during the scan and to perform shallow breathing if their breath can no longer be held. Other imaging parameters included: nonselective BIR4 90° saturation pulse, matrix size = 160×320, spatial resolution = 1.8-2.1×1.8-2.1 mm², slice thickness = 8 mm, readout flip angle = 15°, repetition time = 2.4 ms, asymmetric echo = 78%. Prospectively rate-4 (rate 5.1 compared to full k-space) accelerated data were collected in 10 patients with acquisition window of 96 ms per slice. Prospectively rate-6 accelerated data were collected in 2 patients with acquisition window further shortened to 64 ms per slice. An additional low-resolution short-axis arterial-input-function (AIF) slice with saturation recovery time of 5 ms was also acquired per heartbeat for future quantitative perfusion analysis. The AIF slice was fully-sampled in this study and the acceleration was only performed on the TF slices. The data reconstruction in this work refers only to the TF data.

3.2.3 Retrospective-accelerated patient data simulation

To evaluate the CS methods at various acceleration rates, the 10 prospectively rate-4 accelerated patient data were further retrospectively down-sampled to simulate rate-6 and rate-8 acceleration. The high spatial frequency k_y lines were randomly removed from existing data to reach the desired increased acceleration rate without violating the poisson-disc rule. The ratio of the center fully-sampled k_y lines over the peripheral k_y lines were kept the same. Figure 3.1 showed example sampling patterns.

3.2.4 Data reconstruction

The BLOSM technique was extended to combine with sensitivity encoding (SENSE)(7) to handle multi-coil data and to take advantage of the correlation among RF coils in this study. In the extended BLOSM reconstruction, as illustrated in Figure 3.2, matrix low-rank sparsity is exploited within motion-tracked regions of SENSE-combined images. The coil sensitivity maps are calculated from temporally-averaged accelerated data (82) and are then used to combine multi-channel data into synthesized single-channel data for the iterative BLOSM reconstruction. The first frame of the combined images is spatially divided into square regions (blocks) as previously described (78). The blocks are motion tracked through all successive images using motion information obtained from image registration. The respiratory motion is thus compensated in these motion-tracked blocks. The motion-tracked blocks are grouped into clusters and rearranged into a 2D Casorati matrix where each block becomes a column of the 2D matrix. Singular values of the matrix are calculated using singular value decomposition (SVD) and undergo soft thresholding to promote low-rank sparsity, as the smaller values mainly represent noise. The de-noised clusters are then merged back into complete images and further distributed back to each coil using the sensitivity maps to compensate for data fidelity. The algorithm iterates until a predefined iteration number limit of 200 is reached. Complete implementation details of BLOSM were previously published (78). “BLOSM” used in the rest part of this chapter also refers to BLOSM with SENSE.

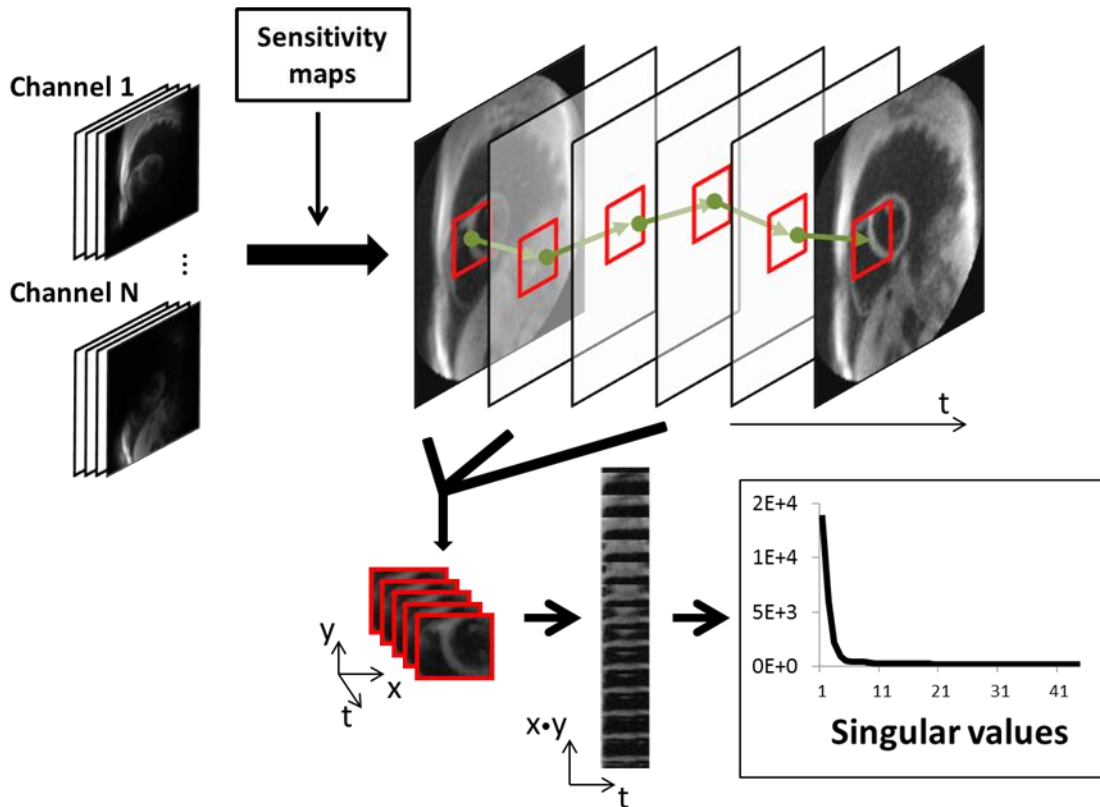


Figure 3.2 BLOSM with SENSE exploits matrix low-rank sparsity within motion-tracked regions from SENSE-combined images. After the multi-channel data are combined with SENSE, regions (blocks) are initialized on the first image. Each block is motion tracked to the succeeding images through time using motion trajectories from image registration. The blocks are gathered into a 3D cluster and further rearranged into a 2D matrix with high spatial-temporal correlations. The sparsity is exploited using singular value decomposition.

The accelerated data were reconstructed using BLOSM with SENSE and compared to k-t SLR. For fair comparison, k-t SLR was combined with SENSE following the method of combining of BLOSM with SENSE described above. The two CS methods were implemented using the same iterative soft thresholding (IST) optimization algorithm (65). The reconstruction parameters, especially the singular value thresholding level, were tested over a wide range and

for each method. Optimal parameters were selected based on previous retrospective study (78) and reconstructed image quality.

3.2.5 Reconstruction assessment

For the prospectively rate-4 accelerated reconstruction, two cardiologists scored the image from 1 to 5: 1: excellent apparent signal to noise ratio (aSNR) and no motion blurring; 2: very good aSNR and little motion blurring; 3: good aSNR and some motion blurring; 4: poor aSNR and strong motion blurring; 5: very poor aSNR and severe motion blurring. A motion degree score was also set up to evaluate how much motion, regardless of the motion recovery quality, can be observed in the image: 1: barely any motion; 2: some motion; 3: strong motion. Different slice data were considered as different studies. Thus a total of 10 (patients) \times 3 (slices) \times 2 (CS methods) = 60 image studies were scored. The order of the image studies was randomized before presented to the scorers for blind scoring.

Signal intensities from the left ventricle (LV) myocardium and the LV blood pool were obtained from the images. Myocardium and blood pool were contoured manually from reconstructed images from prospective rate 4 data using BLOSM for all frames to account for motion. The first few frames were not contoured since the image contrast has not arrived at the LV. The same contours were used for k-t SLR reconstructed images and retrospectively rate-6 and rate-8 accelerated studies, since the image quality from those reconstructions were too low to get accurate contouring.

3.3 Results

Figure 3.3 shows example reconstructed images using BLOSM and k-t SLR. Images at three time points from prospectively rate-4 (Pro R4), prospectively rate-6 (Pro R6) accelerated studies and retrospectively rate-6 (Retro R6), retrospectively rate-8 (Retro R8) accelerated studies simulated from the Pro R4 data are shown. With the presence of respiratory motion (Pro R4, Retro R6, Retro R8), images reconstructed using BLOSM presented high quality with clear delineation of the myocardium. With increased acceleration rates, BLOSM showed subtle degradation. In contrast, k-t SLR presented motion blurring at all acceleration rates. BLOSM achieved consistent high quality images with prospective rate-6 acceleration (bottom row). However, the improvement over k-t SLR was subtle due to the lack of respiratory motion in those datasets. Figure 3.4 showed the corresponding spatial-temporal profiles of the reconstructions in Figure 3.3. Profiles across the heart along the vertical direction (y-t) and the horizontal direction (x-t) are shown in different columns. Strong motion in the Pro R4, Retro R6 and Retro R8 can be clearly seen from the spatial-temporal files. The BLOSM reconstruction provided high quality motion recovery without motion blurring. The k-t SLR reconstruction showed severe motion blurring when respiratory motion occurred.

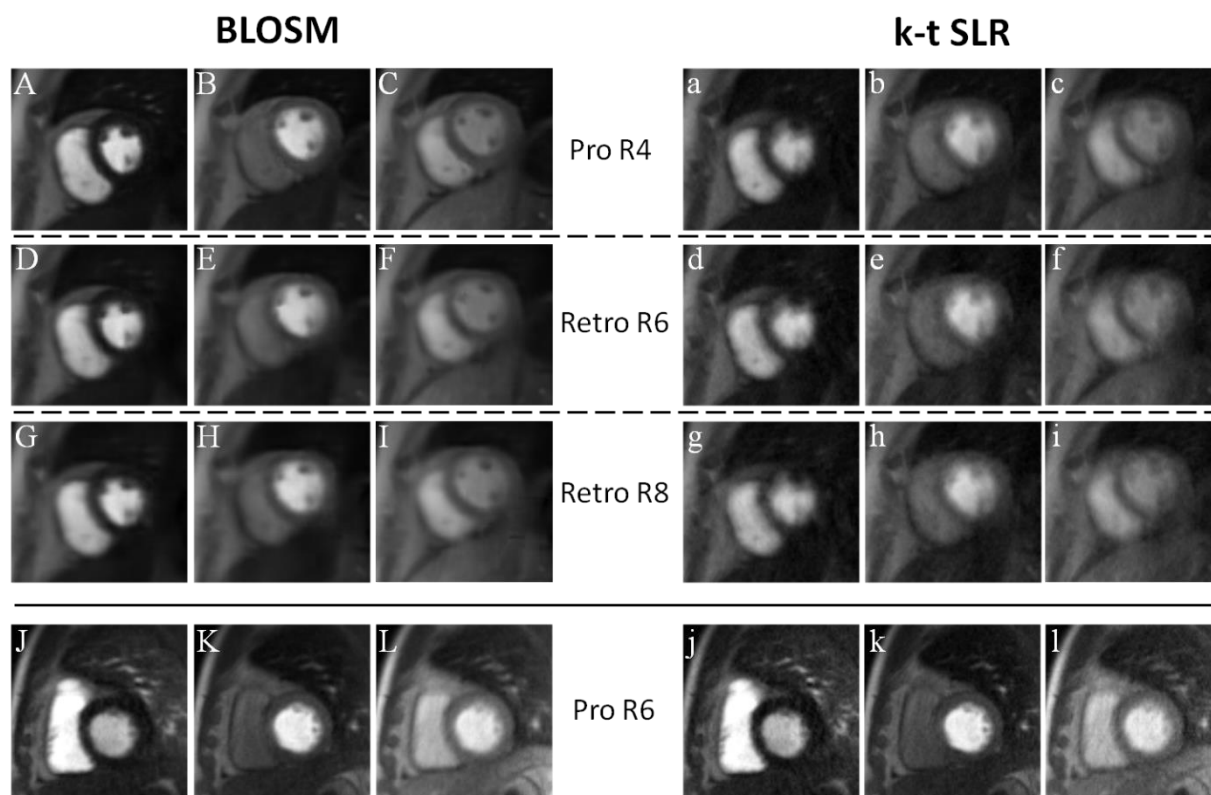


Figure 3.3 Example reconstruction images using BLOSM (A-L) and k-t SLR (a-l) at various acceleration rates. Images from prospectively accelerated rate-4 scan (A-C, a-c) and corresponding retrospectively sub-sampled rate-6 (D-F, d-f) and rate-8 (G-I, g-i) were shown in the top panel. Images from prospectively accelerated rate-6 scan (J-L, j-l) were shown in the bottom. Images at early, mid and late time points were shown in different columns. The top panel images present strong respiratory motions. BLOSM reconstructions showed the best image quality with respect to noise removal and motion preservation. The BLOSM quality preserved with increased sub-sampling rates. k-t SLR suffered from blurring for all accelerations. In the Pro R6 study, BLOSM presented consistent high image quality. k-t SLR presented similar quality as BLOSM, since the images presented few motions in this study.

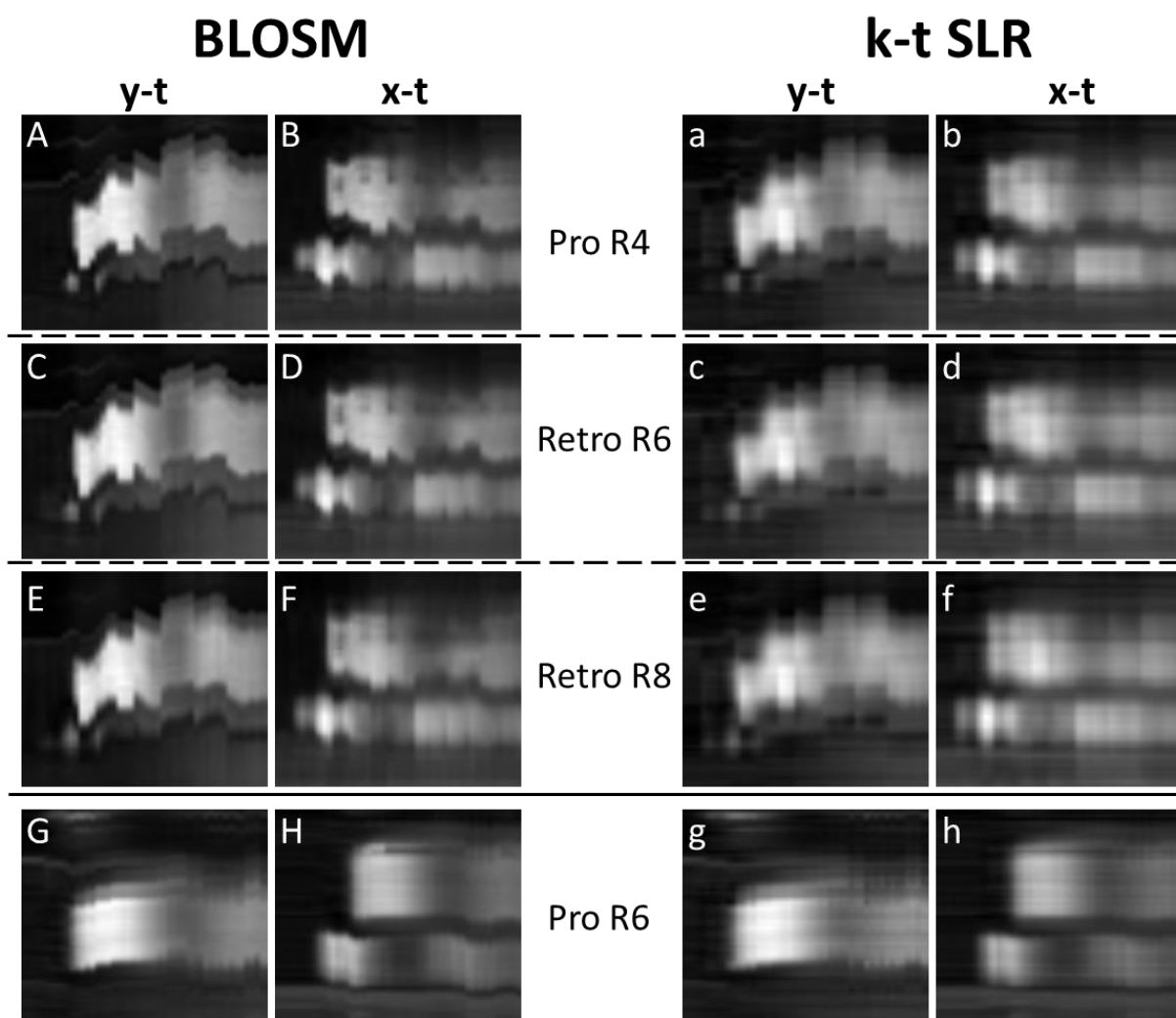


Figure 3.4 Example vertical (y - t) and horizontal (x - t) spatial-temporal profiles across the heart from BLOSM (A-H) and k-t SLR (a-h). The profiles were obtained using the same example data used in Figure 3.3. For prospective rate-4 (Pro R4, A, B, a, b), retrospective rate-6 (Retro R6, C, D, c, d) and retrospective rate-8 data (Retro R8, E, F, e, f), strong respiratory motions can be observed in both directions. The BLOSM reconstruction provided clear motion depiction while the k-t SLR presented severe motion blurring at all acceleration rates. Limited motion can be observed from the prospective rate-6 (Pro R6, G, H, g, h) data, and BLOSM and k-t SLR performed similarly in this case, although some subtle motion blurring can still be observed on the k-t SLR reconstruction.

Image quality and motion degree scores by the two cardiologists for Pro R4 images were summarized in Table 3.1 and Table 3.2. BLOSM showed significant better image quality ($p < 0.01$). Also the motion degree score indicated that the data from the 10 patients presented considerable level of motions.

Table 3.1 Summary of image quality and motion degree scores. The average score from the two scorers are listed. The scores were then averaged over different image studies and standard deviation was calculated.

	BLOSM	k-t SLR
Quality (1~5, 1 the best)	2.1±0.8	2.9±0.7
Motion Degree (1~3, 1 no motion)	2.3±0.7	2.2±0.7

Table 3.2 Summary of all image quality scores from the two scorers on the prospectively rate-4 accelerated data. Count and frequency of each score level are shown.

		Excellent	Very Good	Good	Poor	Very Poor	Total
Scorer 1	BLOSM	14 <u>47%</u>	7 <u>23%</u>	5 <u>17%</u>	4 <u>13%</u>	0 <u>0%</u>	30 <u>100%</u>
	k-t SLR	6 <u>20%</u>	10 <u>33%</u>	7 <u>27%</u>	1 <u>20%</u>	0 <u>0%</u>	30 <u>100%</u>
Scorer 2	BLOSM	10 <u>34%</u>	7 <u>23%</u>	10 <u>33%</u>	3 <u>10%</u>	0 <u>0%</u>	30 <u>100%</u>
	k-t SLR	0 <u>0%</u>	1 <u>3%</u>	16 <u>54%</u>	13 <u>43%</u>	0 <u>0%</u>	30 <u>100%</u>

Figure 3.5 shows example BLOSM results from a patient with perfusion defect and prominent respiratory motion (D), along with a corresponding LGE image showing scar (E). The perfusion defect regions recovered by BLOSM matched well with the LGE scar regions.

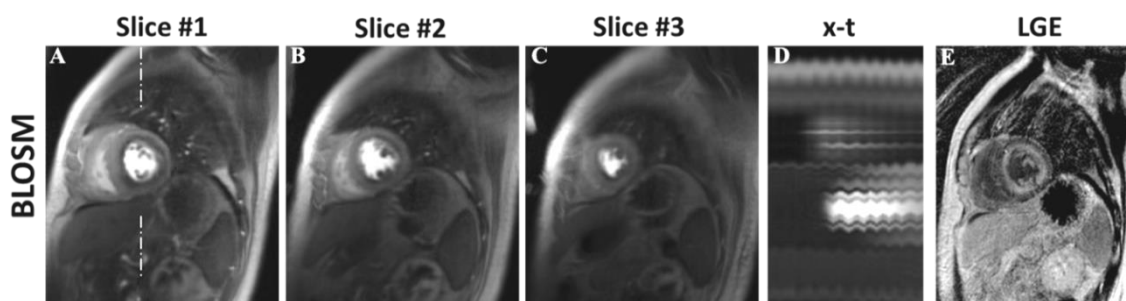


Figure 3.5 Example BLOSM reconstruction results from one patient with amyloidosis. Multi-slice images from one time point are shown (A-C), along with the x-t profile (D) and a corresponding LGE image (E). A subendocardial perfusion defect is clearly depicted by BLOSM, even in the presence of respiratory motion during the scan, as illustrated in the x-t profile. The subendocardial perfusion defect location matched closely with enhancement on the LGE image.

3.4 Discussion

Previously, BLOSM was evaluated using retrospectively accelerated first-pass perfusion data, where the fully sampled data were acquired first and retrospectively undersampled (78). In this study, BLOSM was applied to prospectively accelerated data in patients with suspected heart disease. Benefitting from the true acceleration, multi-slice high spatial resolution perfusion imaging were enabled.

Using the prospectively accelerated data, BLOSM achieved high quality reconstructions even at the presence of respiratory motion, consistent with the previous retrospective acceleration studies. The current study also overcame the limit of the former study where only single channel data synthesized from magnitude images was reconstructed. Parallel imaging technique was proven to be compatible with BLOSM reconstruction.

The advantages of utilizing regional sparsity and motion compensation were demonstrated by comparing BLOSM to k-t SLR. When small respiratory motion was presented,

the image quality from k-t SLR was similar to BLOSM. However, as shown in Figure 3.3 and Figure 3.4, when strong respiratory motion occurred during the scan, BLOSM showed superior reconstruction quality over k-t SLR. Severe motion blurring artifacts can be observed on images reconstructed using k-t SLR. This demonstrated that BLOSM is robust for first-pass perfusion imaging, regardless of the respiratory motion. However, for other CS methods such as k-t SLR, which estimated basis functions from the whole images without motion compensation, fails to sparsify the data in this case. To further demonstrate this, a wide range of the singular value thresholding levels (250~2000 for BLOSM, 500~15000 for k-t SLR), which mainly control the denoising performance of the CS method, were tested using the same accelerated data for both BLOSM and k-t SLR. The reconstruction results were shown in Figure 3.6. Standard deviation of the signals from a background region was calculated to represent the noise level, as shown in Figure 3.7. With the increase of the thresholding level, the noise levels from both methods dropped accordingly. At matched noise level, k-t SLR demanded a much stronger thresholding, which also led to severe motion blurring. On the other hand, BLOSM showed an overall low noise level and the motion was well preserved for a range of thresholding levels. This also indicated that BLOSM may require less parameter tuning among different datasets.

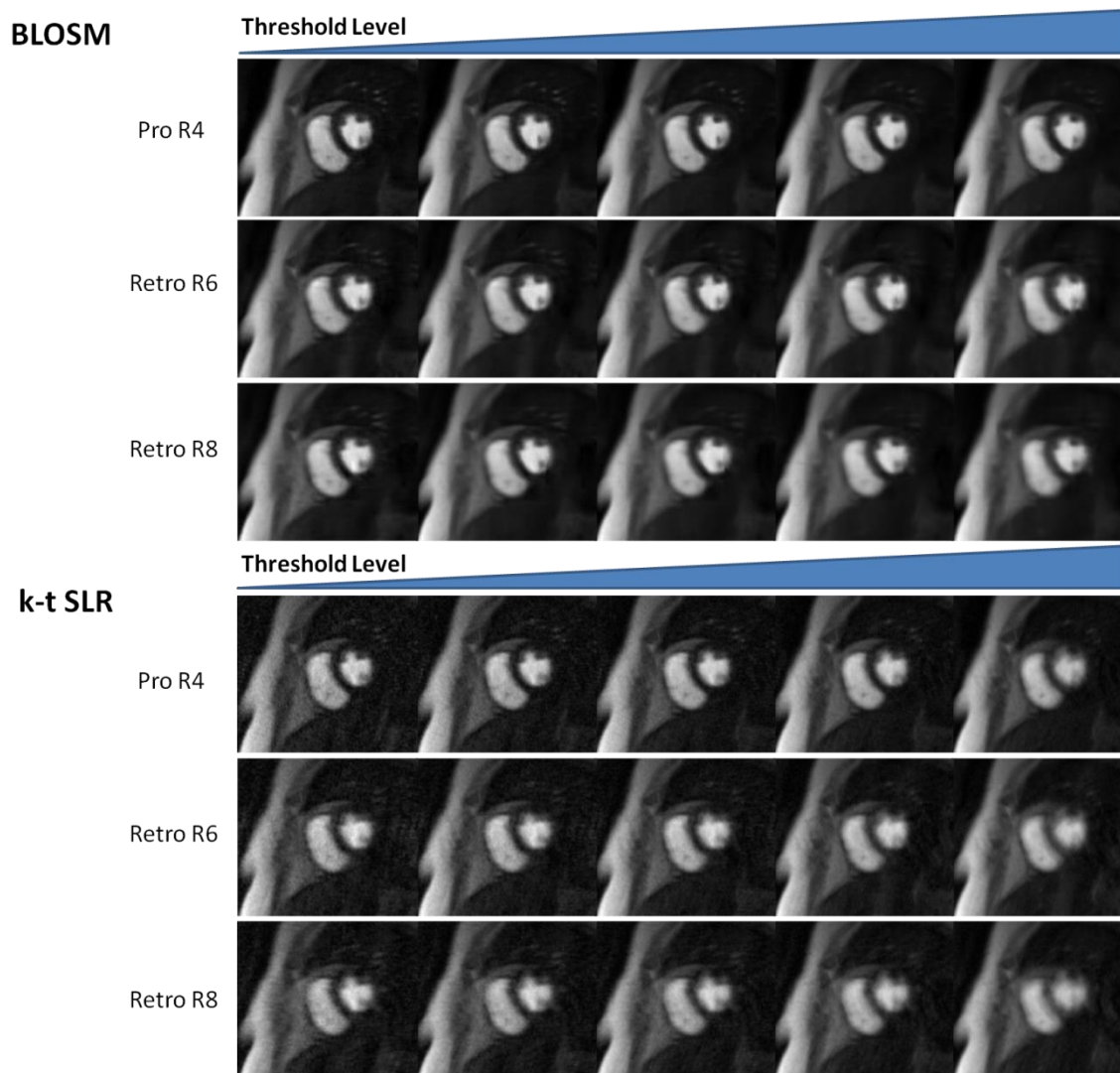


Figure 3.6 Example images at one time point reconstructed using different threshold level. The threshold level increases from left to right, representing stronger regularization. Data at different acceleration rates reconstructed by BLOSM and k-t SLR are shown in different rows. BLOSM presented good noise removal performance at all levels of thresholding. Subtle increase of motion blurring can be observed as the threshold level increases in BLOSM. In contrast, images reconstructed by k-t SLR presented high level of residual artifacts at low threshold level. The artifacts were removed at the cost of increased motion blurring in k-t SLR.

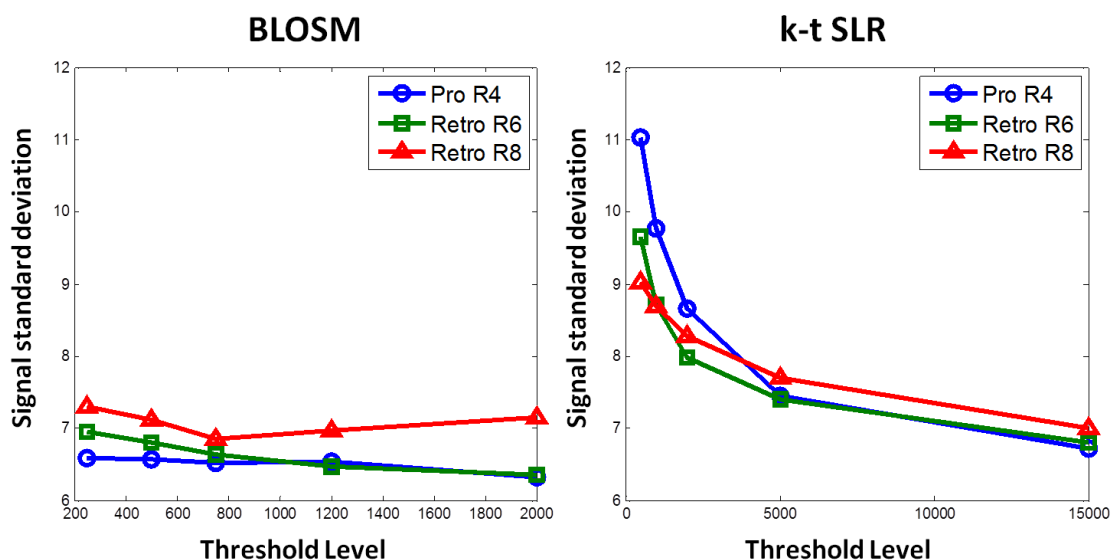


Figure 3.7 Example standard deviation of signals from a background region over a wide range of threshold levels. Signals were obtained from the same images reconstructed by BLOSM and k-t SLR shown in Figure 3.6. High threshold values are needed in k-t SLR to match the same noise level in BLOSM. At low threshold level where k-t SLR presented moderate motion blurring, the noise level is much higher than BLOSM.

Higher acceleration rate of 6 and 8 were simulated from prospectively accelerated rate 4 data to evaluate BLOSM at higher acceleration rates. The retrospective study provided a close to reality situation without acquiring multiple data from one patient, which is almost impossible in first-pass perfusion study. Similar observations by comparing BLOSM and k-t SLR can be drawn from the retrospective studies as from the prospectively rate 4 study. BLOSM showed moderate quality degrade as the acceleration rate increased. The prospectively rate-6 accelerated images from BLOSM showed consistent good performance in the retrospective study. We also observed from some of the patients studies that at high acceleration rates, the strong fat signals from the chest and/or the back regions were more overlapped onto the heart region. The CS regularization power was increased for those studies and sometimes moderate residual artifacts

could still be observed. In the future, techniques such as fat-saturation RF pulses or outer-volume suppression preparation can be adopted to decrease the influence of the strong fat signals from regions that are not of interest.

In this study, the sensitivity maps were calculated from temporal averaged data. The RF coil sensitivities may alter due to respiratory motions and time-varying sensitivity maps may benefit the reconstruction quality using CS and PI combined methods. Obtaining time-varying sensitivity maps are feasible in our study settings because the center fully sampled k-space from the variable density k-t sampling can be used to generate low spatial-resolution but high temporal-resolution images for sensitivity maps calculation. This will be studied in the future studies.

In summary, using prospectively accelerated data, BLOSM showed improved reconstruction quality compared to k-t SLR, demonstrating the utility of regional sparsity and motion compensation. BLOSM may provide clinically acceptable image quality at higher acceleration rates such as 6, even with the presence of respiratory motion.

Chapter 4

Accelerated 2D Cine DENSE using BLOSM

Cine Displacement Encoding with Stimulated Echoes (DENSE) provides accurate quantitative imaging of the heart with rapid displacement and strain analysis; however, image acquisition times are relatively long. In this study, an accelerated cine DENSE sequence with variable-density spirals and golden angle rotations was implemented. Prospectively and retrospectively accelerated data were collected in 7 healthy volunteers, and a computer-simulated phantom was also used. A previously developed CS method, Block Low-rank Sparsity with Motion-guidance (BLOSM) was combined with Sensitivity encoding (SENSE), and BLOSM-SENSE was compared to SENSE and to k-t SPARSE-SENSE. At acceleration rates of 4 and higher, BLOSM-SENSE showed superior image quality quantified by lower root mean square error and higher signal-to-noise ratio. Myocardial circumferential strain calculated from BLOSM-SENSE reconstructed images showed better agreement with the reference data. BLOSM-accelerated spiral cine DENSE images with 2D in-plane displacement encoding can be acquired in a single breathhold, as short as 8 heartbeats. These methods promise to improve clinical MRI of myocardial strain.

4.1 Introduction

Imaging myocardial strain is of growing importance for the clinical assessment of heart disease (3,32-34). MRI myocardial tagging, a long-established method, has been considered the gold standard as compared to strain imaging using echocardiography (34,35). However, recently within the MRI modality, cine displacement encoding with stimulated echoes (DENSE) (36-38) has emerged as a strain imaging technique that, compared to tagging, has equivalent accuracy and better reproducibility (39), and where strain analysis is less time consuming (35,40,41). While cine DENSE holds these advantages, it also has the disadvantage that data acquisition times are relatively long. Currently, tagged images using two-dimensional (2D) grid tags are typically acquired during a single breathhold (34), whereas common protocols for 2D cine DENSE typically require two separate breathholds, each with 1D displacement encoding (42). Acceleration using data undersampling could substantially shorten the scan time and/or provide improved temporal resolution for cine DENSE. However, the relatively low signal-to-noise ratio (SNR) inherent to stimulated echoes presents challenges to acceleration techniques such as parallel imaging (PI), which reduce scan time at the expense of SNR (43).

Compressed sensing (32) is a newer acceleration technique which is making a major impact on MRI (10) and which typically has SNR advantages compared to PI (15,75,83). In CS, high-quality images can be recovered from data sampled well below the Nyquist rate. Dynamic MR images such as those acquired by cine DENSE are in some ways inherently suitable for acceleration using CS since the data present both spatial and temporal sparsity (12,16,44); however, the specific complex dynamics involved in cine DENSE data also present challenges. In particular, cine DENSE images feature cardiac contraction and relaxation coupled with signal

intensity changes due to T1 relaxation of the stimulated echo. Also, complex-valued image reconstruction is required because the displacement-encoded signal phase is used to compute myocardial motion and strain. Lastly, as noted above, the SNR of stimulated echoes is relatively low.

Recently data-driven sparsity transforms such as principal component analysis (PCA) and singular value decomposition (SVD) have been successful for accelerating MRI acquisitions containing both motion and signal amplitude modulations (17,19). Even more recently, these methods have been improved by exploiting regional sparsity, where the sparsity transform is applied to regions rather than whole images (26,84,85). For dynamic methods utilizing regional sparsity, motion compensation can improve image quality as demonstrated using methods such as Block LOw rank Sparsity with Motion guidance (BLOSM) and others (78,86,87).

Given the recent success of motion-compensated regional data-driven methods for accelerating complex dynamic acquisitions with motion and signal intensity variations, we aimed to extend and evaluate the BLOSM technique for accelerating cine DENSE. Since cine DENSE benefits from spiral k-space sampling and the use of RF coil arrays (37,38), we extended BLOSM to reconstruct data from variable density spiral trajectories and to incorporate PI (88,89). Our evaluation of BLOSM-accelerated cine DENSE was performed using computer-simulations and in vivo imaging of volunteers. For all evaluations, BLOSM-accelerated cine DENSE was compared to k-t SPARSE with sensitivity encoding (k-t SPARSE-SENSE), which has previously been used to accelerate velocity-encoded MRI (76), a dynamic phase-contrast MRI method with similarities to cine DENSE.

4.2 METHODS

4.2.1 Data acquisition

A previously-described spiral cine DENSE sequence (37,38) was modified for the present study. In cine DENSE, after the detection of an ECG R-wave, a displacement-encoding module is applied to encode tissue position into the longitudinal magnetization. Later in the cardiac cycle, displacement-encoded stimulated echoes are acquired at multiple cardiac phases, where tissue displacement relative to end-diastole is encoded in the signal phase as $\theta = \{\mathbf{k}_e \cdot \Delta \mathbf{x} + \varphi\}_{2\pi}$, where θ is the phase value, \mathbf{k}_e is the displacement-encoding frequency which is applied in a particular direction, $\Delta \mathbf{x}$ is the tissue displacement along the \mathbf{k}_e direction, φ is the background phase due to factors such as magnetic field inhomogeneity, and $\{*\}_{2\pi}$ takes the modulus of 2π . To obtain 2D displacements, a simple encoding strategy is employed that utilizes three datasets with \mathbf{k}_e applied in orthogonal x and y directions and with $\mathbf{k}_e = 0$ for phase reference data. Alternatively, balanced three-point displacement encoding can be used, which also requires the acquisition of three datasets (90). Throughout this paper, the simple encoding case will be assumed, however the BLOSM method can be easily adapted to the balanced encoding case. In addition, two-point phase cycling (90) and through-plane dephasing (91) are used to suppress artifact-generating echoes from T1-relaxation and conjugate signals. Considering all of these factors, a complete fully-sampled 2D spiral cine DENSE scan requires a total number of acquisitions per image given by $N_{\text{leaves}} \cdot N_{\text{enc}} \cdot N_{\text{phyc}} / N_{\text{segment}}$, where N_{leaves} is the number of spiral interleaves, N_{enc} is the number of displacement-encoding directions (inclusive of the phase

reference acquisition), N_{phcyc} is the phase-cycling factor, and N_{segment} is the number of spiral interleaves acquired per heartbeat.

Variable-density spiral k-space trajectories are well-suited for acceleration because the center of k-space can be sampled with high density and the sampling density can be decreased for higher spatial frequencies (31,92,93). We implemented variable-density spiral trajectories to accelerate cine DENSE with CS-PI, where the initial sampling density for the center portion (~25%) of k-space fulfilled the Nyquist criterion and the sampling density decreased smoothly as the trajectories progressed to higher spatial frequencies. Multiple spiral interleaves per image were generated by rotating one variable-density spiral interleaf uniformly by $2\pi/N_{\text{leaves}}$. To accelerate data acquisition, N_{leaves} and the ending sampling density were reduced while the initial sampling density was maintained to obtain similar fields of view and resolutions for different acceleration rates.

To promote data incoherence along time, the variable-density spiral trajectories were rotated by a golden angle through different cardiac phases. The spiral trajectories were unchanged as the phase of the displacement-encoding pulses cycled (phase cycling) and as the displacement-encoding direction changed.

4.2.2 Data reconstruction

The BLOSM technique, which was recently developed and applied to accelerate first-pass contrast-enhanced perfusion MRI (78), was extended by incorporating sensitivity encoding (SENSE) (7) to reconstruct multi-coil data. The BLOSM-SENSE reconstruction method has been introduced previously in this dissertation (Chapter 3.2.4). Special designs, however, are needed to apply BLOSM-SENSE to cine DENSE imaging.

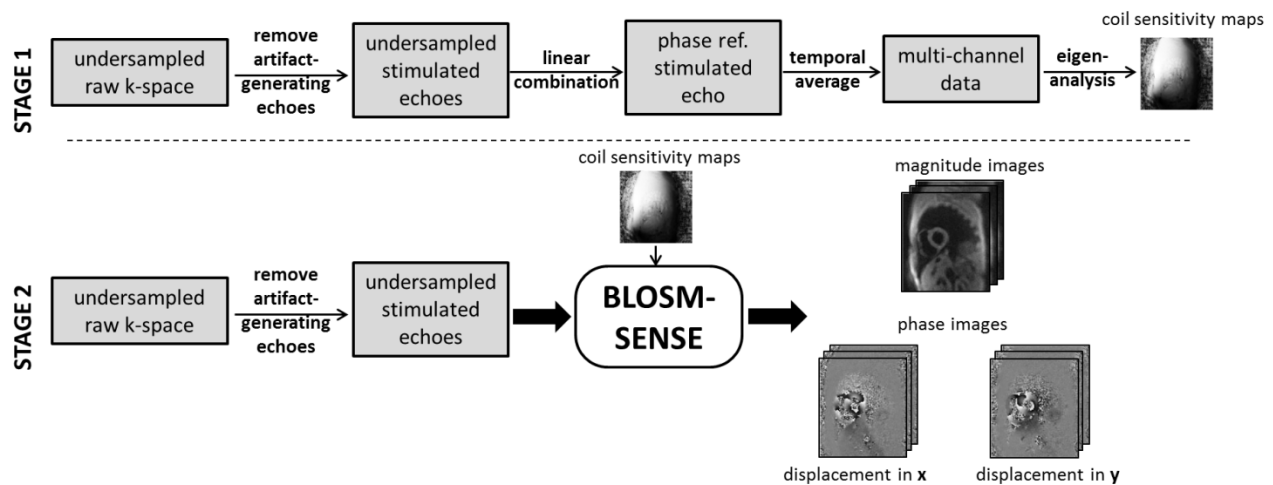


Figure 4.1 BLOSM-SENSE reconstruction of 2D cine DENSE. The reconstruction includes: calculation of sensitivity maps (stage 1) and BLOSM-SENSE reconstruction (stage 2). The undersampled phase-cycled raw k-space data are first subtracted to remove T1-relaxation echoes. The subtracted undersampled stimulated echoes undergo a linear combination to extract the background phase reference stimulated echo. The phase reference data are transformed into images, averaged over time and eigen-analysis is applied to obtain coil sensitivity maps. At the second stage, the undersampled stimulated echoes subtracted from the undersampled raw-k-space data are input for the BLOSM-SENSE CS-PI algorithm. BLOSM-SENSE uses the calculated sensitivity maps to exploit matrix low-rank sparsity within motion-tracked regions from SENSE-combined images. The final outputs of the iterative BLOSM-SENSE reconstruction are magnitude images and phase images with orthogonal 2D displacement encoding.

The first stage of the BLOSM-SENSE method is to calculate sensitivity maps (Figure 4.1, top). In the first step, the undersampled phase-cycled raw k-space data undergoes subtraction to remove the-artifact generating T1-relaxation echo. The subtracted undersampled stimulated echoes undergo a linear combination to extract background phase reference data (36,90). Background phase reference data are transformed to images and averaged over all cardiac phases, from which the coil sensitivity maps are estimated using eigen-analysis (82). The coil sensitivity maps are then used to combine multi-coil data into synthesized single-coil data later in stage 2.

The second stage of BLOSM-SENSE is to apply the iterative BLOSM algorithm to the SENSE-combined images (Figure 4.1, bottom). Briefly, matrix low-rank sparsity is exploited within motion-tracked regions of SENSE-combined images. Detailed description please refer to Chapter 3.2.4. The algorithm iterates until a predefined iteration number limit of 200 is reached. The final outputs are magnitude-valued images and phase-valued images with orthogonal 2D displacement encoding.

The BLOSM-SENSE optimization problem can be described with a modification of the original BLOSM cost function as:

$$\mathbf{m}^* = \arg \min_{\mathbf{m}, \mathcal{R}} \|\mathcal{F}_u \mathbf{S} \mathbf{m}_c - \mathbf{d}\|_2 + \lambda \|\Phi_{\mathcal{R}} \mathbf{m}_c\|_{p^*} \quad [4.1]$$

where \mathbf{m}_c represents the coil-combined estimated dynamic images, \mathbf{S} represents coil sensitivities, \mathbf{d} is the acquired undersampled k-space data, and \mathcal{F}_u is the undersampled non-uniform fast Fourier transform (NUFFT) (94) which only takes values at the k-space positions where the \mathbf{d} are acquired. $\Phi_{\mathcal{R}}$ represents the operator for block tracking and creation of rearranged clusters after \mathbf{m}_c is divided into blocks which are tracked using displacement maps \mathcal{R} . $\|\cdot\|_{p^*}$ is a joint Schatten p -norm that exploits the regional low rank property. Note that although only the magnitude images were used for motion estimation, complex-valued blocks were tracked and subjected to SVD, thereby preserving phase information. The only differences between Equation 4.1 and the prior description of BLOSM (78) are that Equation 4.1 incorporates sensitivity encoding and utilizes the NUFFT to handle spiral trajectories.

The BLOSM-SENSE algorithm described above can be applied separately to datasets acquired with different displacement encoding directions. However, correlations exist among the different encoding directions since the underlying objects and motions are the same. By exploiting the joint correlations (joint-encoding sparsity), we investigated whether better

reconstruction quality can be achieved compared to separately using independent datasets. To exploit joint-encoding sparsity, the images from different encodings were motion tracked together and SVD was applied to a combined 2D matrix containing data from all encoding directions. Specifically, the magnitude images were averaged over the different encodings and block motion was estimated from the averaged magnitude images. This ensured that the motion-tracked blocks on all images with different displacement encoding frequencies were at the same locations. After the blocks were collected into clusters and were rearranged into the 2D matrices, the matrices from the multiple encodings were concatenated along the temporal direction. The new joint 2D matrix has the size of N_b by $N_t \cdot N_{enc}$, where N_b is the number of pixels in a block and N_t is the number of time points. SVD was applied to this joint 2D matrix. This method is termed BLOSM-SENSE with joint encoding sparsity (BLOSM-SENSE-joint), as distinguished from BLOSM-SENSE applied independently to each displacement encoding frequency (BLOSM-SENSE-ind).

4.2.3 Evaluation using computer-simulated phantom

Computer-simulated data have previously been used to evaluate new algorithms for improving cine DENSE (41,95). In the present study, a computer-simulated cardiac phantom was generated to mimic 2D cine DENSE data representing a contracting left ventricle in a short-axis view. As shown in Figure 4.2, two concentric circles were generated to represent the epicardial and endocardial borders. Cardiac contraction and relaxation were simulated by deforming the two borders simultaneously, as described previously (41). Myocardial displacement values were pre-defined on a high resolution grid and down-sampled onto the low-resolution imaging grid. The displacements were transformed into image phase values using $\theta = \{\mathbf{k}_e \cdot \Delta \mathbf{x}\}_{2\pi}$. The magnitude

images mimic cardiac geometry and motion and the phase images reflect simulated cardiac displacements. Two-dimensional displacement encoding was simulated with an encoding frequency $\mathbf{k}_e=0.1$ cycles/mm along orthogonal \mathbf{x} and \mathbf{y} directions, and with $\mathbf{k}_e=0$ for phase reference data. No additional artifact-generating echoes were simulated. Noise was added to the complex-valued images, and raw k-space data on spiral trajectories were computed using the NUFFT . For the computer-simulated phantom, the variable density spiral trajectories described in Table 4.1 were used to simulate fully-sampled data and rate-2, rate-4 and rate-8 accelerated data, respectively. Other parameters included FOV = 192 x 192 mm² and matrix size = 96-102 x 96-102. Single-coil acquisitions were simulated for the phantom.

Table 4.1 Parameters of the variable density spiral trajectories for fully-sampled and accelerated acquisitions. The reference sampling density of 1 corresponds to the Nyquist rate.

	Number of interleaves	Initial sampling density	Ending sampling density
Full	8	3	0.8
Rate 2	4	1.2	0.4
Rate 4	2	1.2	0.12
Rate 8	1	1.2	0.03

4.2.4 Evaluation using in vivo data

Short-axis 2D cine DENSE images of the left ventricle were collected from healthy volunteers ($n = 7$) on a 1.5T MRI scanner (Avanto, Siemens, Erlangen, Germany) with a 5-channel body-spine combined RF coil array. The scans were performed in accordance with protocols approved by our institutional review board after informed consent was obtained. Fully-sampled datasets with 2D in-plane displacement encoding and $N_{\text{leaves}} = 6$ to 8 spiral interleaves per image were acquired within a long breathhold (20 to 26 heartbeats), and prospectively accelerated datasets at rate-2 and rate-4 acceleration (with 4 and 2 spiral interleaves per image) were acquired within shorter breathholds of 14 and 8 heartbeats, respectively.

Retrospective acceleration studies were performed using the fully-sampled data, where the data were retrospectively undersampled at rate-2 and rate-4. The fully-sampled data were acquired using spiral trajectories described in Table 1. The retrospectively rate-2 and rate-4 undersampled datasets had $N_{\text{leaves}} = 4$ and 2, respectively, initial sampling densities of 1.5 and 0.75, respectively, and ending sampling densities of 0.4 and 0.2, respectively.

Prospective acceleration was also performed at rate-2 and rate-4, using 4 and 2 spiral interleaves per image, respectively. To match the spatial resolution of the fully-sampled data, rate-2 and rate-4 accelerated data used spiral trajectories described in Table 1. Other imaging parameters included field of view (FOV) of 280-320 x 280-320 mm², in-plane spatial resolution of 1.8-2.2 x 1.8-2.2 mm², slice thickness = 8 mm, ramped flip angle with the last flip angle = 15°, TR = 9.8 ms, TE = 1.3 ms, $N_{\text{segment}} = 2$ spiral interleaves per heartbeat, temporal resolution = 19.6 ms, cardiac phases 35-38, 2-point phase cycling ($N_{\text{phcyc}} = 2$), and simple 3-point displacement encoding ($N_{\text{enc}} = 3$).

4.2.5 Comparison of reconstruction methods

The undersampled data were reconstructed using BLOSM-SENSE with independent encoding and with joint encoding. The BLOSM-SENSE methods were compared to k-t SPARSE-SENSE (76). For k-t SPARSE-SENSE, a Fourier transform was taken along the temporal direction to transform the dynamic images into the spatial and temporal-frequency (x-f) domain. Then PCA was performed to transform the x-f matrix to the spatial and principal-components domain (x-PCA) domain. This technique also combines CS with SENSE, as the sparsifying transforms were performed on the SENSE-combined data. In previous work the temporal-frequency-expanded x-f matrix included both velocity-encoded and phase reference data (76), similar to the joint-encoding sparsity used in the present BLOSM-SENSE-joint algorithm. Thus, we implemented k-t SPARSE-SENSE with joint-encoding sparsity where the expanded x-f matrix uses all encoding data on the time dimension. We used the same iterative soft threshold (IST) algorithm (65) to solve both BLOSM-SENSE and k-t SPARSE-SENSE optimization problems. The soft thresholding weighting factor for the sparsity term was

optimized independently for each method. Other parameters for BLOSM-SENSE were set as reported previously (78). The undersampled multi-coil data were also reconstructed using SENSE alone. The fully-sampled data and the undersampled data were also reconstructed using the sum-of-squares (SOS) method. All reconstructions used NUFFT to transform data between the image and k-space domains.

For retrospectively accelerated data, image quality for the various reconstruction algorithms was quantified using the root mean square error (RMSE). Complex-valued images were used in the RMSE calculations shown below. RMSE values were averaged over all the cardiac phases and RMSE was defined as

$$\text{RMSE} = \frac{1}{N} \sqrt{\sum \frac{|x-y|^2}{|x|^2}} \quad [4.2]$$

where $N = N_x \times N_y \times N_t$, \mathbf{x} are the fully-sampled images and \mathbf{y} are the images reconstructed from retrospectively undersampled data.

RMSE for regions of interest (ROIs) on the phase-reconstructed images were also calculated. ROIs were selected using a semi-automatic process described below that delineates the myocardium. Also, SNR values were estimated for the reconstructed images. SNR values were averaged over all the cardiac phases and SNR was defined as

$$\text{SNR} = \frac{\overline{S_{\text{obj}}}}{\sqrt{\overline{S_{\text{bg}}^2} - \overline{S_{\text{bg}}}^2}} \quad [4.3]$$

where S_{obj} is the regional signal from the imaged object and S_{bg} is the regional signal from the background. For simplicity, the liver was used for the object region and the background region was the area in front of the chest wall. Identical regions were used for the same datasets reconstructed using different methods.

4.2.6 Functional analysis

Myocardial displacement and strain were computed using semi-automatic previously published cine DENSE analysis algorithms (96). To calculate myocardial strain, initial endocardial and epicardial contours were manually delineated at one cardiac phase and propagated automatically to all other cardiac phases (40). After this segmentation process, the phase-reconstructed images were phase-unwrapped and strain values were calculated (96). Circumferential strain (E_{cc}) is the most commonly reported strain element (35) and was selected in this study to evaluate the reconstruction algorithms. To limit user-dependent variability, different reconstructions of the same prospectively or retrospectively accelerated data used the same initially defined contours. Short-axis images were segmented into 6 regions according to the standard American Heart Association model (97) and segmental E_{cc} values at all cardiac phases were recorded. Linear regression and Bland-Altman analysis were performed to assess correlations and agreement between the accelerated reconstructions and the reference data.

4.3 RESULTS

4.3.1 Computer-simulated phantom

Results from computer-generated phantoms demonstrate that BLOSM-SENSE with joint encoding has advantages compared to the other methods that were evaluated. Figure 4.2 shows example phantom images from computer-generated data that simulated rate-4 acceleration. Magnitude and phase images (with displacement encoding applied in the x direction) at end-systole are shown. Images reconstructed using different algorithms are shown in separate

columns. Difference magnitude and phase images of the phantom computed by subtracting the reconstructed images from the fully-sampled images are also shown. By visual observation, BLOSM-SENSE with joint encoding resulted in the minimum error. For the phase images, BLOSM-SENSE with joint encoding most closely recovered the phase information.

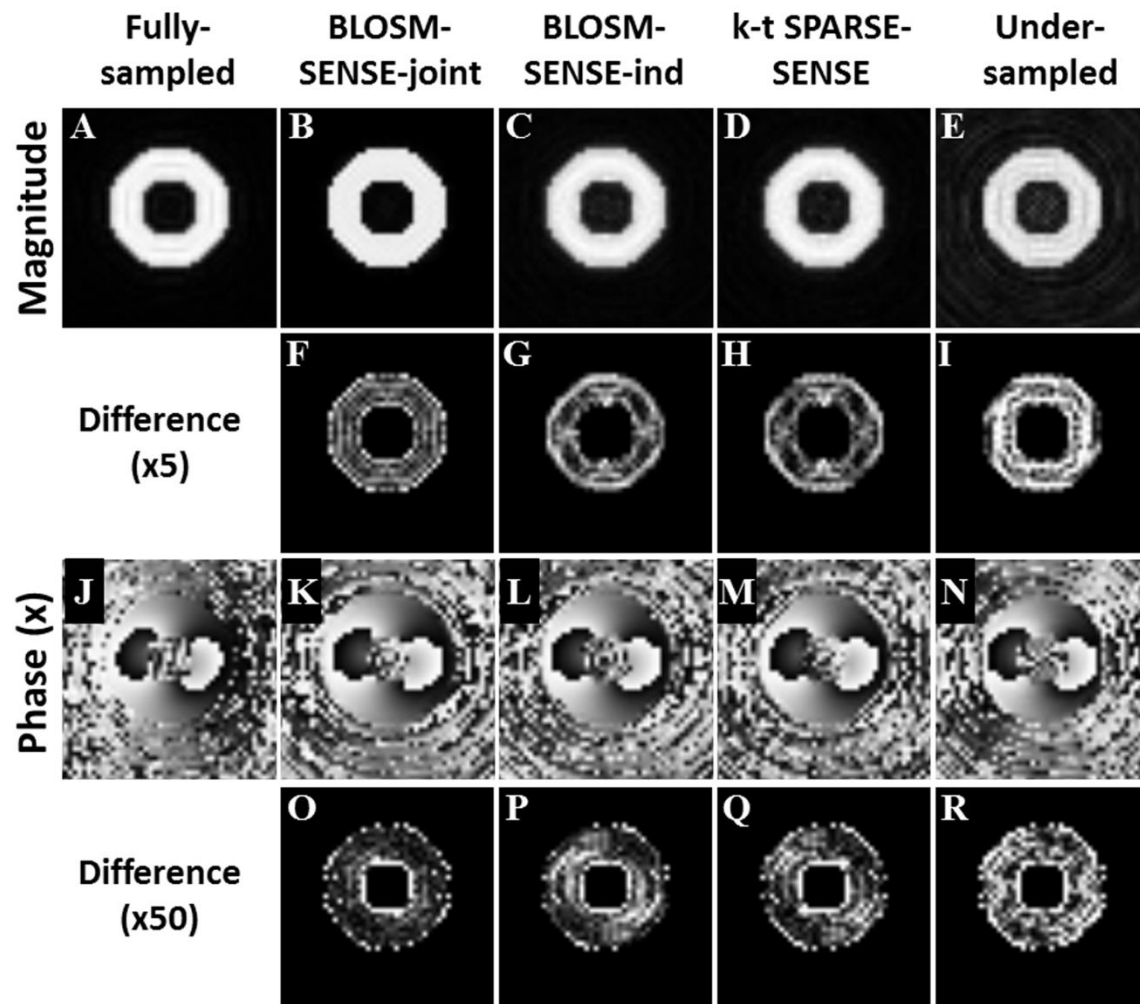


Figure 4.2 Example reconstructions of retrospectively rate-4 undersampled images from a computer simulated cardiac-contraction phantom. Magnitude (A-E) and phase (J-N) images with displacement encoding applied in the x direction at end-systole are shown. Fully-sampled data reconstructed with NUFFT (A,J) and accelerated data reconstructed using BLOSM-SENSE with joint encoding (B,K), BLOSM-SENSE with independent encoding (C,L), k-t SPARSE-SENSE (D,M) and zero-filled NUFFT (under-sampled) (E,N) are shown in different columns. Difference images (F-I,O-R) computed by subtracting reconstructed images from fully-sampled images are also shown (difference amplified by 5 and 50 times for magnitude and phase images, respectively, for display purposes). BLOSM-SENSE with joint encoding presented the smallest error and best agreement with the fully-sampled data.

Figure 4.3 shows RMSE analysis of the phantom studies for all the reconstruction algorithms at all acceleration rates. At an acceleration rate of 2, all algorithms perform similarly. When the acceleration rate was increased, BLOSM-SENSE with joint encoding showed advantages over the other methods. Furthermore, as shown in Figure 4.4, linear regression and Bland-Altman analysis of E_{cc} calculated from BLOSM-SENSE with joint encoding showed excellent agreement with the fully-sampled images at all acceleration rates (with greater errors at higher acceleration rates). Table 4.2 compares the Bland-Altman analyses for all of the different algorithms tested.

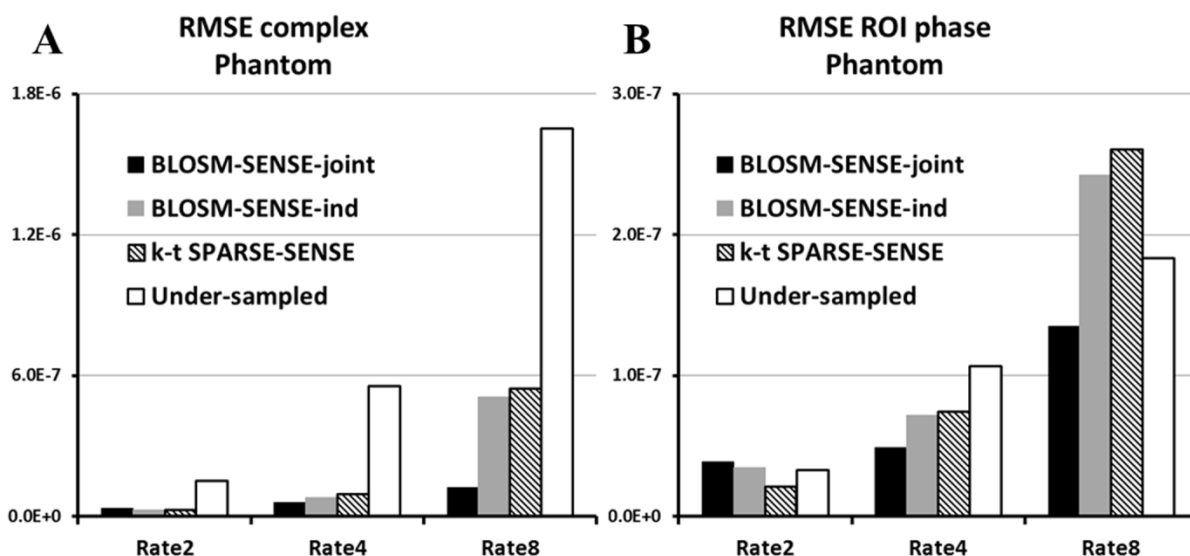


Figure 4.3 Root mean square error (RMSE) analysis of the performance of various reconstruction methods applied to a computer-simulated cardiac-contraction phantom at different undersampling rates. RMSE of the complex-valued images is shown in (A). Regional RMSE over the myocardium of the phase images was calculated and shown in (B). At the lower acceleration rate of 2, all CS-based algorithms performed similarly and showed lower complex RMSE compared to the zero-filled NUFFT reconstruction (Under-sampled). At higher acceleration rates of 4 and 8, BLOSM-SENSE with joint encoding showed advantages over the other methods using both complex and phase data.

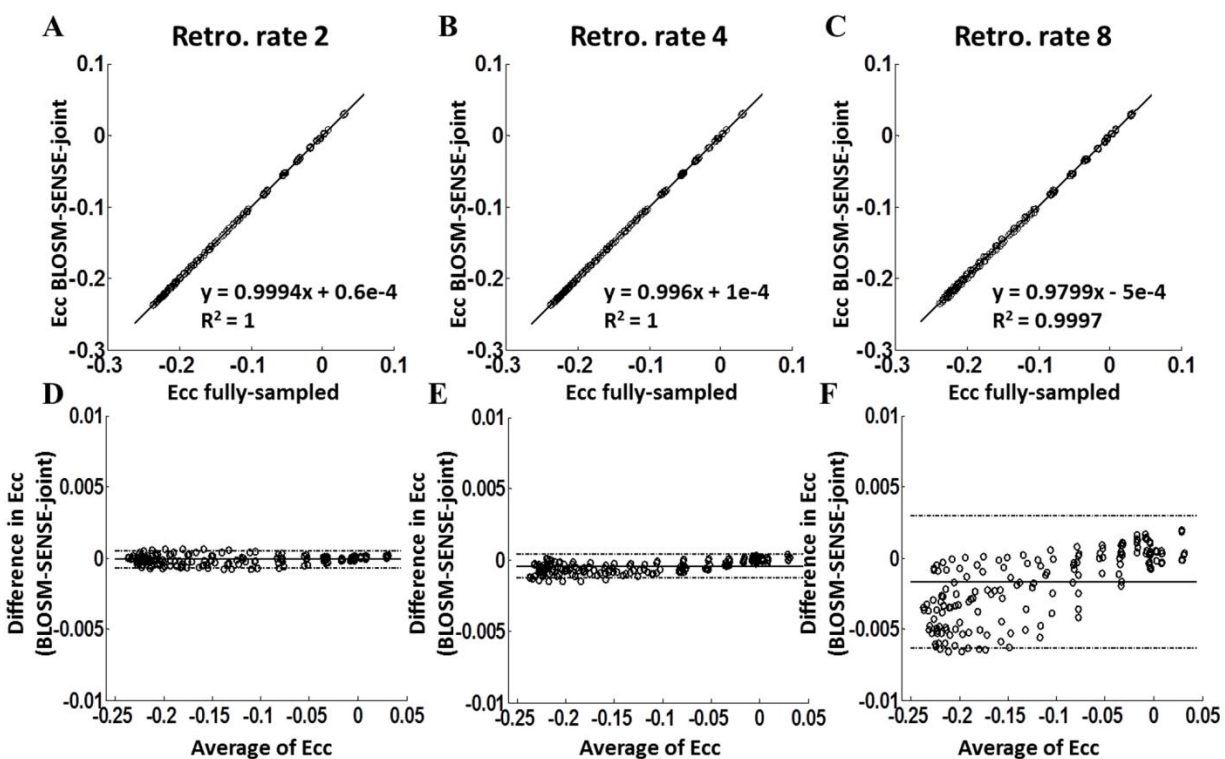


Figure 4.4 Linear regression (A-C) and Bland-Altman analysis (D-E) of Ecc calculated from BLOSM-SENSE with joint encoding compared to fully-sampled reconstructions for computer-simulated phantoms. Results from retrospectively rate-2, rate-4 and rate-8 are shown. Excellent agreement was achieved at all acceleration rates. Note that the y-axis range on the Bland-Altman graphs are much smaller than the Ecc range.

Table 4.2 Bland-Altman and linear regression results from phantoms studies for different reconstruction algorithms and acceleration rates.

Acc. Rate	Algorithm	Mean E_{cc} (1e-3)	Mean $E_{cc}-E_{cc_ref}$ (1e-3)	StdDev. $E_{cc}-E_{cc_ref}$ (1e-3)	R^2
2	BLOSM-SENSE-joint	-108.5	-0.11	0.30	1
	BLOSM-SENSE-ind	-108.5	-0.12	0.33	1
	k-t SPARSE-SENSE	-108.5	-0.20	0.36	1
4	BLOSM-SENSE-joint	-108.7	-0.42	0.43	1
	BLOSM-SENSE-ind	-108.4	-1.1	0.94	1
	k-t SPARSE-SENSE	-108.5	-0.89	0.98	1
8	BLOSM-SENSE-joint	-108.2	-1.7	2.4	0.99
	BLOSM-SENSE-ind	-107.8	-2.4	3.6	0.99
	k-t SPARSE-SENSE	-108.1	-1.9	3.7	0.99

4.3.2 Evaluation of in vivo studies

Example magnitude and phase images (with displacement encoding applied in the x direction) from retrospectively and prospectively rate-4 accelerated volunteer scans are shown in Figure 4.5 Images reconstructed using different algorithms are shown in the various columns. By visual inspection, all CS-PI algorithms (BLOSM-SENSE with joint encoding, BLOSM-SENSE with independent encoding, and k-t SPARSE-SENSE) provided better quality than SENSE.

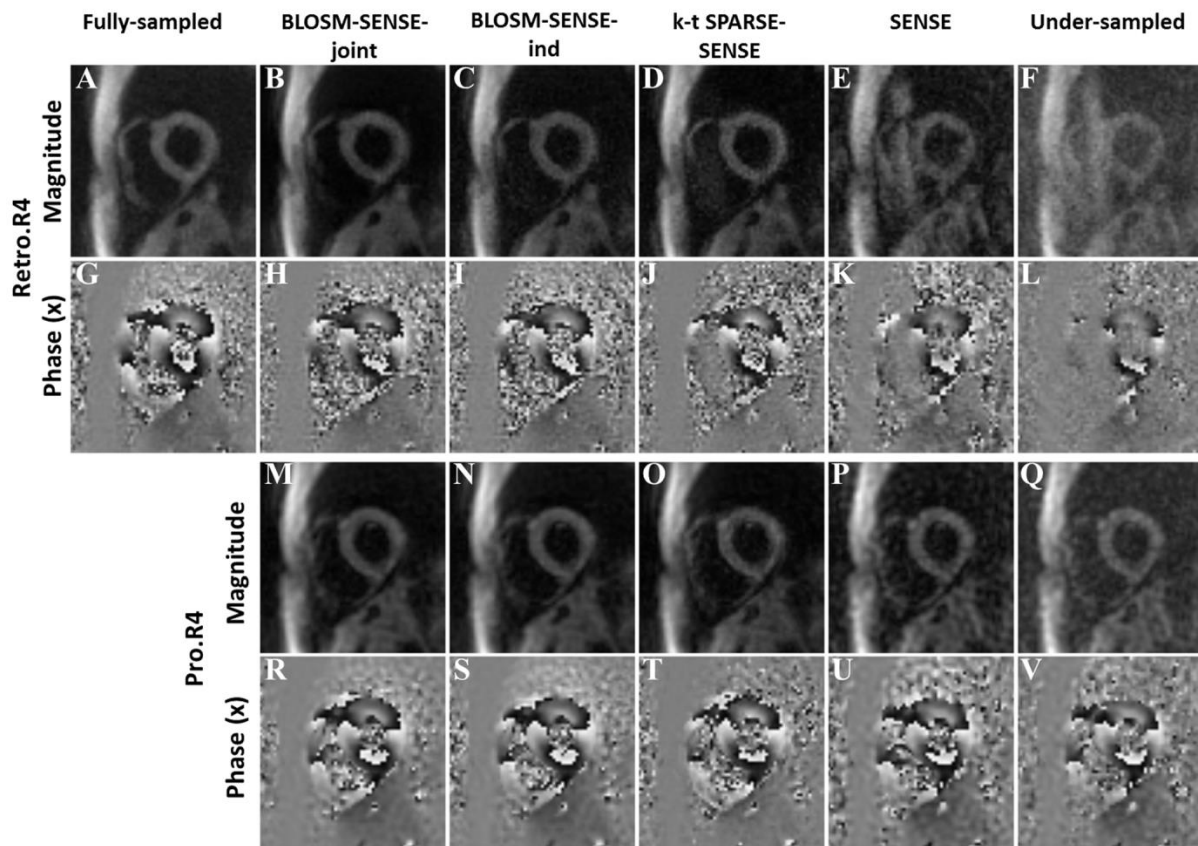


Figure 4.5 Example reconstructions of retrospectively rate-4 (A-L) and prospectively rate-4 (M-V) undersampled images from a healthy volunteer. Magnitude and phase images with displacement encoding applied in the x direction at end-systole are shown. Fully-sampled data reconstructed with NUFFT (A,G) and accelerated data reconstructed using BLOSM-SENSE with joint encoding (B,H,M,R), BLOSM-SENSE with independent encoding (C,I,N,S), k-t SPARSE-SENSE (D,J,O,T), SENSE (E,K,P,U) and zero-filled NUFFT-SOS-combined (under-sampled) (F,L,Q,V) methods are shown. All CS-PI combined methods achieved better image quality than SENSE.

Figure 4.6 shows the quantitative analyses for the in vivo studies. At an acceleration rate of 2, all algorithms achieved low RMSE, although the CS-PI methods gave higher SNR compared to the PI method. With an acceleration rate of 4, BLOSM-SENSE with joint encoding had the minimum error, which was statistically significant compared to the other algorithms

($p < 0.05$ ANOVA). BLOSM-SENSE with joint encoding also provided significantly higher SNR compared to other methods.

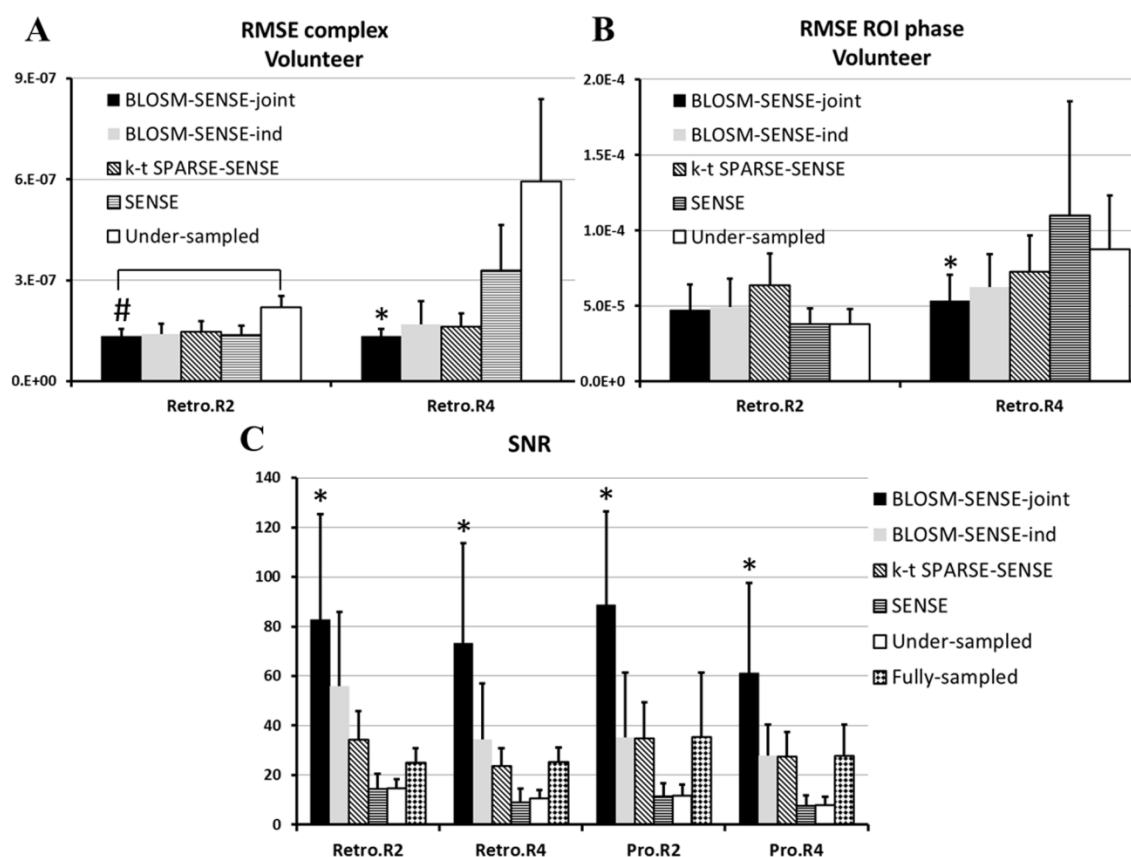


Figure 4.6 Quantitative analysis of the performance of various reconstruction methods applied to in vivo imaging of volunteers. Root mean square error (RMSE) and signal-to-noise ratio (SNR) are shown, with error bars indicating one standard deviation. (A) RMSE of the complex-valued images; (B) Regional RMSE over the myocardium of the phase images; (C) SNR values. At A low acceleration rate of 2, all methods offered similar RMSE, although CS-PI presented higher SNR. At a higher acceleration rate of 4, CS-PI showed improvement over SENSE. Specifically, BLOSM-SENSE with joint encoding showed significantly lower RMSE compared to the other methods at rate-4 acceleration for complex and phase data (* $P < 0.05$, ANOVA). For rate-2 acceleration, the lower RMSE of BLOSM-SENSE with joint encoding was statistically significant compared to the undersampled data reconstructed using SOS (# $P < 0.05$, ANOVA). BLOSM-SENSE with joint encoding showed significantly higher SNR compared to all other reconstruction methods (* $P < 0.05$, ANOVA).

Figure 4.7 shows linear regressions and Bland-Altman analyses of E_{cc} calculated from BLOSM-SENSE with joint encoding at different acceleration rates compared to the fully-

sampled data. Good correlations were found for both retrospectively and prospectively accelerated datasets. Table 4.3 summarizes the Bland-Altman and linear regression analyses for all the algorithms.

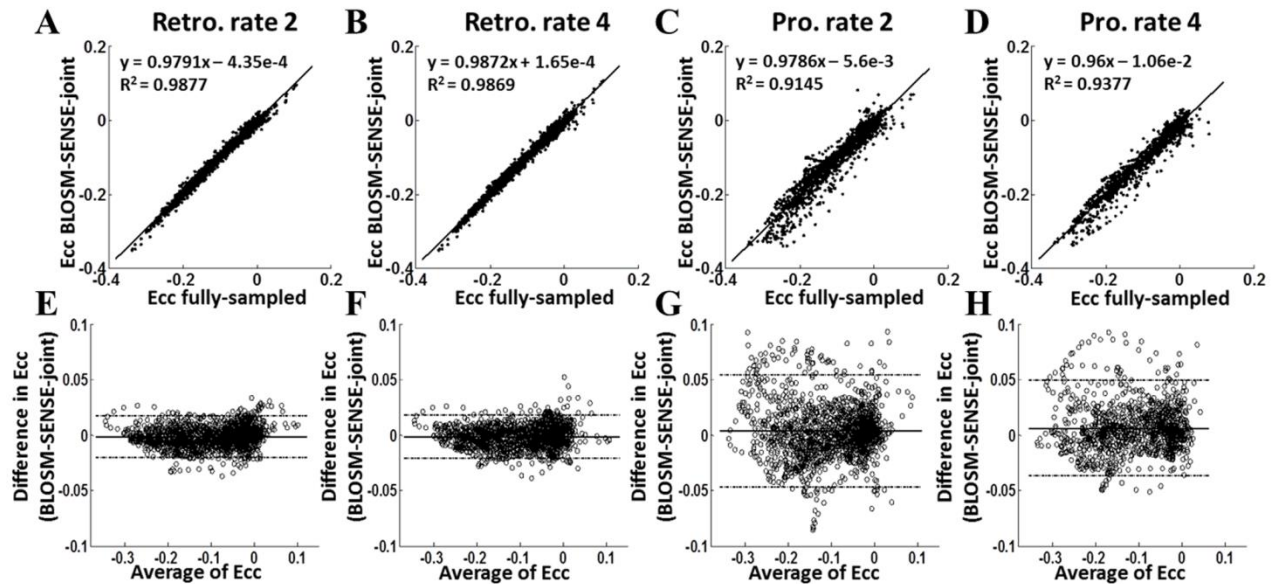


Figure 4.7 Linear regression (A-D) and Bland-Altman analysis (E-H) of Ecc using BLOSM-SENSE with joint encoding compared to fully-sampled reconstructions for in vivo imaging of volunteers. Results from retrospectively rate-2 (A,E) and rate-4 (B,F) and prospectively rate-2 (C,G) and rate-4 (D,H) are shown. Good agreement was achieved at all acceleration rates. Agreement was better for retrospectively undersampled data compared to prospectively accelerated data, likely due to differences in breathholding between different acquisitions.

Table 4.3 Bland-Altman and linear regression results from volunteers studies for different reconstruction algorithms and acceleration rates.

Acc. Rate	Algorithm	Mean E_{cc} (1e-3)	Mean $E_{cc}-E_{cc_ref}$ (1e-3)	StdDev. $E_{cc}-E_{cc_ref}$ (1e-3)	R²
Retro. 2	BLOSM-SENSE-joint	-98.7	-1.6	9.6	0.99
	BLOSM-SENSE-ind	-98	-2.9	11.4	0.98
	k-t SPARSE-SENSE	-97.8	-3.4	13.5	0.98
	SENSE	-98.8	-1.3	10	0.99
Retro. 4	BLOSM-SENSE-joint	-98.8	-1.4	9.8	0.99
	BLOSM-SENSE-ind	-97.8	-2.6	13.3	0.98
	k-t SPARSE-SENSE	-98.1	-2.7	15.0	0.97
	SENSE	-94.1	-10.7	35.8	0.84
Pro.2	BLOSM-SENSE-joint	-101.8	3.5	25.8	0.91
	BLOSM-SENSE-ind	-101.8	3.5	26.8	0.91
	k-t SPARSE-SENSE	-99.9	2.4	23.6	0.94
	SENSE	-101.5	3.0	22.5	0.93
Pro.4	BLOSM-SENSE-joint	-108.6	6.4	21.9	0.94
	BLOSM-SENSE-ind	-108.8	6.8	22.8	0.93
	k-t SPARSE-SENSE	-106.9	3.0	23.7	0.93
	SENSE	-108.3	5.8	21.5	0.94

4.4 DISCUSSION

In this study we developed an accelerated cine DENSE method utilizing variable density spiral k-space trajectories and golden angle rotations for data acquisition and CS-PI algorithms for image reconstruction. Studies using fully-sampled data with retrospective undersampling demonstrated low RMSE and high SNR of CS-PI-reconstructed images compared to fully-

sampled data. Prospectively undersampled scans at various acceleration rates demonstrated good image quality and high correlation of strain values with the reference data. These results demonstrate that acceleration methods can substantially reduce the scan time or increase temporal resolution for cine DENSE MRI compared to conventional protocols.

4.4.1 Comparison of different image reconstruction methods

In this study, using computer-generated and fully-sampled in vivo datasets, we retrospectively undersampled the raw data and compared the performance of BLOSM-SENSE with joint encoding, BLOSM-SENSE with independent encoding, k-t SPARSE-SENSE, and SENSE. While BLOSM-SENSE and k-t SPARSE-SENSE both apply CS to SENSE-combined data, BLOSM utilizes regional low-rank sparsity, whereas k-t SPARSE-SENSE exploits x-PCA sparsity throughout whole images. While the low-rank and x-PCA techniques both exploit spatiotemporal correlations using data driven basis functions, the regional approach (with motion tracking) used by BLOSM offered lower error and noise than the global approach of k-t SPARSE-SENSE. This finding is consistent with our previous results in the setting of first-pass perfusion imaging (78) as well as other recent publications adopting regional (26) and motion compensated approaches (86). Also, consistent with previous studies (15,75,76), CS-PI performed better than SENSE alone at acceleration rates greater than 2. At an acceleration rate of 2, SENSE offered good image quality and provided lower RMSE values than k-t SPARSE-SENSE. However, SENSE always had lowest SNR.

In cine DENSE, tissue displacement is encoded into the image phase, which is used to quantify myocardial motion and strain. At rate 4 acceleration, RMSE of complex-reconstructed images was significantly lower for BLOSM-SENSE with joint encoding compared to all other

methods. This result shows the advantage of BLOSM-SENSE with joint encoding for accurate quantification of cardiac function.

An integral part of strain analysis of cine DENSE images may involve the automatic propagation of endocardial and epicardial contours across cardiac phases using an algorithm called motion guided segmentation (MGS) (40). The performance of MGS depends on image quality. Among the 31 reconstructed datasets included in this study (including all datasets and all acceleration rates), we observed zero MGS failures for BLOSM-SENSE with joint encoding, 5 failures for BLOSM-SENSE with independent encoding, 10 failures for k-t SPARSE-SENSE, and 7 failures for SENSE.

Cine DENSE MRI is primarily used to quantify myocardial strain (36). For retrospectively undersampled data, BLOSM-SENSE with joint encoding provided the best correlation of E_{cc} compared to the fully-sampled data. The prospectively accelerated data showed worse agreement with the reference data, but this result is likely due to different respiratory positions at different acquisitions.

In this study, SNR measurements were used to provide a more comprehensive quality assessment than RMSE alone; however quantification of SNR for CS-PI reconstructions is difficult due to their inherent noise reduction properties and because SNR can vary spatially within images reconstructed using these methods. Accordingly, the SNR results should be interpreted carefully. Due to spatial variability, we were careful to use identically placed regions of interest for comparisons of different reconstruction algorithms. These results indicated that BLOSM-SENSE with joint encoding achieved the highest SNR, and this finding was consistent with the visual observations from Figure 5. Also, in the present study we observed that relative SNR values were dominated by differences in noise, not in signal.

4.4.2 Independent encoding vs. joint encoding

In this study, two different methods were explored for low-rank sparsity. The joint encoding method simultaneously processes cine DENSE data from multiple encoding directions while the independent encoding method calculated the sparsity separately for each encoding direction. The joint encoding sparsity method was inspired by previous work in k-t SPARSE-SENSE (76). The additional sparsity due to correlations between different encoding directions was exploited and provided lower reconstruction errors, higher SNR and more accurate strain assessments. The reconstruction time was also reduced by performing the reconstruction in a joint fashion. A benchmark test showed the times were 81 minutes and 157 minutes for BLOSM-SENSE with joint encoding and for BLOSM-SENSE with independent encoding, respectively, using identical in vivo data. In the future, the use of sampling randomness over different displacement encodings will be studied to potentially further promote sparsity along the displacement-encoding dimension.

4.4.3 Clinical implications

Using rate-4 acceleration, a common clinical cine DENSE protocol can be reduced from 28 heartbeats to 8 heartbeats. For clinical scanning, this represents a significant improvement in efficiency. To make fair comparisons in the present study, we held parameters such as readout duration and TR constant. However, acceleration can enable shorter readout duration and shorter TR, which in turn can reduce spiral blurring artifacts and provide increased temporal resolution. Reduced readout duration also has important implications regarding better spiral cine DENSE image quality at higher field strengths such as 3T, where off-resonance effects are greater. Thus,

acceleration of cine DENSE has broad implications for achieving shorter scan times, better temporal resolution, use at 3T, and subsequently higher SNR and/or spatial resolution. These technical innovations will likely directly lead to better cine DENSE imaging for patients with heart disease.

4.4.4 Accelerated 3D cine DENSE

With the imaging acceleration enabled by BLOSM, one next step of the study is to accelerate 3D cine DENSE. A 3D strain measurement can provide a complete assessment of the heart with regard to spatial coverage and a comprehensive evaluation of the strain tensor. The current navigator-gated 3D cine DENSE scan was approximately 25 minutes (38), which is too long for routine clinical use. In a preliminary study, we have extended the BLOSM technique to 3D imaging, where the dynamic 3D images were divided into small cubes and matrix low-rank sparsity was exploited inside these cubes to remove artifacts. The BLOSM-accelerated 3D cine DENSE imagings were performed on 6 healthy volunteers. With rate-6 acceleration, the averaged scan time was greatly shortened to 3.0 ± 1.4 minutes with navigation acceptance of $58 \pm 28\%$. Example reconstructed images from rate-6 prospectively-accelerated 3D DENSE data show high image quality in both magnitude and phase through the whole heart (Figure 4.8). The strain analysis obtained from the reconstructed images agreed well with historical strain values (35) (Figure 4.9). These preliminary results suggest that acceleration will make it feasible to routinely employ 3D cine DENSE for clinical comprehensive myocardial strain imaging with scan times of around 3 minutes.

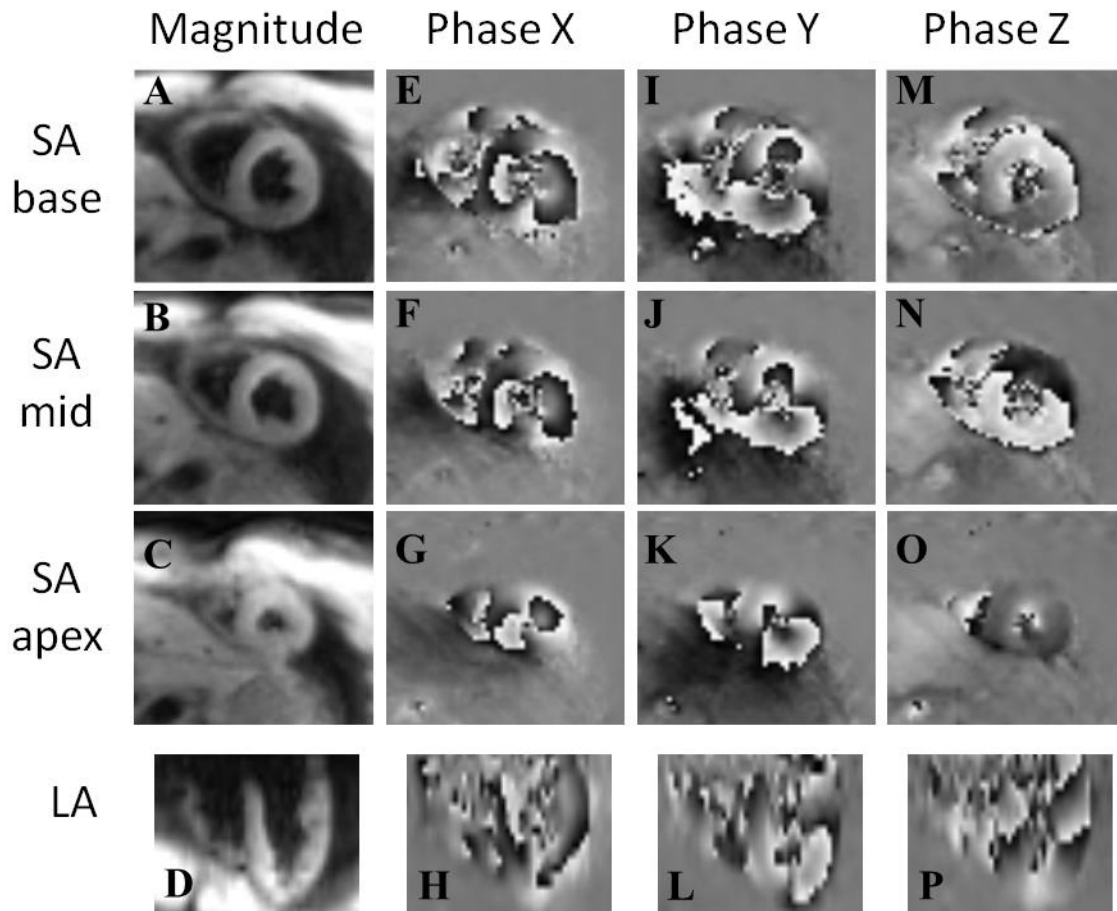


Figure 4.8 Example BLOSM-accelerated 3D cine DENSE images. Three short-axis (SA) views at base, mid and apex locations, along with one long-axis (LA) views are shown in different rows. The magnitude images (A-D) show clear delineation of the myocardium. All the phase images with displacement encodings in x (E-H), y (I-L) and z (M-P) show clear phase information that can be utilized for strain analysis.

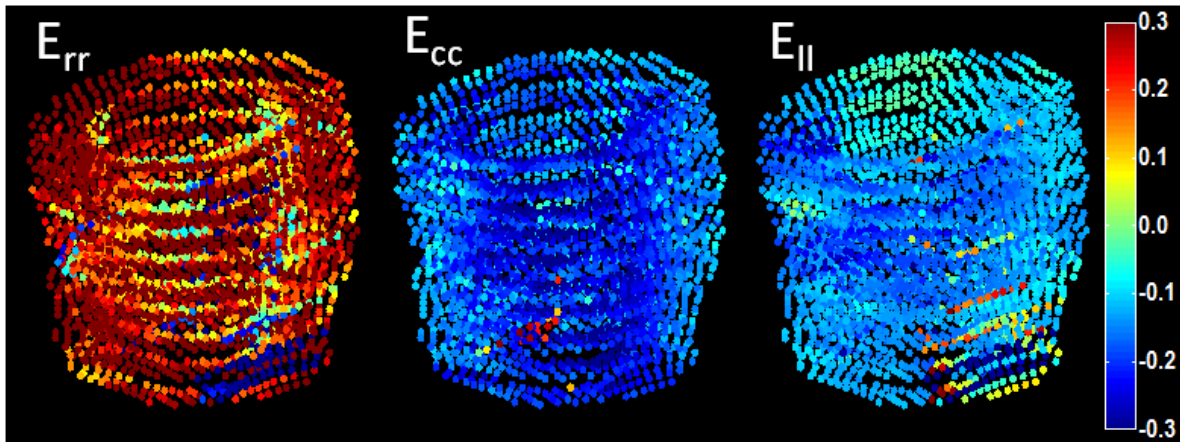


Figure 4.9 Example 3D voxel-wise strain maps of the LV at end systole. Radial (E_{rr}), circumferential (E_{cc}) and longitudinal strain (E_{ll}) maps show values in the range of normal subjects.

Chapter 5

Conclusions and Future Work

5.1 Conclusions

Compressed sensing, which enables high acquisition acceleration with little or no cost of image quality, has brought huge influences to the MRI field. However, the complex dynamics in CMR images bring up challenging tasks for CS. This dissertation developed a novel CS algorithm BLOSM that incorporates motion-compensation and regional sparsity together to handle the complex dynamics for broad types of CMR applications. Greatly improved image quality was achieved using BLOSM, comparing to other CS methods and fast imaging techniques.

BLOSM exploits low-rank sparsity within motion-compensated sub-regions of the whole images, which combines the advantages of current CS methods for dynamic CMR acceleration: regional sparsity, data-driven sparsity transform, and motion compensation. Careful implementation designs, such as the coarse-to-fine strategy and the block handling ensure the successful realization of the concepts.

The systematic validation studies of BLOSM using retrospectively accelerated first-pass cardiac perfusion images with prominent respiratory motions and computer simulated motion phantoms demonstrated that the two key concepts of BLOSM, namely regional sparsity and

motion-tracking, together contributes to the superior reconstruction quality over the existing CS methods.

Two CMR applications, first-pass perfusion and cine DENSE, both of which present extremely challenging tasks for CS reconstruction, were prospectively accelerated using BLOSM in this dissertation.

Prospectively accelerated first-pass perfusion imaging was performed in patients with suspected heart disease using BLOSM. The clinical data demonstrated true acceleration and the BLOSM offered large quality improvements over k-t SLR when respiratory motions were presented. 10 patients data supported the clinical use of rate 4 acceleration by BLOSM, which enables 2 mm^2 spatial resolution perfusion imaging with an acquisition window of 96 ms per slice. Retrospective study and 2 patients data suggested that higher accelerations can be achieved by BLOSM.

2D cine DENSE imaging was also accelerated by BLOSM. The scan time of 2D cine DENSE was greatly shortened from two separate breathholds of total 28 heartbeats to a single breathhold of 8 heartbeats. Both retrospective and prospective studies were conducted in healthy volunteers and BLOSM was demonstrated to provide better image quality than other fast imaging techniques and the cardiac function assessed from BLOSM reconstructed images matched closely with the fully-sampled reference data.

BLOSM is designed to be flexible and can include other fast imaging techniques for improvement. The BLOSM technique was extended to incorporate with parallel imaging technique SENSE to handle data acquired using phased-array multi-coil. This enabled BLOSM to exploit correlations among the RF coils. The BLOSM technique was also modified to handle non-Cartesian spiral trajectory, which offers more efficient k-space data collection. In a

preliminary study, BLOSM was extended to 3D and greatly shortened the scan time of 3D cine DENSE. These improvements have enabled BLOSM to broader types of CMR applications.

5.2 Future work

BLOSM can be improved and extended to achieve higher acceleration rates, better reconstruction quality and broader types of CMR applications. BLOSM can also be extended to combine with intra-frame motion correction technique. This could allow free-preparation CMR scanning.

Current clinical CMR imaging can benefit in various ways from the acceleration enabled by BLOSM. Applications such as cine SSFP imaging, myocardium parameter mapping with potential respiratory motions can be accelerated by BLOSM. BLOSM can also be utilized for small animal research studies.

Free-preparation CMR

In a “free-preparation” CMR scan, the patient preparation is minimized: no ECG leads are needed for cardiac contraction motion information, and patient can breathe freely without navigation pre-scan for respiratory motion information. The free-preparation can largely increase the MRI scan throughput and increase patient’s comfort. Imaging techniques for the free-preparation CMR should be able to achieve high acceleration rate to achieve high temporal resolution with desired spatial resolution, to capture all the cardiorespiratory dynamics. This high acceleration rate should be feasible at the presence of strong inter-image motion where the

motion occurs between two consecutive images. The technique should also be able to handle intra-image motion, where different parts of the k-space are acquired at different motion status.

The BLOSM method proposed in this study enables CS acceleration with inter-image motions, while the intra-image motion is ignored. To proceed towards a “free-preparation” CMR scan technique, intra-image motion correction step is needed in BLOSM, which is feasible with the design of BLOSM. Note that the inter-image motion correction is realized by adding motion-guidance/-compensation in the sparsity calculation term. The intra-image motion correction can then be realized separately by modifying the data fidelity term to correct the motion among different k-space data. To obtain the motion information, data can be combined with varying temporal acquisition window width and motion can be estimated using image-registration based method from pre-CS reconstructed images.

Higher order data correlations

To exploit data correlations, currently the dynamic data is rearranged into a 2D matrix with one dimension representing space and one dimension representing time. However, CMR data may present higher dimension structure. Example includes phase-encoding based method such as cine DENSE, where the data has extra dimension of different phase encodings in addition to the time and space. Another example is free-breathing CMR applications, where the data can be divided into different respiratory positions, thus an extra motion status dimension. Instead of blindly merging the high dimensional data into a 2D matrix for data correlation exploitation, a multi-dimension matrix with higher order data correlation exploitation may increase the sparsity level for higher acceleration rates and better CS reconstruction quality.

Basis functions

Currently, the spatiotemporal sparsity is exploited independently for each block and only the singular values are studied. However, correlations exist among blocks and these blocks share similar basis functions. Exploitation of these correlations can further improve the sparsity level and increase the image quality. One way to utilize the correlation is to combine the similar blocks together, such that the regions follow closely to the anatomical structure and region shape is beyond square blocks. Another way is to study the correlations among the basis functions and form over-complete dictionaries of the basis spatial, temporal or spatiotemporal basis functions. By studying the basis functions, not only the correlations among the regions can be exploited, but also some motion information can be extracted, which may aid or replace the image-registration step currently used in BLOSM for motion estimation.

2D first-pass CMR

With the acceleration enabled by BLOSM, first-pass cardiac perfusion imaging can achieve bigger spatial coverage at high spatial resolution. With rate 6 acceleration or higher, the acquisition window can be decreased to less than 64 ms with 2 mm spatial resolution. An interleaved multi-slice acquisition strategy may take full advantage of this reduced acquisition window and achieve more 2D slices to cover the whole heart. Fat saturation and outer-volume-suppression techniques that decrease the high signal from the chest wall, are preferred for clinical study for high acceleration rates and high number of RF coils.

High spatial resolution whole heart coverage of quantitative perfusion assessment may be of interest as well. The acceleration can also enable high spatial resolution perfusion imaging for stress perfusion studies, where acquisition window is small and motion problem is more severe.

2D cine DENSE

With the acceleration enabled by BLOSM, a complete 2D strain imaging can be performed within a short 8 heartbeat breathhold. Clinical studies on patients with heart disease are necessary to evaluate BLOSM's clinical performance.

Single-shot spiral cine DENSE with high temporal resolution is feasible. Studies evaluating cardiac dyssynchrony and mechanical activation time can benefit from this high temporal resolution. The acceleration may also support shorter readout time and enable 2D cine DENSE imaging on higher field scanner.

3D imaging

The BLOSM concept can be readily extended to 3D imaging, where instead of 2D blocks, 3D cubes can be motion-tracked through time to exploit spatiotemporal correlations. The 3D imaging can provide higher initial signal to noise ratio, which may allow higher acceleration rates.

The first-pass perfusion can benefit from an accelerated 3D imaging acquisition to cover the whole heart within one heartbeat. The 3D cine DENSE can also benefit from the acceleration to largely shorten the scan time from ~25 minutes to ~3 minutes.

Optimization parameter selection

The BLOSM, like any other CS method, is an optimization problem. The optimal optimization parameter is data dependent. It has been shown in this dissertation that the optimal parameter of BLOSM varies little within the same CMR application. However, careful parameter tuning is still necessary among different applications. This suggests that the parameter is mainly decided by the dynamic characteristics of the specific CMR application. Empirical parameter selection can largely decrease the time of the reconstruction setup.

Computation time

The focus of the current study is to improve the image quality of accelerated CMR imaging. However, computation time should also be improved for future clinical application. As reported in the first-pass perfusion study, most of the computation time was on the motion-estimation part. A more efficient motion estimation method can greatly decrease the computation time. A cost function convergence stopping criteria can also decrease the necessary iteration numbers and thus decrease the reconstruction time. And with better design of the code structure and adoption of parallel programming and graphic processing units (GPU), the computation time should be decreased to a clinical feasible time.

Appendix

Publications, Patents, Awards and Conference Abstracts

A.1 Journal Papers

- [1] **Chen X**, Salerno M, Yang Y, Epstein FH. Motion-compensated compressed sensing for dynamic contrast-enhanced MRI using regional spatiotemporal sparsity and region tracking: Block LOW-rank sparsity with motion-guidance (BLOSM). *Magn Reson Med* 2014;72(4):1028-38
- [2] Metha BB, **Chen X**, Bilchick K, Salerno M, Epstein FH. Accelerated and Navigator-Gated Look-Locker Imaging for Cardiac T1 Estimation (ANGIE): Development and Application to T1 mapping of the Right Ventricle. *Magn Reson Med* 2015;73(1):150-60
- [3] Naresh NK, **Chen X**, Roy R, Antkowiak P, Annex B, Epstein FH. Accelerated dual-contrast first-pass perfusion MRI of the mouse heart: development and application to diet-induced obese mice. *Magn Reson Med* 2014 (early view). Doi: 10.1002/mrm.25238
- [4] Ramachadran R, **Chen X**, Epstein FH, Bilchick KC. Singular value decomposition applied to cardiac Magnetic Resonance Imaging for selection of optimal cardiac resynchronization therapy candidates. *Radiology* 2014. (in press)

- [5] Qing K, Altes T, Tustison N, Feng X, **Chen X**, Mata J, Miller G, Tobias W, Cates G, Brookeman J, Mugler J. Rapid acquisition of Helium-3 and proton 3D image sets of the human lung in a single breath-hold using compressed sensing. Magn Reson Med 2014 (in press)

A.2 Patents

- [1] **Chen X**, Pan L. Compressed sensing using regional sparsity. US20130114872.
- [2] **Chen X**, Salerno M, Epstein FH. Systems and methods for accelerated dynamic magnetic resonance imaging. US 20140219531 A1
- [3] Epstein FH, **Chen X**, Yang Y, Salerno M, Meyer CH. Accelerated Cine DENSE using Variable Density Spirals and Compressed Sensing with Parallel Imaging. (application submitted)
- [4] Zhao L, **Chen X**, Fielden SW, Epstein FH, Mugler JP, Nicolas-Jilwan M, Wintermark M and Meyer CH. Systems and methods for accelerated arterial spin labeling using compressed sensing. US 20130315461 A1

A.3 Awards

- [1] American Heart Association Predoctoral Fellowship 12PRE12040059 (2012-2014) on Accelerating Cardiac MR with Intrinsically Motion-Guided Compressed Sensing.
- [2] 2014 ISMRM Young Investigator I.I.Rabi Award in Basic Science – semi finalist on Motion-compensated compressed sensing for dynamic contrast-enhanced MRI using

- regional spatiotemporal sparsity and region tracking: Block Low-rank Sparsity with Motion-guidance (BLOSM). First author.
- [3] Magna Merit Award of ISMRM 2014 on Accelerated first-pass perfusion MRI using BLOSM: Evaluation using dynamic simulations and patient datasets with prominent respiratory motion. First author.
- [4] 1st place in the Ninth-Annual University of Virginia Engineering Research Symposium (2013) on Accelerated Dynamic Cardiac Magnetic Resonance Imaging using Block Low-rank Sparsity with Motion guidance (BLOSM).
- [5] Huskey Graduate Research Exhibition at the University of Virginia 2nd place (2012) on Motion-guided compressed sensing to accelerate dynamic cardiac magnetic resonance imaging
- [6] Gold Award of the University of Virginia Department of Radiology Symposium 2010 on Accelerated MRI T1 mapping using compressed sensing.

A.4 Oral Presentations

- [1] **Chen X**, Salerno M, Kramer CM, Mehta BB, Yang Y, Shaw Peter, Epstein FH. Prospectively accelerated first-pass myocardial perfusion imaging in patients using motion-compensated compressed sensing exploiting regional low-rank sparsity. SCMR/EuroCMR Joint Scientific Sessions 2015. In press.
- [2] **Chen X**, Yang Y, Salerno M, and Epstein FH. Accelerated first-pass perfusion MRI using BLOSM: Evaluation using dynamic simulations and patient datasets with prominent respiratory motion. In Proceedings of ISMRM 2014:0880.

- [3] **Chen X**, Yang Y, Salerno M, Meyer, CH, and Epstein FH. Accelerated Cine DENSE MRI using Compressed Sensing and Parallel Imaging. J Cardio Mag Reson 2014, 16(Suppl 1):W16.
- [4] **Chen X**, Salerno M, Meyer CH, and Epstein FH. Accelerated dynamic MRI using Block LOw-rank Sparsity with Motion guidance (BLOSM). In Proceedings of ISMRM Scientific Workshop 2013 on Data Sampling.
- [5] Auger DA, Cui X, **Chen X**, Bilchick KC, Epstein FH. Cardiac Mechanical Activation Mapping in Heart Failure Patients with Left Bundle Branch Block using Cine DENSE MRI. SCMR/EuroCMR Joint Scientific Sessions 2015. In press.
- [6] Naresh NK, **Chen X**, Roy RJ, Annex BH, Epstein FH. Multiparametric MRI detects early biomarkers of diabetic cardiomyopathy in C57BI/6 mice fed a high-fat diet. AHA 2014.
- [7] Auger D, Cui Sophia, **Chen X**, Bilchick K, and Epstein F. Magnetic Resonance Imaging of Cardiac Activation in Heart Failure Patients with Left Bundle Branch Block. In Proceeding of BMES 2014.
- [8] Yang Y, **Chen X**, Epstein FH, Meyer CH, Kramer CM, and Salerno M. 3D whole-heart quantitative first-pass perfusion imaging with a stack-of spirals trajectory. In Proceedings of ISMRM 2014:0878.
- [9] Naresh NK, **Chen X**, Roy RJ, Annex BH, and Epstein FH. Cardiac MR Detects Impaired Myocardial Perfusion Reserve and Left-ventricular Hypertrophy in C57BI/6 Mice Fed a High-Fat Diet. J Cardio Mag Reson 2014,16(Suppl 1):O87. Regional scholarship awards.

- [10] Yang Y, **Chen X**, Epstein FH, Meyer CH, Kuruvilla S, Kramer CM, and Salerno M. Motion-corrected compressed-sensing enables robust spiral first-pass perfusion imaging with whole heart coverage. *J Cardio Mag Reson* 2014,16(Suppl 1):O81.
- [11] Zhao L, **Chen X**, Fielden SW, Mugler III JP, Pfeuffer J, Nicolas-Jilwan M, Wintermark M and Meyer CH. Accurate accelerated dynamic PCASL with 3D spiral, parallel imaging and compressed sensing. In *Proceedings of ISMRM Scientific Workshop 2013 on Data Sampling*.

A.5 Other Conference Abstracts

- [1] **Chen X**, Yang Y, Salerno M, Meyer CH, and Epstein FH. Accelerated Cine DENSE using Variable Density Spirals and Compressed Sensing with Parallel Imaging. In *Proceedings of ISMRM 2014*:3892.
- [2] **Chen X**, Mehta BB, Salerno M, and Epstein FH. High resolution myocardial T1 mapping using MOLLI with parallel imaging and compressed sensing. In *Proceedings of ISMRM 2013*:1407.
- [3] **Chen X**, Salerno M, Meyer CH, and Epstein FH. Block LOW-rank Sparsity with Motion guidance (BLOSM) for accelerated dynamic MRI. In *Proceedings of ISMRM 2013*:4555.
- [4] **Chen X**, Salerno M, and Epstein FH. Accelerated first-pass perfusion CMR using compressed sensing with regional spatiotemporal sparsity. *J Cardio Mag Reson* 2013, 15(Suppl 1):E16.

- [5] **Chen X**, Salerno M, Antkowiak PF, and Epstein FH. Motion-Guided Temporally-Constrained Compressed Sensing for Dynamic MRI. In Proceedings of ISMRM 2012:1230.
- [6] **Chen X**, Vij K, and Pan L. Online real-time imaging using compressed sensing in interventional MRI. In Proceedings of iMRI 2012.
- [7] **Chen X**, Salerno M, Epstein FH, and Meyer CH. Accelerated Multi-TI Spiral MRI using Compressed Sensing with Temporal Constraints. In Proceedings of ISMRM 2011:4369.
- [8] **Chen X**, Young A, and Epstein FH. Cine DENSE MRI with Dual Displacement Encoding. In Proceedings of ISMRM 2010:3570.
- [9] **Chen X**, Zhong X, and Epstein FH. MRI of Longitudinal Myocardial Strain using Multislice Cine DENSE with Through-plane Displacement Encoding. In Proceedings of ISMRM 2010:3564.
- [10] Naresh NK, Butcher JT, **Chen X**, Annex BH, Isakson BE, Epstein FH. Cardiac MR Detects the Progression of Impaired Myocardial Perfusion Reserve in a Mouse Model of Obesity-Related Cardiomyopathy. SCMR/EuroCMR Joint Scientific Sessions 2015. In press.
- [11] Auger D, Cui Sophia, **Chen X**, Bilchick K, and Epstein F. CMR mapping of mechanical activation time in patients with heart failure and left bundle branch block: methods and initial results. AHA 2014?
- [12] Mehta B, Bilchick KC, **Chen X**, Salerno M, and Epstein FH. Right ventricular myocardial T1 and extracellular volume fraction (ECV) measurements using high resolution ANGLE T1 mapping. In Proceedings of ISMRM 2014:3970.

- [13] Naresh NK, **Chen X**, Antkowiak PF, Roy RJ, and Epstein FH. First-pass MRI detects reduced myocardial perfusion reserve in ApoE^{-/-} mice on a high-cholesterol diet. In Proceedings of ISMRM 2013:5812.
- [14] Zhao L, **Chen X**, Fielden SW, Mugler III JP, Pfeuffer J, Nicolas-Jilwan M, Wintermark M, and Meyer CH. Accelerated 3DPCASL using compressed sensing. In Proceedings of ISMRM 2013:2157.
- [15] Naresh NK, **Chen X**, Antkowiak P, Xu Y, French BA, and Epstein FH. Accelerated dual-contrast quantitative first-pass perfusion MRI of the mouse heart with compressed sensing. J Cardio Mag Reson 2013, 15(Suppl 1): W17
- [16] Ramachandran R, **Chen X**, Mehta BB, Bilchick KC, and Epstein FH. Principle component analysis of myocardial strain to quantify left ventricular dyssynchrony. J Cardio Mag Reson 2013, 15(Suppl 1): P74
- [17] Naresh NK, **Chen X**, Antkowiak PF, Eptesin FH. Quantitative first-pass perfusion MRI of the mouse heart: data acquisition, reconstruction, and analysis strategies. J Nuclear Med 2012;53(4):669-70.
- [18] Yang Y, **Chen X**, Feng X, Wang M, Epstein FH, Meyer CH, and Salerno M. Evaluation of Parallel Reconstruction Techniques for First-pass Perfusion Imaging Using Spiral Trajectories. In Proceedings of ISMRM 2012:3956.
- [19] Zhao L, **Chen X**, Fielden SW, Epstein FH, Mugler III JP, Pfeuffer J, Nicolas-Jilwan M, Wintermark M and Meyer CH. Accelerated kinetic ASL using 3D spiral TSE and compressed sensing. In Proceedings of ISMRM 2012:1997.

- [20] Yan M, Johnson J, **Chen X**, Chang TC, Chen Y, and Fang T. Evaluation of compressed sensing MR reconstruction quality using signed just notification difference (JND) analysis. In Proceedings of ISMRM 2012:4223.
- [21] Epstein FH, Naresh NK, Antkowiak PF, Vandsburger MH, and **Chen X**. Quantitative MRI of the myocardial microcirculation in mice using FAIR Look-Locker arterial spin labeling and a gamma-variate model of blood transit time distribution. In Proceedings of ISMRM 2011:216.

References

1. Earls JP, Ho VB, Foo TK, Castillo E, Flamm SD. Cardiac MRI: Recent progress and continued challenges. *J Magn Reson Imaging* 2002;16(2):111-127.
2. West AM, Kramer CM. Cardiovascular Magnetic Resonance Imaging of Myocardial Infarction, Viability, and Cardiomyopathies. *Curr Prob Cardiology* 2010;35(4):176-220.
3. Epstein FH. MRI of left ventricular function. *Journal of nuclear cardiology : official publication of the American Society of Nuclear Cardiology* 2007;14(5):729-744.
4. McGibney G, Smith MR, Nichols ST, Crawley A. Quantitative evaluation of several partial Fourier reconstruction algorithms used in MRI. *Magnetic resonance in medicine : official journal of the Society of Magnetic Resonance in Medicine / Society of Magnetic Resonance in Medicine* 1993;30(1):51-59.
5. Madore B, Glover GH, Pelc NJ. Unaliasing by fourier-encoding the overlaps using the temporal dimension (UNFOLD), applied to cardiac imaging and fMRI. *Magn Reson Med* 1999;42(5):813-828.
6. Jones RA, Haraldseth O, Muller TB, Rinck PA, Oksendal AN. K-space substitution: a novel dynamic imaging technique. *Magn Reson Med* 1993;29(6):830-834.
7. Pruessmann KP, Weiger M, Scheidegger MB, Boesiger P. SENSE: Sensitivity encoding for fast MRI. *Magnetic Resonance in Medicine* 1999;42(5):952-962.
8. Griswold MA, Jakob PM, Heidemann RM, Nittka M, Jellus V, Wang JM, Kiefer B, Haase A. Generalized Autocalibrating Partially Parallel Acquisitions (GRAPPA). *Magnetic Resonance in Medicine* 2002;47(6):1202-1210.

9. Donoho DL. Compressed sensing. *Ieee T Inform Theory* 2006;52(4):1289-1306.
10. Lustig M, Donoho D, Pauly JM. Sparse MRI: The application of compressed sensing for rapid MR imaging. *Magnetic Resonance in Medicine* 2007;58(6):1182-1195.
11. Candès EJ, Romberg J, Tao T. Robust uncertainty principles: Exact signal reconstruction from highly incomplete frequency information. *Information Theory, IEEE Transactions on* 2006;52(2):489-509.
12. Lustig M, Santos JM, Donoho D, Pauly JM. k-t SPARSE: high frame rate dynamic MRI exploiting spatio-temporal sparsity. *Proceedings of ISMRM, Seattle* 2006:2420.
13. Chen X, Salerno M, Epstein FH, Meyer CH. Accelerated Multi-TI Spiral MRI using Compressed Sensing with Temporal Constraints. *Proceedings of 19th Annual Meeting of ISMRM* 2011:4369.
14. Velikina JV, Johnson KM, Block WF, Samsonov A. Design of Temporally constrained compressed sensing methods for accelerated dynamic MRI. *Proceedings of 18th Annual Meeting of ISMRM* 2010:4865.
15. Otazo R, Kim D, Axel L, Sodickson DK. Combination of compressed sensing and parallel imaging for highly accelerated first-pass cardiac perfusion MRI. *Magnetic Resonance in Medicine* 2010;64(3):767-776.
16. Jung H, Sung K, Nayak KS, Kim EY, Ye JC. k-t FOCUSS: A General Compressed Sensing Framework for High Resolution Dynamic MRI. *Magnetic Resonance in Medicine* 2009;61(1):103-116.
17. Zhao B, Haldar JP, Liang ZP. PSF model-based reconstruction with sparsity constraint: algorithm and application to real-time cardiac MRI. *Conf Proc IEEE Eng Med Biol Soc* 2010;2010:3390-3393.

18. Knobloch V, Boesiger P, Kozerke S. Sparsity transform k-t principal component analysis for accelerating cine three-dimensional flow measurements. *Magn Reson Med* 2012.
19. Lingala SG, Hu Y, DiBella E, Jacob M. Accelerated Dynamic MRI Exploiting Sparsity and Low-Rank Structure: k-t SLR. *Ieee T Med Imaging* 2011;30(5):1042-1054.
20. Chen X, Salerno M, Antkowiak PF, Epstein FH. Motion-Guided Temporally-Constrained Compressed sensing for Dynamic MRI. *Proceedings of ISMRM 2012*:1230.
21. Lingala SG, Nadar M, Ched'hotel C, Zhang L, Jacob M. Unified reconstruction and motion estimation in cardiac perfusion MRI. *proceedings of IEEE 2011* 2011:65 - 68.
22. Asif MS, Hamilton L, Brummer M, Romberg J. Motion-adaptive spatio-temporal regularization for accelerated dynamic MRI. *Magn Reson Med* 2012.
23. Usman M, Atkinson D, Odille F, Kolbitsch C, Vaillant G, Schaeffter T, Batchelor PG, Prieto C. Motion corrected compressed sensing for free-breathing dynamic cardiac MRI. *Magn Reson Med* 2012.
24. Akcakaya M, Basha TA, Goddu B, Goepfert LA, Kissinger KV, Tarokh V, Manning WJ, Nezafat R. Low-dimensional-structure self-learning and thresholding: regularization beyond compressed sensing for MRI reconstruction. *Magnetic Resonance in Medicine* 2011;66(3):756-767.
25. Vitanis V, Manka R, Giese D, Pedersen H, Plein S, Boesiger P, Kozerke S. High Resolution Three-Dimensional Cardiac Perfusion Imaging Using Compartment-Based k-t Principal Component Analysis. *Magnetic Resonance in Medicine* 2011;65(2):575-587.
26. Akcakaya M, Basha TA, Pflugi S, Foppa M, Kissinger KV, Hauser TH, Nezafat R. Localized spatio-temporal constraints for accelerated CMR perfusion. *Magn Reson Med* 2013.

27. Salerno M, Beller GA. Noninvasive Assessment of Myocardial Perfusion. *Circ Cardiovasc Imag* 2009;2(5):412-424.
28. Gerber BL, Raman SV, Nayak K, Epstein FH, Ferreira P, Axel L, Kraitchman DL. Myocardial first-pass perfusion cardiovascular magnetic resonance: history, theory, and current state of the art. *J Cardiovasc Magn R* 2008;10.
29. Kellman P, Arai AE. Imaging sequences for first pass perfusion - A review. *J Cardiovasc Magn R* 2007;9(3):525-537.
30. Jerosch-Herold M, Seethamraju RT, Swingen CM, Wilke NM, Stillman AE. Analysis of myocardial perfusion MRI. *J Magn Reson Imaging* 2004;19(6):758-770.
31. Salerno M, Sica C, Kramer CM, Meyer CH. Improved first-pass spiral myocardial perfusion imaging with variable density trajectories. *Magn Reson Med* 2013;70(5):1369-1379.
32. Gorcsan Jr, Tanaka H. Echocardiographic assessment of myocardial strain. *J Am Coll Cardiol* 2011;58(14):1401-1413.
33. Geyer H, Caracciolo G, Abe H, Wilansky S, Carerj S, Gentile F, Nesser H-J, Khandheria B, Narula J, Sengupta PP. Assessment of myocardial mechanics using speckle tracking echocardiography: fundamentals and clinical applications. *J Am Soc Echocardiogr* 2010;23(4):351-369; quiz 453-355.
34. Shehata ML, Cheng S, Osman NF, Bluemke DA, Lima JA. Myocardial tissue tagging with cardiovascular magnetic resonance. *Journal of cardiovascular magnetic resonance : official journal of the Society for Cardiovascular Magnetic Resonance* 2009;11:55.
35. Simpson RM, Keegan J, Firmin DN. MR assessment of regional myocardial mechanics. *J Magn Reson Imaging* 2013;37(3):576-599.

36. Kim D, Gilson WD, Kramer CM, Epstein FH. Myocardial tissue tracking with two-dimensional cine displacement-encoded MR imaging: development and initial evaluation. *Radiology* 2004;230(3):862-871.
37. Zhong X, Spottiswoode BS, Meyer CH, Epstein FH. Two-dimensional Spiral Cine DENSE. *Proceedings of the 15th Annual Meeting of ISMRM 2007*:756.
38. Zhong XD, Spottiswoode BS, Meyer CH, Kramer CM, Epstein FH. Imaging Three-Dimensional Myocardial Mechanics Using Navigator-Gated Volumetric Spiral Cine DENSE MRI. *Magnetic Resonance in Medicine* 2010;64(4):1089-1097.
39. Young AA, Li B, Kirton RS, Cowan BR. Generalized spatiotemporal myocardial strain analysis for DENSE and SPAMM imaging. *Magnetic Resonance in Medicine* 2012;67(6):1590-1599.
40. Spottiswoode BS, Zhong X, Lorenz CH, Mayosi BM, Meintjes EM, Epstein FH. Motion-guided segmentation for cine DENSE MRI. *Med Image Anal* 2009;13(1):105-115.
41. Gilliam AD, Epstein FH. Automated motion estimation for 2-D cine DENSE MRI. *IEEE Trans Med Imaging* 2012;31(9):1669-1681.
42. Bilchick KC, Kuruvilla S, Hamirani YS, Ramachandran R, Clarke SA, Parker KM, Stukenborg GJ, Mason P, Ferguson JD, Moorman JR, Malhotra R, Mangrum JM, Darby AE, Dimarco J, Holmes JW, Salerno M, Kramer CM, Epstein FH. Impact of mechanical activation, scar, and electrical timing on cardiac resynchronization therapy response and clinical outcomes. *J Am Coll Cardiol* 2014;63(16):1657-1666.
43. Kim D, Kellman P. Improved cine displacement-encoded MRI using balanced steady-state free precession and time-adaptive sensitivity encoding parallel imaging at 3 T. *Nmr Biomed* 2007;20(6):591-601.

44. Gamper U, Boesiger P, Kozerke S. Compressed sensing in dynamic MRI. *Magnetic Resonance in Medicine* 2008;59(2):365-373.
45. Adluru G, Awate SP, Tasdizen T, Whitaker RT, Dibella EV. Temporally constrained reconstruction of dynamic cardiac perfusion MRI. *Magnetic Resonance in Medicine* 2007;57(6):1027-1036.
46. Lingala S, DiBella E, Ched'hotel C, Nadar M, Jacob M. Motion compensated reconstruction for myocardial perfusion MRI. *J Cardiovasc Magn R* 2012;14(Suppl 1):M11.
47. Adluru G, DiBella E. A comparison of L1 and L2 norms as temporal constraints for reconstruction of undersampled dynamic contrast enhanced cardiac scans with respiratory motion. *Proceedings of ISMRM* 2008:340.
48. Hansen MS, Sorensen TS, Arai AE, Kellman P. Retrospective reconstruction of high temporal resolution cine images from real-time MRI using iterative motion correction. *Magn Reson Med* 2012;68(3):741-750.
49. Batchelor PG, Atkinson D, Irarrazaval P, Hill DLG, Hajnal J, Larkman D. Matrix description of general motion correction applied to multishot images. *Magnetic Resonance in Medicine* 2005;54(5):1273-1280.
50. Chen X, Salerno M, Meyer CH, Epstein FH. Block LOW-Rank Sparsity with Motion guidance (BLOSM) for Accelerated Dynamic MRI. *Proceedings of ISMRM* 2013:4555.
51. Bergen JR, Anandan P, Hanna KJ, Hingorani R. Hierarchical Model-Based Motion Estimation. *Lecture Notes in Computer Science* 1992;588:237-252.
52. Makela T, Clarysse P, Sipila O, Pauna N, Pham QC, Katila T, Magnin IE. A review of cardiac image registration methods. *Ieee T Med Imaging* 2002;21(9):1011-1021.

53. Dufaux F, Moscheni F. Motion Estimation Techniques for Digital Tv - a Review and a New Contribution. *P Ieee* 1995;83(6):858-876.
54. Montoliu R, Pla F. Robust techniques in least squares-based motion estimation problems. *Progress in Pattern Recognition, Speech and Image Analysis* 2003;2905:62-70.
55. Zitova B, Flusser J. Image registration methods: a survey. *Image Vision Comput* 2003;21(11):977-1000.
56. Avants BB, Tustison NJ, Song G, Cook PA, Klein A, Gee JC. A reproducible evaluation of ANTs similarity metric performance in brain image registration. *Neuroimage* 2011;54(3):2033-2044.
57. Nicholas J, Tustison BBA. Diffeomorphic Directly Manipulated Free-Form Deformation Image Registration via Vector Fields Flows. *Proceedings of the Fifth Workshop on Biomedical Image Registration* 2012;7359:31-39.
58. Thevenaz P, Blu T, Unser M. Interpolation revisited. *Ieee T Med Imaging* 2000;19(7):739-758.
59. Zhao B, Haldar JP, Brinegar C, Liang ZP. Low rank matrix recovery for real-time cardiac MRI. *proceedings of IEEE 2010* 2010:996 - 999.
60. Liang ZP. Spatiotemporal imaging with partially separable functions. *ISBI 2007*:988 - 991.
61. Zhao B, Haldar JP, Christodoulou AG, Liang ZP. Image Reconstruction From Highly Undersampled (k, t)-Space Data With Joint Partial Separability and Sparsity Constraints. *Ieee T Med Imaging* 2012;31(9):1809-1820.
62. Akcakaya M, Basha TA, Chan RH, Rayatzadeh H, Kissinger KV, Goddu B, Goepfert LA, Manning WJ, Nezafat R. Accelerated contrast-enhanced whole-heart coronary MRI

- using low-dimensional-structure self-learning and thresholding. *Magnetic Resonance in Medicine* 2012;67(5):1434-1443.
63. Dillencourt MB, Samet H, Tamminen M. A General-Approach to Connected-Component Labeling for Arbitrary Image Representations. *J Acm* 1992;39(2):253-280.
 64. Majumdar A, Ward RK. An algorithm for sparse MRI reconstruction by Schatten p-norm minimization. *Magnetic resonance imaging* 2011;29(3):408-417.
 65. Combettes PL, Wajs VR. Signal recovery by proximal forward-backward splitting. *Multiscale Model Sim* 2005;4(4):1168-1200.
 66. Dabov K, Foi A, Katkovnik V, Egiazarian K. Image denoising by sparse 3-D transform-domain collaborative filtering. *IEEE Trans Image Process* 2007;16(8):2080-2095.
 67. Jung H. k-t FOCUSS.
 68. Aletras AH, Ding S, Balaban RS, Wen H. DENSE: displacement encoding with stimulated echoes in cardiac functional MRI. *J Magn Reson* 1999;137(1):247-252.
 69. Petzschner FH, Ponce IP, Blaimer M, Jakob PM, Breuer FA. Fast MR Parameter Mapping Using k-t Principal Component Analysis. *Magnetic Resonance in Medicine* 2011;66(3):706-716.
 70. Wang Z, Bovik AC, Sheikh HR, Simoncelli EP. Image quality assessment: From error visibility to structural similarity. *Ieee T Image Process* 2004;13(4):600-612.
 71. Brinegar C, Zhang H, Wu YJ, Foley LM, Hitchens T, Ye Q, Ho C, Liang ZP. First-pass perfusion cardiac MRI using the Partially Separable Functions model with generalized support. *Conf Proc IEEE Eng Med Biol Soc* 2010;2010:2833-2836.
 72. Feng X, Salerno M, Kramer CM, Meyer CH. Kalman filter techniques for accelerated Cartesian dynamic cardiac imaging. *Magn Reson Med* 2012.

73. Yang JF, Zhang Y. Alternating Direction Algorithms for $L(1)$ -Problems in Compressive Sensing. *Siam J Sci Comput* 2011;33(1):250-278.
74. Lustig M, Pauly JM. SPIRiT: Iterative self-consistent parallel imaging reconstruction from arbitrary k-space. *Magnetic resonance in medicine : official journal of the Society of Magnetic Resonance in Medicine / Society of Magnetic Resonance in Medicine* 2010;64(2):457-471.
75. Liang D, Liu B, Wang JJ, Ying L. Accelerating SENSE Using Compressed Sensing. *Magnetic Resonance in Medicine* 2009;62(6):1574-1584.
76. Kim D, Dyvorne HA, Otazo R, Feng L, Sodickson DK, Lee VS. Accelerated Phase-Contrast Cine MRI Using k-t SPARSE-SENSE. *Magnetic Resonance in Medicine* 2012;67(4):1054-1064.
77. Murphy M, Alley M, Demmel J, Keutzer K, Vasanawala S, Lustig M. Fast $l(1)$ -SPIRiT Compressed Sensing Parallel Imaging MRI: Scalable Parallel Implementation and Clinically Feasible Runtime. *Ieee T Med Imaging* 2012;31(6):1250-1262.
78. Chen X, Salerno M, Yang Y, Epstein FH. Motion-compensated compressed sensing for dynamic contrast-enhanced MRI using regional spatiotemporal sparsity and region tracking: Block low-rank sparsity with motion-guidance (BLOSM). *Magn Reson Med* 2014;72(4):1028-1038.
79. Tsao J, Boesiger P, Pruessmann KP. k-t BLAST and k-t SENSE: Dynamic MRI with high frame rate exploiting spatiotemporal correlations. *Magnetic Resonance in Medicine* 2003;50(5):1031-1042.
80. Motwani M, Jogiya R, Kozerke S, Greenwood JP, Plein S. Advanced cardiovascular magnetic resonance myocardial perfusion imaging: high-spatial resolution versus 3-

- dimensional whole-heart coverage. *Circulation Cardiovascular imaging* 2013;6(2):339-348.
81. Plein S, Kozerke S, Suerder D, Luescher TF, Greenwood JP, Boesiger P, Schwitter J. High spatial resolution myocardial perfusion cardiac magnetic resonance for the detection of coronary artery disease. *Eur Heart J* 2008;29(17):2148-2155.
 82. Walsh DO, Gmitro AF, Marcellin MW. Adaptive reconstruction of phased array MR imagery. *Magnetic Resonance in Medicine* 2000;43(5):682-690.
 83. Lustig M, Pauly JM. SPIRiT: Iterative Self-consistent Parallel Imaging Reconstruction From Arbitrary k-Space. *Magnetic Resonance in Medicine* 2010;64(2):457-471.
 84. Chen X, Salerno M, Epstein FH. Accelerated first-pass perfusion CMR using compressed sensing with regional spatiotemporal sparsity. *Journal of cardiovascular magnetic resonance : official journal of the Society for Cardiovascular Magnetic Resonance* 2013;15(Suppl 1):E16.
 85. Zhang T, Cheng JY, Potnick AG, Barth RA, Alley MT, Uecker M, Lustig M, Pauly JM, Vasanawala SS. Fast pediatric 3D free-breathing abdominal dynamic contrast enhanced MRI with high spatiotemporal resolution. *J Magn Reson Imaging* 2013.
 86. Yoon H, Ye JC. Region Adaptive Motion Compensated Dynamic CS for Cardiac Perfusion Imaging. *Proceedings of ISMRM 2014*:4382.
 87. Mohsin YQ, Yang Z, Lingala SG, Jacob M. Motion Compensated Dynamic Imaging Without Explicit Motion Estimation. *Proceedings of ISMRM 2014*:0747.
 88. Chen X, Yang Y, Salerno M, Epstein FH. Accelerated Cine DENSE using Variable Density Spirals and Compressed Sensing with Parallel Imaging. *Proceedings of ISMRM 2014*:3892.

89. Chen X, Yang Y, Salerno M, Meyer CH, Epstein FH. Accelerated cine DENSE MRI using compressed sensing and parallel imaging. *Journal of cardiovascular magnetic resonance : official journal of the Society for Cardiovascular Magnetic Resonance* 2014;16(Suppl 1):W16.
90. Zhong X, Helm PA, Epstein FH. Balanced Multipoint Displacement Encoding for DENSE MRI. *Magnetic Resonance in Medicine* 2009;61(4):981-988.
91. Zhong X, Spottiswoode BS, Cowart EA, Gilson WD, Epstein FH. Selective suppression of artifact-generating echoes in cine DENSE using through-plane dephasing. *Magn Reson Med* 2006;56(5):1126-1131.
92. Spielman DM, Pauly JM, Meyer CH. Magnetic resonance fluoroscopy using spirals with variable sampling densities. *Magnetic resonance in medicine : official journal of the Society of Magnetic Resonance in Medicine / Society of Magnetic Resonance in Medicine* 1995;34(3):388-394.
93. Lee JH, Hargreaves BA, Hu BS, Nishimura DG. Fast 3D imaging using variable-density spiral trajectories with applications to limb perfusion. *Magnetic resonance in medicine : official journal of the Society of Magnetic Resonance in Medicine / Society of Magnetic Resonance in Medicine* 2003;50(6):1276-1285.
94. Fessler JA, Sutton BP. Nonuniform fast Fourier transforms using min-max interpolation. *Ieee T Signal Proces* 2003;51(2):560-574.
95. Feng L, Donnino R, Babb J, Axel L, Kim D. Numerical and in vivo validation of fast cine displacement-encoded with stimulated echoes (DENSE) MRI for quantification of regional cardiac function. *Magn Reson Med* 2009;62(3):682-690.

96. Spottiswoode BS, Zhong X, Hess AT, Kramer CM, Meintjes EM, Mayosi BM, Epstein FH. Tracking myocardial motion from cine DENSE images using spatiotemporal phase unwrapping and temporal fitting. *IEEE Trans Med Imaging* 2007;26(1):15-30.
97. Cerqueira MD, Weissman NJ, Dilsizian V, Jacobs AK, Kaul S, Laskey WK, Pennell DJ, Rumberger JA, Ryan T, Verani MS, American Heart Association Writing Group on Myocardial S, Registration for Cardiac I. Standardized myocardial segmentation and nomenclature for tomographic imaging of the heart. A statement for healthcare professionals from the Cardiac Imaging Committee of the Council on Clinical Cardiology of the American Heart Association. *Circulation* 2002;105(4):539-542.